Investigation of the detergent activity in a fully formulated lubricant for DLC-involving contact : Control of friction by load-induced detergent structure modification

Yue Guan

Investigation of the detergent activity in a fully formulated lubricant for DLC-involving contact: Control of friction by load-induced detergent structure modification

Etude de l'activité détergente dans un lubrifiant formulé pour un contact impliquant du DLC : Contrôle du frottement par la modification de la structure du détergent induite par la charge

Date de soutenance prévue : le 11 Décembre, 2023

Par Yue GUAN

Devant le jury composé de :

Pr. Christophe DONNET	Université Jean Monnet	Président du jury
Pr. Mitjan KALIN	University of Ljubljana	Rapporteur
Pr. Adrian MORINA	University of Leeds	Rapporteur
Dr. Maria-Isabel DE BARROS BOUCHET	Ecole Centrale de Lyon	Directrice de thèse
Pr. Fabrice DASSENOY	Ecole Centrale de Lyon	Co-directeur de thèse

Abstract

For over a decade now, Diamond-Like Carbon (DLC) coatings have been applied to sliding components within internal combustion engines, such as cam lobes, tappets, finger followers, and piston rings. The purpose of using DLC coating is to decrease energy losses attributed to friction. These coatings are lubricated using traditional engine oils initially designed for steel components. However, few studies have been carried out to understand the tribological properties of DLC involved tribo-pair with a fully formulated oil.

In this work, tribological tests were performed by using a commercially available fully formulated lubricant for a-C:H DLC involved tribo-pair. Steel/steel contact was used as the reference. A focus was made on the influence of the contact pressure on the tribological performance of the tribo-systems.

A ring-on-disk configuration was first used to simulate the piston-ring-cylinder liner of internal combustion engine in the more severe tribological conditions. It was found that the friction coefficient decreases as the function of pressure in boundary/mixed lubrication regime for steel/a-C:H mixed contact. The surface analyses showed that the tribofilm was rich in calcium carbonate. Its structure was found to be load-dependent. Vaterite was found at low load, aragonite at medium load and calcite at high load. This crystal transformation was not observed for the steel/steel tribo-pair, for which the friction increased as the function of pressure.

In order to have a better understanding on the effect of contact pressure on the observed tribological behaviors, additional friction tests were carried out using a standard ball-on-disk configuration and with the same tribo-pairs. A friction reduction at high pressure was obtained in a-C:H self-mated contact when the fully formulated oil was used. Similarly, the tribofilm is rich in calcium carbonate.

Moreover, the amorphous calcium carbonate crystallizes to calcite at high pressure. Friction tests were also conducted with the corresponding base oil blending with 1wt% of the detergent additive. The friction reduction at high contact load was observed for each tribo-pair. The tribofilm was found again to be rich in calcium carbonate. The amorphous calcium carbonate crystallizes to calcite at high contact pressure. These findings are in line with the ring-on-disk configuration.

Keywords: Diamond-Like Carbon (DLC) coatings, fully formulated oil, contact pressure effect, overbased detergent additive, calcium carbonate crystal allotropes

Résumé

Depuis plus d'une décennie, les revêtements en carbone de type diamant (DLC) sont appliqués sur des composants coulissants à l'intérieur des moteurs à combustion interne, tels que les cames, les poussoirs, les galets et les segments de piston. L'objectif de l'utilisation de tels revêtements est de réduire les pertes d'énergie dues au frottement dans les moteurs. Ces revêtements sont lubrifiés à l'aide d'huiles moteur traditionnelles initialement conçues pour les composants en acier. Cependant, peu d'études ont été réalisées pour comprendre les propriétés tribologiques de contacts impliquant des revêtements en DLC en présence d'huiles entièrement formulées.

Dans ce travail, des essais tribologiques ont été réalisés en utilisant un lubrifiant commercial entièrement formulé et avec un contact impliquant un DLC de type a-C:H. Le contact acier/acier a été utilisé comme référence. L'accent a été mis sur l'influence de la pression de contact sur les performances tribologiques du système étudié.

Une configuration bague-sur-disque a d'abord été utilisée pour simuler le piston-segment-cylindre d'un moteur à combustion interne dans des conditions tribologiques sévères. Il a été constaté que le coefficient de frottement diminuait en fonction de la pression dans le régime de lubrification limite/mixte pour le contact mixte acier/a-C:H. Les analyses de surface ont montré que le tribofilm était riche en carbonate de calcium. Sa structure s'est avérée dépendre de la charge. La vaterite a été trouvée à faible charge, l'aragonite à charge moyenne et la calcite à charge élevée. Cette transformation cristalline n'a pas été observée pour le contact acier/acier, pour lequel le frottement augmente en fonction de la pression.

Afin de mieux comprendre l'effet de la pression de contact sur les différents comportements tribologiques observés, des essais de frottement supplémentaires ont été réalisés en utilisant une

configuration bille-sur-disque standard ainsi que les mêmes types de contact. Une réduction du frottement a été observée sous forte charge pour le contact a-C:H/a-C:H en présence de l'huile entièrement formulée. Le tribofilm obtenue s'est montré être riche en carbonate de calcium présent sous forme de calcite. Des essais de frottement supplémentaires ont également été effectués avec l'huile de base additivée de 1% en poids d'additif détergent. Une réduction de frottement a été observée à haute pression pour tous les contacts étudiés. Le tribofilm s'est révélé une fois de plus être riche en carbonate de calcium, présent sous forme calcite à haute pression. Ces résultats sont cohérents avec les résultats obtenus en configuration bague-sur-disque.

Mots-clés : Revêtements Diamond-Like Carbon (DLC), huile formulée, effet de la pression de contact, additif surbasé détergent, allotropes du carbonate de calcium.

Acknowledgements

First of all, I would like to give my heartfelt thanks to all the people who have ever helped me in this paper.

My sincere and hearty thanks and appreciations go firstly to my supervisors, Mme. Maria-Isabel De Barros Bouchet and Prof. Fabrice Dassenoy, whose suggestions and encouragement have given me much insight into the researches. It has been a great privilege and joy to study under your guidance and supervision. Furthermore, it is my honor to benefit from your personality and diligence, which I will treasure my whole life. My gratitude to you knows no bounds.

I am also extremely grateful to all my friends and colleagues who have kindly provided me assistance and companionship in the course of preparing this paper.

In addition, many thanks go to my family for their unfailing love and unwavering support.

Finally, I am really grateful to all those who devote much time to reading this thesis and give me much advice, which will benefit me in my future study.

Contents

General introduction

Global energy usage has risen dramatically since the industrial revolution and currently sits at approximately 400 EJ (exajoule, 1 EJ = 10^{18} joules) per year. Despite technological advances in mechanical engineering, fossil fuels still remain a significant source of energy. Unfortunately, the intensive use of this fossil fuel has negative impacts on the environment. 30% of the world oil consumption is due to the transportation vehicles, with about one third lost due to friction and wear in their moving parts [1]. Holmberg et al. has recently created a systematic method to determine the worldwide consequences of friction and wear on the energy demand and the environment in various industrial sectors [2-4]. According to the report, despite the considerable improvements in managing friction and wear, there is still a notable amount of energy being wasted to counteract friction, particularly within the transportation industry.

In the majority of transportation vehicles, the internal combustion engine (ICE) serves as the primary source of power. As illustrated in Figure 1, in a typical passenger car, only 21% of the fuel is used for the vehicle's movement, with the remaining 79% being lost as energy waste, among which about 12% is due to the friction loss in car engine [5]. On the other hand, the rise in the production of electric vehicles can be seen as a significant measure to reduce the negative environmental effects of traditional engines. However, the production of vehicles based on ICE is still continuing and will not be completely replaced by electric cars even after 2035 (agreement on the development of the fuels that are carbon neutral).

From the perspective of energy consumption, the piston assembly, comprising of pistons, rings, and cylinder liners, is particularly significant in ICE for passenger cars, because almost half of the energy is dissipated due to the friction caused by these mechanical parts [6]. Figure 2(a) displays

how energy losses are distributed in internal combustion engines, with a particular emphasis on the significance of mechanical friction. The focus then narrows down to the weight of the piston-ring-cylinder-liner (PRCL) friction in energy losses (Fig. 2(b) and Fig. 2(c)) [7-10]. The illustration indicates that PRCL friction accounts for a reduction of 0.8% to 8% in engine efficiency. Above all, minimizing PRCL friction and wear is a straightforward approach to improve the efficiency of transferring fuel from the tank to the wheels and to prolong the service life of materials.

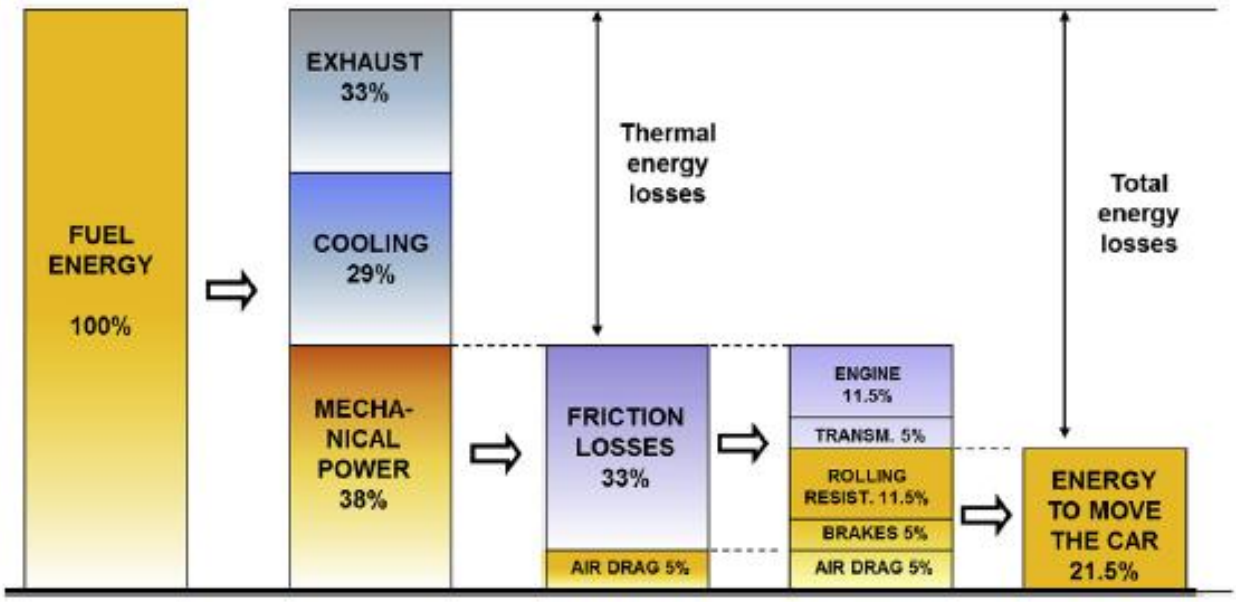

Fig. 1 Details on passenger car energy consumption [5].

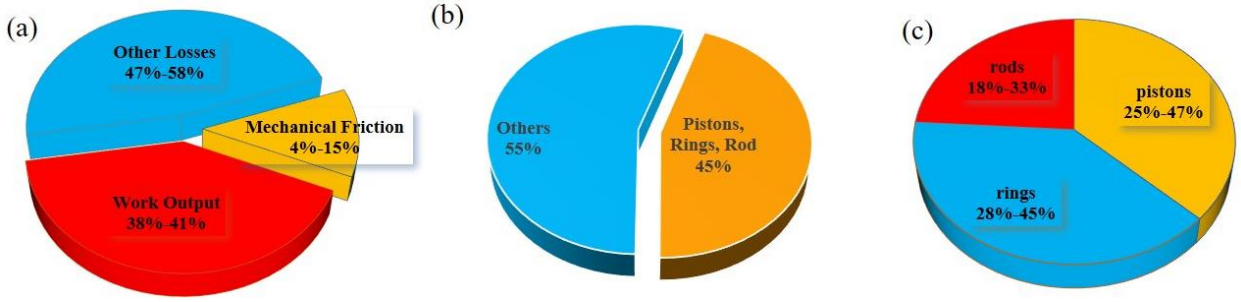

Fig. 2 Energy distribution in internal combustion engine (a) total energy (b) mechanical friction (c) friction in pistons, rings and rod

Great efforts have been made to realize these goals, among which the application of diamond-like carbon (DLC) coatings for sliding components as piston rings, cylinder liners, cams and tappets. The so-called superlubricity (friction coefficient below 0.01) was also achieved by employing DLC with specific additives [11-13]. Therefore, the huge potential of DLC in energy loss reduction could drive the attractive investigation of its application in ICE.

Many studies have been performed on tribological performances between DLC and additives in engine oils, in order to reveal their interaction mechanism under different sliding conditions. However, most of the studies used the model oil, which was obtained by mixing base oil with one or two "traditional" additives, including zinc dialkyldithiophosphates (ZDDP), molybdenum dithiocarbamate (MoDTC) and fatty acids. One of the problems of employing model oil is that the roles of other additives present in engine oils, such as detergents and many others, are ignored. The effects induced by these "ignored" additives could lead to some completely different tribological behaviors. Moreover, due to the various sliding conditions (sliding speed, temperature, contact pressure, etc.) and friction tests mode (reciprocating, rolling-sliding, etc.) selected in publications, the tribological results can be contradictory. Therefore, the interaction mechanisms between DLC and fully formulated engine oils are still unclear.

The main focus of this research work is to investigate the pressure effect of a commercially available fully formulated oil on DLC coated ring, ball and disk in boundary and mixed lubrication regimes. Ring-on-disk friction tests were proposed and performed by our industrial collaborator (HEF-IREIS Groupe) with the purpose to simulate the friction conditions found in PRCL, where one of the most energy loss and failure occurs in mono-block of ICE. The effects of the contact pressure on the coefficient of friction (CoF) and wear were investigated. In the same time,

additional ball-on-disk friction tests were carried out at the lab scale in LTDS in order to simplify the tribo-system and to lead a fundamental understanding on the tribo-chemical reactions between the lubricants and the rubbing materials as the contact pressure was tuned. Tests were conducted with the same lubricants and materials than those used in HEF group.

This PhD thesis consists of general introduction and 6 chapters.

Chapter 1 presents the structure of PRCL in ICE, the basic properties and different types of DLC used for tribological applications. The previous studies on the interaction between fully formulated engine oils and DLC coatings are reported. The main concern of this research work is presented.

Chapter 2 describes information on the materials properties, the parameters and mechanism of the employed tribometers and characterization techniques for surface analyses carried out after friction tests.

Chapter 3 reports the effect of the contact pressure on tribological performances for steel/DLC mixed contact (ring-on-disk configuration) with fully formulated lubricant. Steel self-mated contact and DLC self-mated contact are also employed to compare with steel/DLC mixed contact. The surface analyses results indicate that the tribological behaviors are significantly related to the structure of calcium carbonate, derived from detergent additive, in tribofilm.

In chapter 4, the tribo-system is simplified into ball-on-disk lab scale to study the impacts of the contact pressure with the same lubricant. The steel self-mated, DLC self-mated and steel/DLC mixed contacts are selected to compare with the tribo-pairs in chapter 3. The significant impacts of calcium carbonate structure in tribofilm for tribological performances are confirmed by surface analyses.

In chapter 5, the tribological performances of the model oil (the base oil blending with the detergent additive utilized in the fully formulated lubricant) are investigated. The sliding conditions and tribo-pairs are the same that those used in the chapter 4. The role of the calcium carbonate structure in the tribological behavior of the lubricant is confirmed by in depth surface analyses, and confirm the results obtained in chapter 3 and 4.

Chapter 6 summarizes all the results of this PhD work and propose the future works.

References

[1] Holmberg, K., & Erdemir, A. (2017). Influence of tribology on global energy consumption, costs and emissions. Friction, 5(3), 263–284. https://doi.org/10.1007/s40544-017-0183-5.

[2] Holmberg, K., Andersson, P., Nylund, N.-O., Mäkelä, K., Erdemir, A. (2014). Global energy consumption due to friction in trucks and buses. Tribology International, 78, 94–114. https://doi.org/10.1016/j.triboint.2014.05.004

[3] Holmberg, K., Kivikytö-Reponen, P., Härkisaari, P., Valtonen, K., Erdemir, A. (2017). Global energy consumption due to friction and wear in the mining industry. Tribology International, 115, 116–139. https://doi.org/10.1016/j.triboint.2017.05.010

[4] Holmberg, K., Siilasto, R., Laitinen, T., Andersson, P., Jäsberg, A. (2013). Global energy consumption due to friction in paper machines. Tribology International, 62, 58–77. https://doi.org/10.1016/j.triboint.2013.02.003

[5] Holmberg, K., Andersson, P., & Erdemir, A. (2012). Global energy consumption due to friction in passenger cars. Tribology International, 47, 221-234. https://doi.org/10.1016/j.triboint.2011.11.022

[6] Richardson, D. E. (2000). Review of power cylinder friction for diesel engines. Journal of Engineering for Gas Turbines and Power, 122(4), 506–519. https://doi.org/10.1115/1.1290592

[7] Patton, K. J., Nitschke, R. C., Heywood, J. B. (1989). Development and evaluation of a friction model for spark-ignition engines. SAE Technical Paper Series. https://doi.org/10.4271/890836

[8] Ting, L. L. (1985). A review of present information on Piston Ring Tribology. SAE Technical Paper Series. https://doi.org/10.4271/852355

[9] Kovach, J. T., Tsakiris, E. A., Wong, L. T. (1982). Engine friction reduction for improved fuel economy. SAE Technical Paper Series. https://doi.org/10.4271/820085

[10] Koch, F., Geiger, U., Hermsen, F.-G. (1996). PIFFO - piston friction force measurements during engine operation. SAE Technical Paper Series. https://doi.org/10.4271/960306

[11] Kano, M., Martin, J. M., Yoshida, K., & De Barros Bouchet, M. I. (2014). Super-low friction of ta-C coating in presence of oleic acid. Friction, 2(2), 156-163. https://doi.org/10.1007/s40544-014-0047-1

[12] Cen, H., Morina, A., Neville, A., Pasaribu, R., & Nedelcu, I. (2012). Effect of water on ZDDP anti-wear performance and related tribochemistry in lubricated steel/steel pure sliding contacts. Tribology International, 56, 47-57. https://doi.org/10.1016/j.triboint.2012.06.011

[13] De Barros Bouchet, M. I., Martin, J. M., Avila, J., Kano, M., Yoshida, K., Tsuruda, T., Bai, S., Higuchi, Y., Ozawa, N., Kubo, M., & Asensio, M. C. (2017). Diamond-like carbon coating under oleic acid lubrication: Evidence for graphene oxide formation in superlow friction. Scientific Reports, 7(1). https://doi.org/10.1038/srep46394

Chapter 1 Bibliography

This chapter introduces piston-ring-cylinder-liner (PRCL) assemblies and diamond-like carbon (DLC) coatings, exploring key aspects related to tribology. It concludes with a concise discussion of the impact of contact pressure on DLCs lubricated with fully formulated engine oil.

1.1 Introduction

This work mainly focuses on the tribological performances of a commercialized lubricant used for internal combustion engines (ICE), The piston-ring-cylinder-liner (PRCL) part is mainly concerned by this study. Therefore, first of all, the basic concept of PRCL is given. After that, diamond-like carbon (DLC) coatings, as one of the materials that have been used in PRCL to reduce friction and wear, are introduced. Then, the most relevant previous studies on the interaction between DLC and fully formulated lubricant are presented.

1.2 Piston-ring-cylinder-liner (PRCL)

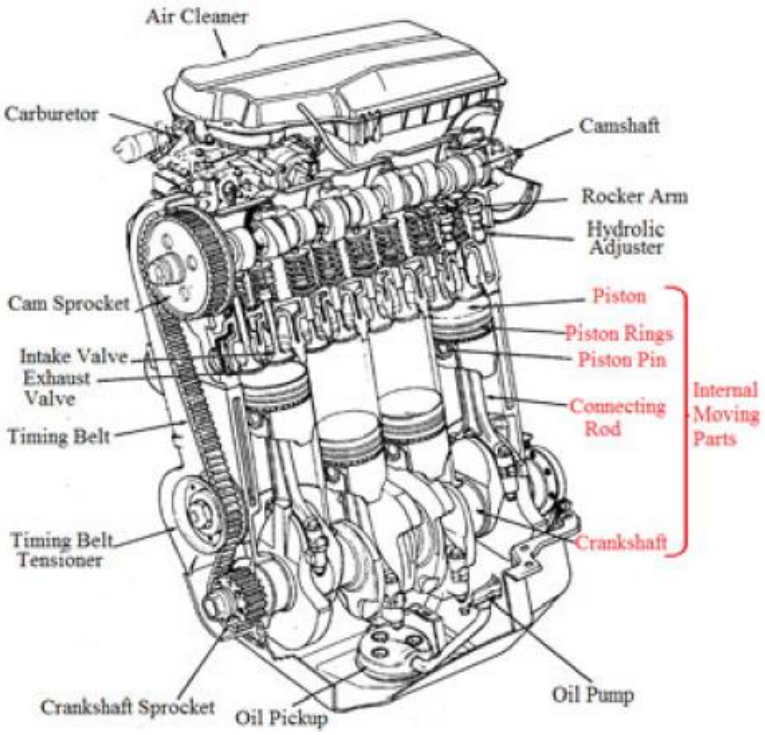

Fig. 1.1 the moving parts of internal combustion engine

Fig. 1.1 [1] presents the moving parts that require a large amount of lubricant in car engine. In this work, the research concentrates on the piston rings, where the lubricant supply is not abundant. The lack of lubricant makes the rings operate in very severe conditions (including boundary and

mixed lubrication regimes), particularly the uppermost one which is located the furthest away from the source of lubricant. From this point of view, the failure of engine is easily induced by the breakdown of rings.

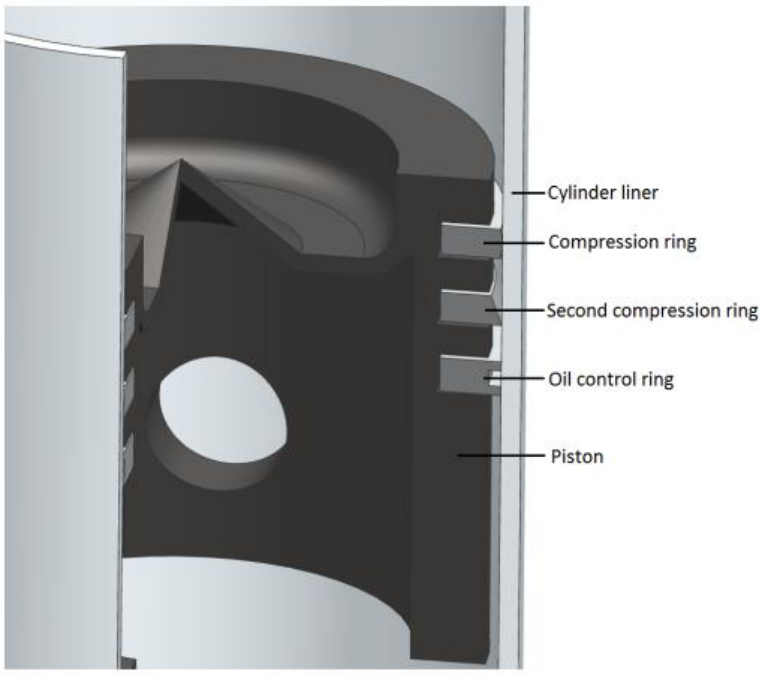

Fig. 1.2 Schematic view of components in PRCL [2]

The close-up of PRCL is shown in Fig. 1.2 [2]. The elastic rings known as piston rings fit between the cylinder wall and the piston grooves. Within the engine's PRCL pack, there are generally three rings. The first is the compression ring, located at the top and nearest to the combustion chamber. It is exposed to the highest pressure and temperature. Therefore, this ring bears the highest risk of potential failure. Its shape is parabolic, and its primary objective is to seal the combustion chamber during combustion to prevent any leakage. Its tension force can range between 5 and 20 N. The second is the wiper ring, namely second compression ring, which is found between the compression and oil control rings. It serves the purpose of sealing and controlling oil, with a tension that ranges between 5N and 30 N. Lastly, the oil control ring is located closest to the

crankcase, and it has two running faces. Its primary function is to regulate the oil's flow by wiping and guiding it through its holes to the oil reservoir, with a tension that ranges between 10N and 50 N. The cylinder liner serves as the inner wall of an engine cylinder and it is where the piston and piston rings operate. Due to its exposure to high pressure and temperature, the material used for the liner surface must be able to withstand such conditions [3].

Therefore, it is necessary to develop the lubrication strategy and coatings to minimize the materials loss due to friction and wear, and to avoid the failure of PRCL. Over the past 20 years, the chromium coatings have met the standards for engine performance. However, in recent years, the operating pressures of engines have significantly increased in both commercial vehicles and motorsport. Carbon-based materials have emerged as a highly advantageous surface engineering solution in the automotive industry. Diamond-like carbon (DLC), which is a more affordable alternative to diamond, has proven to be highly effective in tribological environments by achieving superlubricity conditions and reducing the coefficient of friction [4-7]. Compared to conventional solutions like CrN coatings, DLC coatings offer superior performance [8], for example, the higher hardness. Generally, a harder surface material will have greater mechanical and wear resistance [9-10]. At the same time, DLC coatings also have low friction and low wear characteristics, making them suitable for powertrain parts to improve their tribological performance [11]. DLC coatings have been widely used in engine components, including PRCL section, see Fig. 1.3 [12]. It has been justified that DLC-coated piston ring can avoid scuffing and provide low coefficient of friction (CoF) values [13]. Meanwhile, the friction reduction is also obtained when DLC coatings are applied on cylinder liners [14]. When DLC coatings are combined with lubricants, better tribological performances are exhibited, thus providing a positive effect on engine life [15,16].

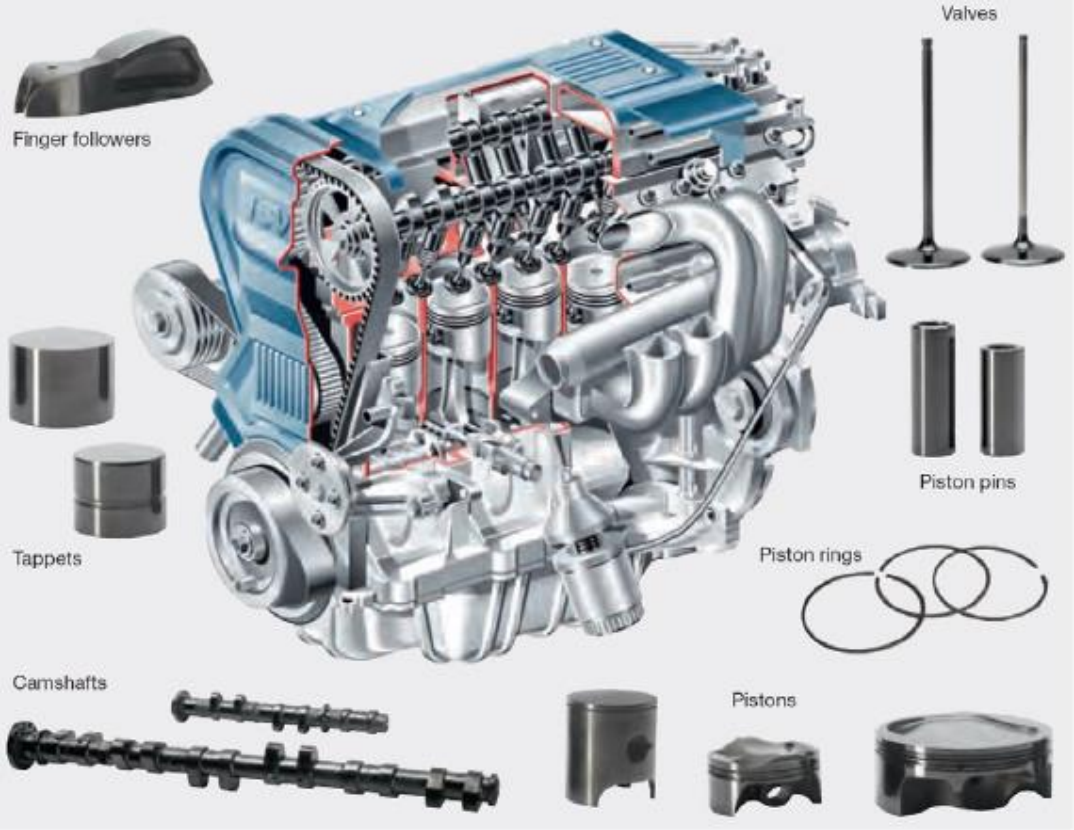

Fig. 1.3 DLC coated parts in internal combustion engine

In the following section, detailed information of DLC coatings and their applications in tribology are introduced. Then, the studies of interaction mechanisms between DLC and fully formulated lubricants will be presented.

1.3 Diamond-like carbon (DLC)

DLC coatings are a type of thin film made of amorphous carbon that have a combination of sp^2 and sp3 coordinated bonds. They can include additional elements such as hydrogen or metal/non-metal doping depending on how they are produced (using various chemical vapor deposition and physical vapor deposition methods) and on the requirements of the application. A significant advantage of DLC coatings is that their properties can be customized by modifying the deposition process, which makes them versatile for many different engineering applications, not only in

transportation (PRCL, as mentioned above), but also for manufacturing, microelectronics, optics, space, transportation, and biomedical technology.

1.3.1 History of DLC

In 1953, Schmellenmeier [17] developed thin films of tungsten carbide (WC) by using acetylene gas in a glow discharge process at low temperatures. Later, it was observed that black hard formless layers were formed at the cathode pole with low flow rate of current, but thick hard films were identified as diamonds by X-ray diffraction [18]. In 1951, Konig and Helwig [19] investigated the glow-discharge process in a benzene atmosphere, but the films grown on the anode were yellow and with a low-density. Heisen [20] found that films deposited on the cathode had higher density than those on the anode, and the growth rate was depending on the substrate geometries. The concept of DLC was originally introduced by Aisenberg and Chabot in 1971 [21]. They formed layers using an ion beam deposition technique that involved C, argon particles, and a graphite electrode at ambient temperature. Upon examination, it was discovered that the films were optically transparent, resistant to wear, and had good electrical and chemical flow. The film structure was described as partially crystalline with lattice parameters similar to those of diamond. Aisenberg and his colleagues [22] reported in 1971 that DLC coatings improved the cutting performance of paper-cutting blades, resulting in a decrease in the frictional coefficient. Spencer and others [23] investigated the performance of DLC coatings, similar to Aisenberg and Chabot. Whitmell and Williamson [24] used the ion beam deposition method of Schmellenmeier and Heisen to organize hard and protective coatings of up to 4 μm thickness on various metal surfaces. However, they used a gas combination of C_2H_4 and 5% Ar. The protective layer needed to maintain a positive charge to achieve maximum thickness, and Holland [25] explained that secondary electrons generated at the boundary of the domed aperture compensate for the positive charge. In

a later study, the findings were validated for a DC-based particle plating technique used to create a measure of amorphous hydrogenated carbon (a-C: H) on protective glass substrates [26].

1.3.2 Classification of DLC

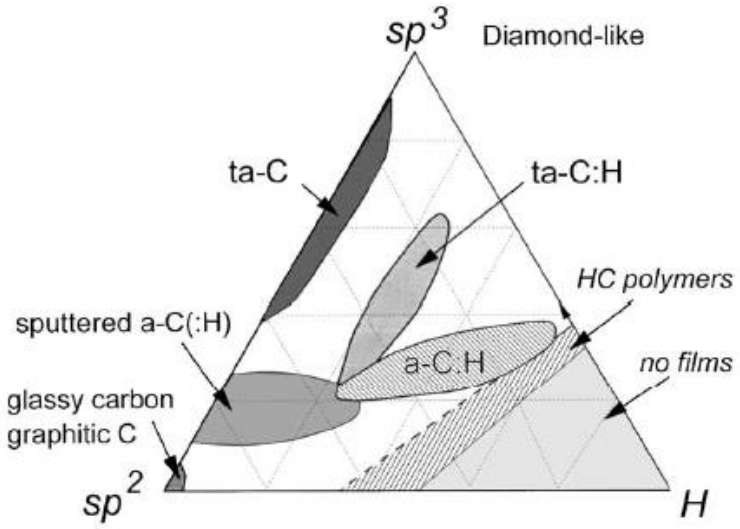

Fig. 1.4 Ternary phase diagram for hydrocarbon films

In order to depict the different compositions of DLC, a ternary phase diagram shown in the Fig. 1.4 is used, which was first demonstrated by Jacob and Moller [27]. There are various types of amorphous carbons (a-Cs), including those with disordered graphitic ordering such as glassy carbon, and a-C which are located in the lower left-hand corner of the triangle. On the other hand, the upper right-hand corner of the triangle is defined by two hydrocarbon polymers: polyethylene $(CH2)_n$ polyacetylene $(CH)_n$, which represent the limits beyond which interconnecting C-C networks cannot form, and only molecules can form instead. When the fraction of sp^3 bonding reaches a high degree, the resulting a-C is referred to as tetrahedral amorphous carbon (ta-C), as proposed by McKenzie [28], to distinguish it from sp^2 a-C. Various deposition methods such as plasma-enhanced chemical vapor deposition (PECVD) are capable of reaching into the interior of the triangle, producing a-C:H. Its content of sp^3 bonding is not significant, and the material has a

high hydrogen content. Therefore, Weiler et al. [29] have coined the term hydrogenated tetrahedral amorphous carbon (ta-C:H) to describe a material with less hydrogen content and more sp3 bonding, which can be produced using high plasma density PECVD reactors.

Except for the DLC classified by sp^2/sp^3 ratio and hydrogen contents, which are indicated in Fig. 1.4, DLC can also be classified as doped and non-doped types, see Fig. 1.5. The categorization of doped DLC coatings can be further differentiated into two types: those metal-doped (such as Ti, W, Cr) and those nonmetal-doped (such as S, Si, F, N). DLC coatings are acknowledged to be chemically inactive [30,31], and the addition of dopants to these coatings can heighten their surface energy and capacity to interact with lubricants, creating surface protective films. The use of doped DLCs also offers other benefits, such as good bonding to the underlying material, increased resistance to wear, improved electrical conductivity. The internal compressive stresses during deposition can also be reduced [32-35].

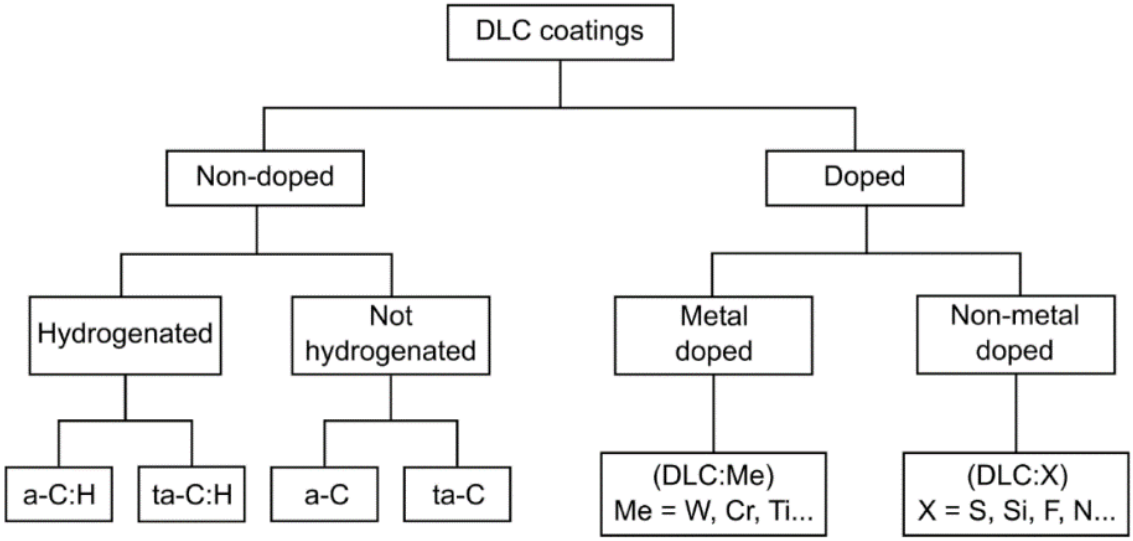

Fig. 1.5 Non-doped and doped DLC classification

1.3.3 Deposition method

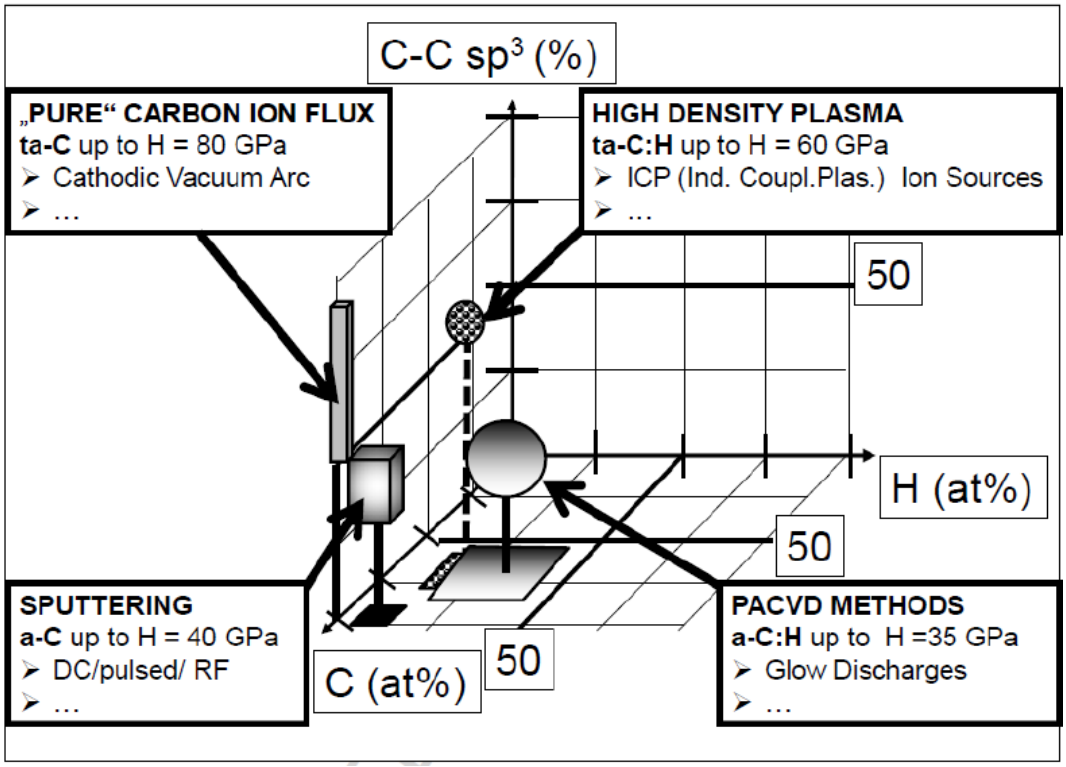

Fig. 1.6 Several commonly used deposition techniques for each type of DLC and their corresponding sp^3/sp^2 and hardness

As already introduced, the first DLCs were prepared by Aisenberg and Chabot using ion beam deposition. However, DLCs can be produced in various methods. The methods can be divided based on the demand of laboratory experiments or industrial manufacturing. Some commonly-used techniques for DLCs are shown in Fig. 1.6 [36]. The DLC film is formed by condensing a beam of carbon or hydrocarbon ions with medium energy (~100 eV), and the sp^3 bonding is created through a physical process resulting from the impact of these ions on the growing film. This is different from the chemical vapor deposition (CVD) used in diamond to stabilize sp^3 bonding [37]. The ideal DLC deposition process should involve a carbon ion flux of approximately 100 eV per carbon atom, with a narrow energy distribution, a single energetic species, and the least

possible number of non-energetic (typically neutral) species [29]. Typically, a decrease in energy results in a reduction of sp^3 carbon content. Neutral species that are rich in sp^2 carbon can create growth defects, such as conical droplets, that increase surface roughness. Additionally, to prevent delamination and failure, it is crucial to establish a robust interfacial bond between the DLC coating and the substrate material. To accomplish this, an intermediate-adhesion layer is often used, with metals such as Cr, W, Si, and Ti being commonly employed due to their carbide- or silicide-forming properties. Concerning the fact that the focus of this work is not on the DLC deposition, no more technological details will be introduced.

1.4 Tribological performances of DLC

1.4.1 Introduction

The tribological behaviors of doped/non-doped DLC coatings under lubricated and dry conditions have been investigated for many years. The employed lubricants were obtained by blending single or multiple additives with base oil or by using directly the fully formulated engine oil. In this work, we only concentrated on the tribological performances of non-doped DLC with fully formulated lubricants. A fully formulated lubricant is obtained by mixing conventional additives with base oil. These additives can be extreme pressure/anti-wear, organic/molybdenum friction modifier, dispersant, detergent, corrosion inhibitors, viscosity improvers, etc. The following sections present the latest studies of the interaction between DLC and fully formulated lubricants and the variation of tribological behaviors as the function of contact pressure.

1.4.2 DLC with fully formulated lubricants

Researches on the interactions between DLC coatings and commercially available formulated lubricants or engine oils are significant to provide the proper instruction on lubricants selection for

specific usages. Unfortunately, the majority of the investigations on DLC tribological performances tend to be done with a base oil plus one or two additives, including molybdenum dithiocarbamate (MoDTC), zinc dialkyldithiophosphates (ZDDP), which are the two most popular friction modifier and anti-wear additives. However, these studies ignored the fact that the additives may perform very differently as they are mixed with other additives.

Only a few studies discussed the DLC performances with fully formulated lubricants. For example, Tung and Gao [38] performed PRCL test on a modified high frequency reciprocating machine by employing engine oil with and without MoDTC. The DLC and chromium nitride (CrN) coating (type unknown) were deposited on nitride stainless steel ring. The results showed that DLC coated ring reduced wear on counter nitride stainless steel cylinder liner comparing to CrN. The lubricant contained with MoDTC and both friction and wear were reduced. Unfortunately, no deeper surface analyses were conducted to understand the phenomena.

Neville and her group [39] selected hydrogenated DLC to perform ball-on-disk friction tests in boundary lubrication regime with two types of fully formulated lubricants, one was based on ZDDP and Ca detergent, the second one was mainly sulfur-based extreme pressure additive and antioxidant. The friction behaviors of hydrogenated DLC were also compared with boron carbide, tungsten carbide and pure steel samples. For both of the two oils, it was found that the lowest friction was always obtained with the hydrogenated DLC/steel. However, only sliding traces of tribofilm elements were observed by SEM and XPS on hydrogenated DLC wear tracks. Comparing with other coatings and steel, the quantification of these elements was relatively lower, especially for the oil containing sulfur-based extreme pressure additive. A lower tribo-chemical reaction on

hydrogenated DLC was suggested. The detailed interpretation on how getting this low friction was not given.

In another study of Neville [40], a-C:H (15% H) and M2 steel mixed tribo-pair was used in fully formulated lubricant with/without friction modifier. No visible wear was observed on the DLC with the fully formulated lubricant containing the friction modifier. By contrast, the lubricant without friction modifier could induce a polishing mechanism wear on DLC. No friction reduction was observed due to the formation of polyphosphate based tribofilm on surface. Although the impacts of other additives in lubricant, such as calcium-based detergent and nitrogen-based dispersants, were referred, there was not further related investigations.

Few other studies on friction and wear of DLC in fully formulated lubricants were found. The main conclusions are always related with the variation of polyphosphate structure derived from anti-wear additives (ZDDP, etc.) and the wear results induced by MoDTC when the DLC coating is present. The roles of other additives, such as detergent, are ignored.

Detergents are commonly added to the lubricant for the formulation of lubricants for automobiles and boats. These detergent additives serve several essential purposes, such as neutralizing acidic combustion by-products to minimize corrosive wear, neutralizing acidic lubricant oxidation products, and acting as a "detergent" to prevent the buildup of deposits on high-temperature surfaces like pistons. The structure of the detergent additives consists of two primary components: a metal surfactant salt and an inorganic base stabilized by this surfactant. Some lubricant detergents only contain the surfactant, and these are referred to as "neutral" detergents. Detergents that contain an inorganic base reserve are called "overbased" because they contain more moles of base than moles of acid to play the role of neutralization. There have been various surfactant types utilized

to create lubricant detergents. Examples of these include sulphonates, alkylphenates, sulfurized alkyl phenates, carboxylates, and salicylates, etc.

Except for the ignorance of additives as detergent in fully formulated oil, the effects of sliding conditions (contact pressure, sliding speed, etc.) were not taken into account. From these points of view, the previous studies on the interaction between DLC and fully formulated oils cannot provide the most helpful information to solve the concern of this work. Therefore, no more details of related literature are given in this work.

1.4.3 Effect of contact pressure

The number of researches dealing with the interaction between DLC and fully formulated lubricant is very limited, and the study on pressure effect is not found. Even though a few studies concentrate on the influence of contact pressure as DLC is employed, the selected lubricants are base oil plus anti-wear, extreme pressure additives or friction modifiers.

For example, Podgornik et al. [41] reported the contact pressure effect in range of 1.0 GPa to 3.0 GPa for steel/DLC mixed contact with the lubricants containing anti-wear and extreme pressure additives. The results indicated that when anti-wear additive is used, the coefficient of friction and wear were almost independent on contact pressure. However, when extreme pressure additive was used, the increase of contact pressure led to a coefficient of friction drop after 5000 cycles. The wear rate also slightly increased as the function of pressure. The further surfaces analyses were not performed and the detailed mechanism was not proposed.

In another study of the group of Spencer [42], the impact of different loads on the chemical composition of tribofilms derived from ZDDP in n-decane was studied using a combinatorial tribological experiment with X-ray photoelectron spectroscopy. The loads were varied between

2.8 and 280MPa calculated by the apparent contact area. According to the findings, as the load increased, there was a corresponding rise in the overall quantity of phosphate detected within the tribo-stressed region.

The outcome of these researches is interesting but it can be very different from those of fully formulated lubricants, due to the ignorance of other additives, for example, detergent additive. The study of contact pressure effect in friction with detergent additive was not found.

References

[1] Hafedh Bouassida. Lubricated piston ring cylinder liner contact: Influence of the liner microgeometry. Mechanics [physics.med-ph]. INSA de Lyon, 2014. English. ⟨NNT: 2014ISAL0088⟩. ⟨tel-01149019⟩

[2] Söderfjäll, M. (2017). Friction in Piston Ring - Cylinder Liner Contacts.

[3] Rahmani, R., Rahnejat, H., Fitzsimons, B., Dowson, D. (2017). The effect of cylinder liner operating temperature on frictional loss and engine emissions in piston ring conjunction. Applied Energy, 191, 568–581. https://doi.org/10.1016/j.apenergy.2017.01.098

[4] Martinella, R. (1993). Selection and application of wear-resistant materials to increase service life of components. Ceramics International, 19(6), 375–389. https://doi.org/10.1016/0272-8842(93)90027-o

[5] Donnet, C., Erdemir, A., Robertson, J. (2010). Tribology of diamond-like carbon films: Fundamentals and applications. Springer.

[6] Dorner-Reisel, A., Lieberwirth, R., Svoboda, S., Günther, K., Röder, C., Himcinschi, C., Irmer, G., Weißmantel, S. (2014). Wear behaviour of hydrogen free diamond-like carbon thin films in diesel fuel at different temperatures. Diamond and Related Materials, 44, 78–87. https://doi.org/10.1016/j.diamond.2014.01.013

[7] Lubwama, M., Corcoran, B., Sayers, K. (2014). DLC films deposited on rubber substrates: A Review. Surface Engineering, 31(1), 1–10. https://doi.org/10.1179/1743294414y.0000000379

[8] Tung, S. C., Gao, H. (2002). Tribological investigation of piston ring coatings operating in an alternative fuel and Engine Oil Blend. Tribology Transactions, 45(3), 381–389. https://doi.org/10.1080/10402000208982563

[9] Beake, B. D., Liskiewicz, T. W., Vishnyakov, V. M., Davies, M. I. (2015). Development of DLC coating architectures for demanding functional surface applications through nano- and micro-mechanical testing. Surface and Coatings Technology, 284, 334–343. https://doi.org/10.1016/j.surfcoat.2015.05.050

[10] Phelps, A. W. (n.d.). Materials selection for wear resistance. Handbook of Materials Selection, 1275–1286. https://doi.org/10.1002/9780470172551.ch41

[11] Kano, M. (2014). Diamond-like carbon coating applied to automotive engine components. Tribology Online, 9(3), 135–142. https://doi.org/10.2474/trol.9.135

[12] Vetter, J. (2014). 60 years of DLC coatings: Historical highlights and technical review of cathodic arc processes to synthesize various DLC types, and their evolution for Industrial Applications. Surface and Coatings Technology, 257, 213–240. https://doi.org/10.1016/j.surfcoat.2014.08.017

[13] Tas, M. O., Banerji, A., Lou, M., Lukitsch, M. J., Alpas, A. T. (2017). Roles of mirror-like surface finish and DLC coated piston rings on increasing scuffing resistance of cast iron cylinder liners. Wear, 376-377, 1558–1569. https://doi.org/10.1016/j.wear.2017.01.110

[14] Rejowski, E. D., Mordente Sr, P., Pillis, M. F., Casserly, T. (2012). Application of DLC coating in cylinder liners for friction reduction. SAE Technical Paper Series. https://doi.org/10.4271/2012-01-1329

[15] Mobarak, H. M., Masjuki, H. H., Mohamad, E. N., Rahman, S. M. A., Mahmud, K. A. H. A., Habibullah, M., & Salauddin, S. (2014). Effect of DLC coating on tribological behavior of cylinder liner-piston ring material combination when lubricated with jatropha oil. Procedia Engineering, 90, 733–739. https://doi.org/10.1016/j.proeng.2014.11.805

[16] Kano, M. (2015). Overview of DLC-Coated Engine Components. In: Cha, S., Erdemir, A. (eds) Coating Technology for Vehicle Applications. Springer, Cham. https://doi.org/10.1007/978-3-319-14771-0_3

[17] Schmellenmeier, H. Die (1953). Beeinflussung von festen Oberflachen durch eine ionisierte. Exp. Té-ech. Phys. 1, 49–68.

[18] Schmellenmeier, H (1956). Carbon layers with diamond structure. Phys. Chem. 205, 349–360.

[19] König, H.; Helwig, G. Z (1951). Thin Layers Formed from Hydrocarbons by Electron or Ion Bombardment. Phys., 129, 491–503.

[20] Heisen, A (1958). Über die Bildung dünner Kohleschichten in einer in Benzolatmosphäre brennenden Glimmentladung. Ann. Phys., 457, 23–35.

[21] Aisenberg, S. (1971); Chabot, R. Ion-beam deposition of thin films of diamondlike carbon. J. Appl. Phys., 42, 2953–2958.

[22] Aisenberg, S. (1973); Chabot, R. Physics of ion plating and ion beam deposition. J. Vac. Sci. Technol, 10, 104–107.

[23] Spencer, E.G.; Schmidt, P.H.; Joy, D.C.; Sansalone, F (1976). Ion-beam-deposited polycrystalline diamondlike films. J. Appl. Phys. Lett., 29, 118–120.

[24] Whitmell, D.S.; Williamson, R (1976). The deposition of hard surface layers by hydrocarbon cracking in a glow discharge. Thin Solid Films, 35, 255–261.

[25] Holland, L (1977). Some characteristics and uses of low-pressure plasmas in materials science. J. Vac. Sci. Technol., 14, 5–15.

[26] Bewilogua, K., & Wagner, D. (1991). The effect of secondary electrons in the ion plating deposition of amorphous hydrogenated carbon (A-C:h) films. Vacuum, 42(7), 473–476. https://doi.org/10.1016/0042-207x(91)90019-f

[27] Mobarak, H. M., Masjuki, H. H., Mohamad, E. N., Rahman, S. M. A., Mahmud, K. A. H. A., Habibullah, M., & Salauddin, S. (2014). Effect of DLC coating on tribological behavior of cylinder liner-piston ring material combination when lubricated with jatropha oil. Procedia Engineering, 90, 733–739. https://doi.org/10.1016/j.proeng.2014.11.805

[28] McKenzie, D. R. (1996). Tetrahedral bonding in amorphous carbon. Reports on Progress in Physics, 59(12), 1611–1664. https://doi.org/10.1088/0034-4885/59/12/002

[29] Weiler, M., Sattel, S., Jung, K., Ehrhardt, H., Veerasamy, V. S., & Robertson, J. (1994). Highly tetrahedral, diamond‐like amorphous hydrogenated carbon prepared from a plasma beam source. Applied Physics Letters, 64(21), 2797–2799. https://doi.org/10.1063/1.111428

[30] Sánchez-López, J. C., Erdemir, A., Donnet, C., Rojas, T. C. (2003). Friction-induced structural transformations of diamondlike carbon coatings under various atmospheres. Surface and Coatings Technology, 163-164, 444–450. https://doi.org/10.1016/s0257-8972(02)00641-2

[31] Grischke, M., Hieke, A., Morgenweck, F., Dimigen, H. (1998). Variation of the wettability of DLC-coatings by network modification using silicon and oxygen. Diamond and Related Materials, 7(2-5), 454–458. https://doi.org/10.1016/s0925-9635(97)00237-9

[32] Donnet, C. (1998). Recent progress on the tribology of doped diamond-like and carbon alloy coatings: A Review. Surface and Coatings Technology, 100-101, 180–186. https://doi.org/10.1016/s0257-8972(97)00611-7

[33] Cutiongco, E. C., Li, D., Chung, Y.-W., Bhatia, C. S. (1996). Tribological behavior of amorphous carbon nitride overcoats for magnetic thin-film rigid disks. Journal of Tribology, 118(3), 543–548. https://doi.org/10.1115/1.2831572

[34] Qian, F., Craciun, V., Singh, R. K., Dutta, S. D., Pronko, P. P. (1999). High intensity femtosecond laser deposition of diamond-like carbon thin films. Journal of Applied Physics, 86(4), 2281–2290. https://doi.org/10.1063/1.371043

[35] Garrelie, F., Loir, A. S., Donnet, C., Rogemond, F., Le Harzic, R., Belin, M., Audouard, E., Laporte, P. (2003). Femtosecond pulsed laser deposition of diamond-like carbon thin films for Tribological Applications. Surface and Coatings Technology, 163-164, 306–312. https://doi.org/10.1016/s0257-8972(02)00481-4

[36] Vetter, J. (2014). 60 years of DLC coatings: Historical highlights and technical review of cathodic arc processes to synthesize various DLC types, and their evolution for Industrial Applications. Surface and Coatings Technology, 257, 213–240. https://doi.org/10.1016/j.surfcoat.2014.08.017

[37] Celii, F. G., Butler, J. E. (1991). Diamond chemical vapor deposition. Annual Review of Physical Chemistry, 42(1), 643–684. https://doi.org/10.1146/annurev.pc.42.100191.003235

[38] Tung, S. C., Gao, H. (2003). Tribological characteristics and surface interaction between piston ring coatings and a blend of energy-conserving oils and ethanol fuels. Wear, 255(7-12), 1276–1285. https://doi.org/10.1016/s0043-1648(03)00240-0

[39] Tamura, Y., Zhao, H., Wang, C., Morina, A., Neville, A. (2016). Interaction of DLC and B4C coatings with fully formulated oils in boundary lubrication conditions. Tribology International, 93, 666–680. https://doi.org/10.1016/j.triboint.2015.02.029

[40] Kosarieh, S., Morina, A., Lainé, E., Flemming, J., Neville, A. (2013). Tribological performance and tribochemical processes in a DLC/steel system when lubricated in a fully formulated oil and base oil. Surface and Coatings Technology, 217, 1–12. https://doi.org/10.1016/j.surfcoat.2012.11.065

[41] Podgornik, B., Sedlaček, M., & Vižintin, J. (2007). Influence of contact conditions on tribological behaviour of DLC coatings. Surface and Coatings Technology, 202(4-7), 1062-1066. https://doi.org/10.1016/j.surfcoat.2007.07.040

[42] Eglin, M., Rossi, A. & Spencer, N.D. (2003). X-ray Photoelectron Spectroscopy Analysis of Tribostressed Samples in the Presence of ZnDTP: A Combinatorial Approach. Tribology Letters 15, 199–209. https://doi.org/10.1023/A:1024805001625

Chapter 2 Materials and methods

This section provides details on the materials, lubricants and specific sliding conditions employed in tribological tests, and the characterization techniques used for sample analysis.

2.1 Materials

The a-C:H DLC coating used in this work was prepared by HEF IREIS. This DLC coating is composed of approximately 20% of hydrogen and 80% of carbon. This type of DLC is currently used in certain mechanical contacts in internal combustion engine. As part of the deposition process, a supplemental layer was added to the steel surfaces to enhance the adherence of the DLC films and minimize residual stresses. The thickness of coating is 2µm, deposited on well-polished steel rings, steel disks and steel balls. The steel disks have a diameter of 25 mm and a thickness of 7 mm, and are made of M2 steel. The steel rings and balls were made of 100Cr6 steel. The rings have a diameter of 35 mm and a contact length of 8 mm, and the balls have a radius of 10 mm. The photos of all the materials used in this work are shown in Figure 2.1.

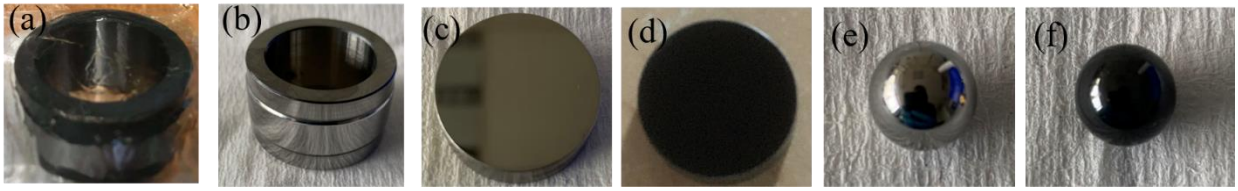

Fig. 2.1 The photos of (a) steel ring (b) a-C:H ring (c) steel disk (d) a-C:H disk (e) steel ball and (f) a-C:H ball

The surface roughness of test materials is measured by interferometer, ContourGT-X, Bruker, and listed in Table 2.1. The roughness parameters, Sa and Sq, can be exported directly. In order to avoid the inaccuracy of measurements, at least 3 different surface areas are characterized on each sample, accompanying with at least 2 specific magnifications which are depending on the predicted roughness before the test. For example, 25x objective is selected for the not polished steel ring, while that of 100x is used to measure other smoother materials. The hardness, the elastic

modulus and the composition of the materials are also listed in Table 2.1. The measurement details are reported elsewhere [1].

Tab. 2.1 Surface roughness of materials before tests (steel ring has two types: surface not polished and surface polished)

	Steel ring	Steel ball	Steel disk	a-C:H ring	a-C:H ball	a-C:H disk
Sa (nm)	220 ±20 30±10	24 ±5	7 ±2	30 ±5	22 ±5	7 ±2
Sq (nm)	260 ±20 50±10	30 ±5	8 ±2	50 ±5	28 ±5	8 ±1
Hardness	223HB		64HRC		27GPa	
Elastic modulus	210GPa				259GPa	
Composition	0.95% C, 0.25% Mn, 0.15% Si, 1.5% Cr		0.85% C, 6% W, 5% Mo, 4% Cr, 2% V		20% H, 80% C	

2.2 Lubricants and additives

A commercial fully formulated ELF SXR 900 5W30 engine oil was selected for this work. The base oil of this fully formulated lubricant was used as a reference to understand the tribological

performances of the fully formulated lubricant and highlight the tribo-chemical reactivity of the additive's compounds. The basic information of these two lubricants is summarized in Table 2.2.

Tab. 2.2 Basic information of the fully formulated lubricant and the base oil.

	Fully formulated oil	Base oil
Kinematic viscosity (100°C)	9.3 cst	3.6 cst
Density (15°C)	857kg/m^3	/
Viscosity index	170	/
T. B. N.	10mgKOH/g	/

In order to have a basic recognition on the composition of fully formulated lubricant, X-ray photoelectron spectroscopy (XPS) was performed. The additives were obtained by liquid-liquid extraction, also known as solvent extraction, which is a process where two solutions that do not mix are brought into contact to extract one or more constituents through the transfer of matter.

In our research, we used methanol (ChimiePlus, content>99%) as a solvent to extract the chemical components present in the lubricant. Methanol was selected for its ability to extract substances without causing any chemical modifications and for its significant volatility. The need for high temperatures to facilitate evaporation and isolate the solutes is then unnecessary. The lubricants were placed separately in two tubes. Each tube contained methanol with a volume four times greater than that of the lubricant. A larger volume of solvent compared to the liquid being extracted leads to improved extraction efficiency [2]. The resulting mixture was agitated for 30 minutes to

enhance the transfer of additives to methanol. After the mixture settled, a small amount of methanol was collected using a pipette and deposited onto a substrate, in our case a steel disk exposed to air. Upon confirming the evaporation of methanol, the steel disk was placed on a sample holder and analyzed using XPS.

The survey spectrum is displayed in Fig. 2.2. The characteristic elements of P, S, Zn and Ca were obtained, which could be originated from ZDDP and calcium carbonate detergent additives present in the fully formulated engine oil. In order to compare the binding energy of the chemical elements before and after friction tests, the characteristic elements were accurately analyzed doing high resolution XPS. The corresponding deconvoluted high resolution spectra are shown in Fig. 2.3. The detailed fitting strategy is presented in section 2.5.4 for this purpose. The contributions of C1s located at 284.8 eV, 286.2 eV, 287.6 eV and 289.8eV were assigned as C-C, C-O, C=O and carbonate, respectively. The O1s contains C=O (530.4 eV), C-O (531.8eV) and a peak at 533.4eV which could be related to water molecules. The Ca2p3/2 photopeak confirms the presence of calcium carbonate by the contribution located at 347.3eV. The phosphorous is mainlyin P-O form with a binding energy at 133.1 eV. The sulphide S-Zn chemical bond was confirmed by S2p3/2 located at 161.4 eV. This chemical bond was justified by Zn2p3/2 located at 1021.2eV. The survey spectra and the Ca2p3/2, P2p, S2p and Zn2p3/2 photopeaks indicate the presence of calcium carbonate overbased detergent and ZDDP-like antiwear additives in the fully formulated lubricant. It should be noted that no trace of molybdenum is detected, indicating that no friction modifier containing Mo element is present in this 5W30 engine oil.

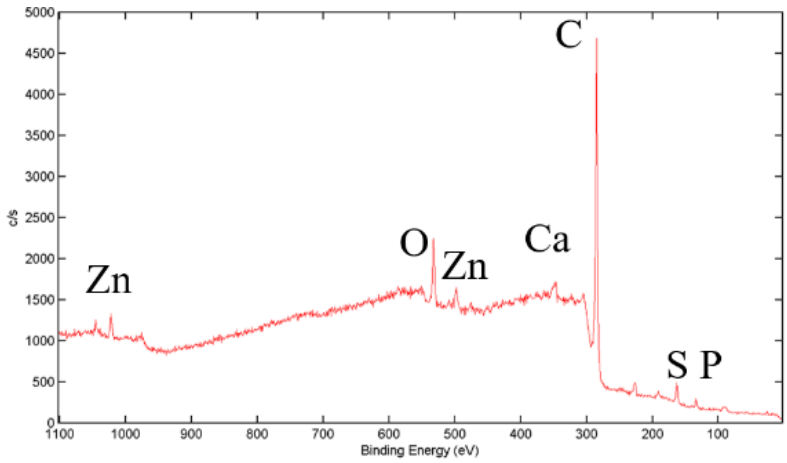

Fig. 2.2 XPS survey spectrum of fully formulated 5W30 engine oil

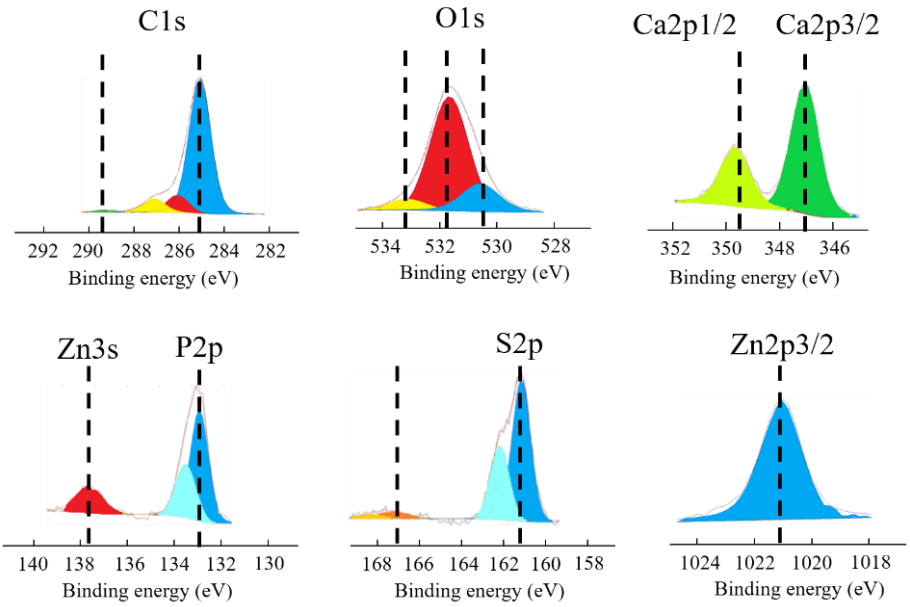

Fig. 2.3 High resolution XPS spectra of C1s, O1s, Ca2p, P2p, S2p and Zn2p3/2 of fully formulated 5W30 engine oil

The detergent additive used in the fully formulated ELF SXR 5W30 engine oil was provided by TotalEnergies, France, in order to perform sliding tests with the base oil blended with only detergent additive. The details of this detergent are confidential.

2.3 Reciprocating sliding tests

2.3.1 Ring-on-disk reciprocating tribometer

Ring-on-disk sliding tests were performed in HEF IREIS company by using a homemade reciprocating tribometer. A detailed description of the tribometer is shown in Fig. 2.4 (a). The range of ring rotational speed is between 10 and 3000 rpm which is set by an electric motor. The applied normal force (obtained by a pneumatic actuator) can be in the range of 50N to 5000N. The reciprocating sliding speed of the flat is fixed at 1 mm/s in order to keep a line contact configuration even if there is wear on the flat. The stroke length can be between 0 – 20mm. The heating system is available from 0°C to 120°C (test samples immersed in the oil, volume 1.6L). The selection of this configuration is to simulate the contact of PRCL in the most severe conditions.

Fig. 2.4(b) shows a schematic of the ring-on-disk tribo-pair. The flat moves reciprocally, on which the normal force is applied. The rotation speed of ring was gradually decreased, and the steady state of CoF at each rotation speed was recorded. The detailed contact conditions are introduced in Tab. 2.2. The tribopairs were steel ring (not polished)-on-a-C:H disk, steel ring (polished)-on-steel disk and a-C:H ring-on-a-C:H disk. The aim to use polished steel ring for steel self-mated contact is to ensure the contact between two surfaces is well-aligned during the test.

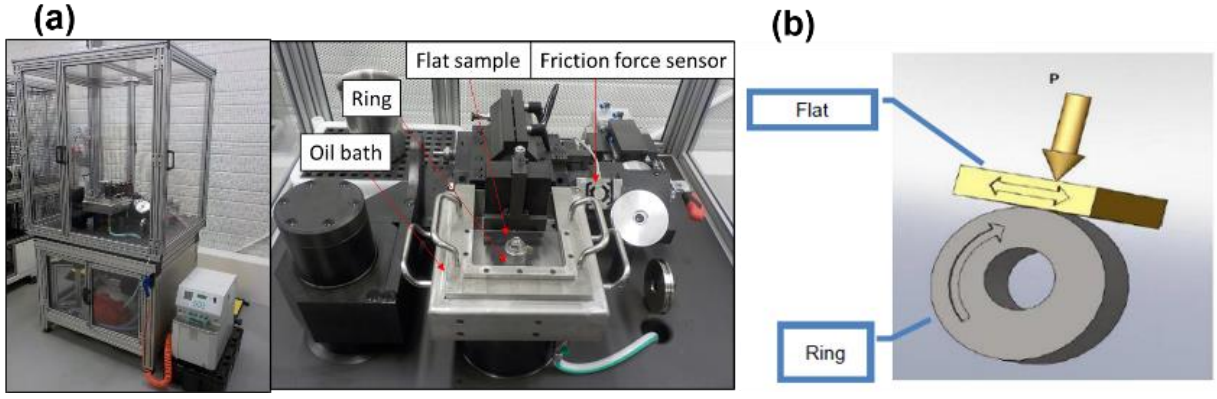

Fig. 2.4 (a) Ring-on-disk tribometer at HEF-IREIS company (b) schematic ring-on-disk contact

Tab. 2.2 Operating Contact parameters for ring-on-disk reciprocating tests

Temperature (°C)	100
Applied load (N)	400, 950, 2100 and 3800
Maximum hertzian Pressure (GPa)	320, 500, 740 and 1
Stroke length of disk (mm)	1
Rotation speed of ring (m/s)	2.66, 2.38, 2.16, 1.83, 1.56, 1.43, 1.21, 1.01, 0.82, 0.64
Test duration (min)	40

2.3.2 Ball-on-disk

The ball-on-disk reciprocating sliding tests were also performed in order to compare with ring-on-disk reciprocating tests. These tests were performed in LTDS with a homemade low load linear reciprocating tribometer [3]. A normal load up to 10 N (recommended) can be applied through the ball specimen. The sensibility of the tangential force is around 0.005 N. A picture of this tribometer is shown in Fig. 2.5(a). The disk is fixed and its surface was covered by 0.5ml tested lubricant before starting the test (Fig. 2.5b). The load was applied through the ball which moves reciprocally (Fig. 2.5c). Friction tests were performed with steel ball-on-steel disk, a-C:H ball-on-steel disk and a-C:H ball-on-a-C:H disk configurations. The detailed contact parameters are listed in Tab. 2.3.

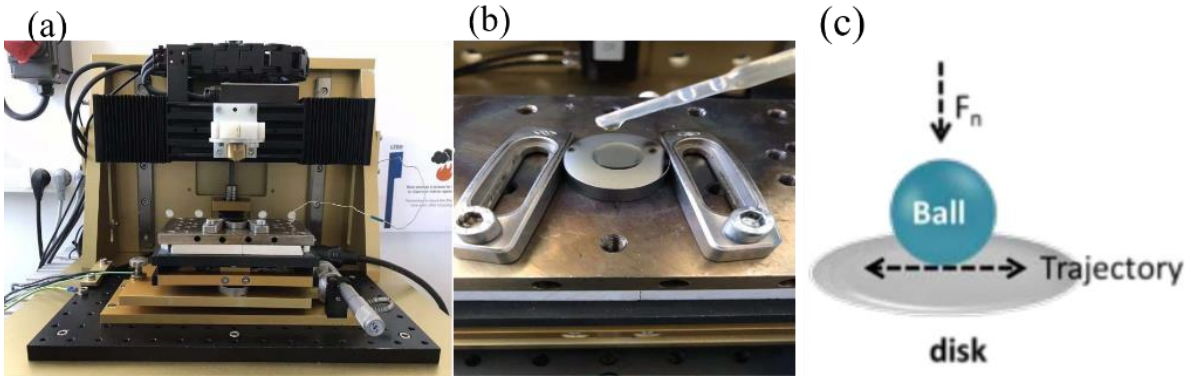

Fig. 2.5 (a) the assembling of low load ball-on-disk tribometer (b) testing materials surface covered by oil droplets and (c) schematic of tribo-pair

Tab. 2.3 Contact parameters for ball-on-disk configuration

Temperature (°C)	100
Applied load (N)	1.4 and 9.5
Maximum hertzian Pressure (GPa)	0.5 and 1.0
Stroke length of disk (mm)	7.5
Test duration (min)	200 (12000 cycles)

2.4 Friction regime estimations (λ calculations)

Here, the as-designed elasto-hydrodynamic lubrication (EHL) film thickness and λ calculations were calculated by following the methods described in references [4,5,6]. In the case of ring-on-disk configuration, the thickness of the fluid film varied between 60nm and 210nm. Therefore, steel ring (not polished)/a-C:H disk was in boundary/mixed lubrication regimes, while steel ring (polished)/steel disk and a-C:H ring/a-C:H disk were in mixed/elasto-hydrodynamic lubrication

regimes. For ball-on-disk configuration, the thickness of the fluid film was around 3nm. Therefore, all the tests were performed in boundary lubrication regime. The post-test λ values and corresponding lubrication regimes were also calculated. They will be introduced in each corresponding chapter.

2.5 Surface characterization techniques

2.5.1 Interferometer

The wear volumes of the samples were assessed using an optical white light interferometer (Contour GT-K1, Bruker). In cases where the wear tracks were too large to be captured in a single image, a stitching procedure was employed to capture and merge multiple images to obtain the complete wear track. To correct the baseline of the sample, a terms removal technique (F-operator) was utilized. Figure 2.6 illustrated the original measurement on a ball (left) and the aligned image (right). To quantify the wear (negative volume), a mask was applied to restrict the analysis area near the wear track and minimize measurement errors.

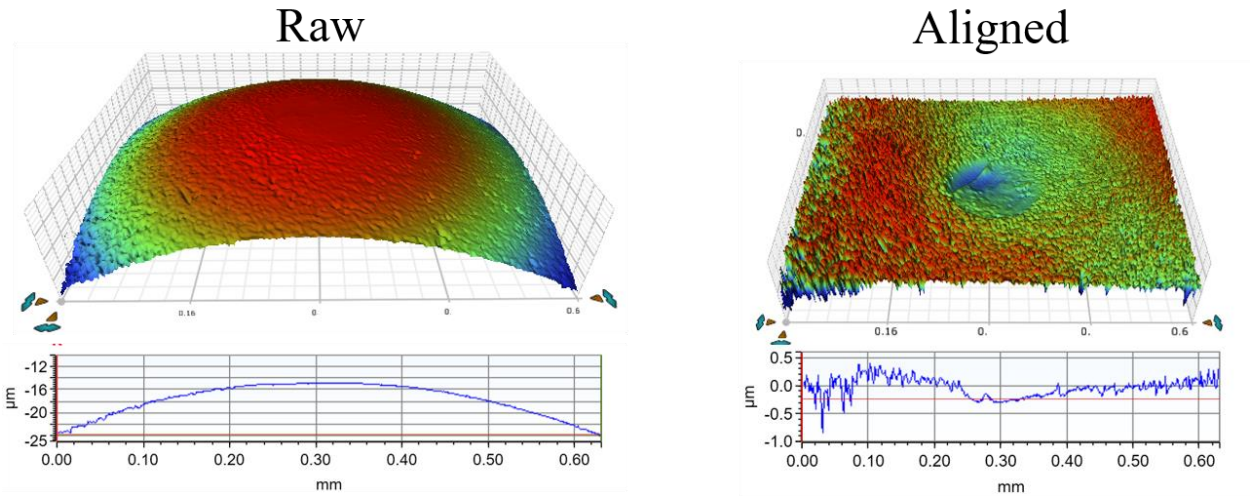

Fig. 2.6 Optical interferometer measurements of a ball: raw (left) and aligned (right)

2.5.2 AFM

To analyze the surface characteristics both inside and outside of the wear tracks, AFM (Atomic Force Microscopy) measurements were conducted using a NX 10 instrument from Park Instruments. The AFM operated in standard Contact Mode.

Initially, the cantilever and tip were mounted on the holder and carefully aligned with the photodetector to achieve a signal intensity of around 3.0 V, with lateral and vertical deviations of less than 0.1 V each. Once the alignment was satisfactory, the tip was automatically approached to the surface to initiate the measurements. The AFM captured images with 20x20 μm^2 size in the region of interest, with a resolution of 256x256 pixels. To prevent damage on the AFM tip, the scanning speed was maintained below 0.5 Hz per line. The collected data was processed, including baseline correction, and analyzed using Gwyddion software.

2.5.3 SEM analysis

After having conducting tribological tests, the topography and chemical composition of the rubbed surfaces were characterized. This analysis was carried out using Scanning Electron Microscopy (SEM) with a FEI XL30-FEG instrument. The SEM was equipped with an Everhardt-Thornley secondary electron detector and operated under high vacuum conditions. The acceleration voltage used for the imaging of steel samples was 20kV, while for a-C:H DLC samples it was 9kV (DLC is less conductive than steel). To investigate the chemical composition of the surfaces, Energy Dispersive X-Ray Spectroscopy (EDS) was employed. The EDS analysis utilized an Oxford Instruments X-max silicon drift detector with an ultra-thin window measuring 80 mm^2. Quantitative analysis of the obtained EDS spectra was performed using the Aztec software. Notably, no conductive coating was applied to the surfaces during these observations.

2.5.4 XPS analysis

After the friction tests, the samples underwent a cleaning process in an ultrasonic bath with n-heptane (Chimie Plus: > 99%) for 10 minutes. This step aimed to eliminate any remaining oil residues. Throughout the cleaning procedure, the samples were handled using metallic tweezers to prevent contact with their surfaces. Subsequently, X-ray Photoelectron Spectroscopy (XPS) analysis was performed on the samples using an ULVAC-PHI Versa Probe III spectrometer. The spectrometer was equipped with a monochromatic Al Kα X-ray source, which had a beam diameter varying between 10µm and 200µm. The binding energy scale was calibrated using the C1s photo-peak at a binding energy of 284.8 eV, with an estimated binding energy error of ±0.1 eV. The analysis procedure began with a survey spectrum using a pass energy of 224 eV to identify all the elements present on the sample surfaces. Subsequently, narrower scans with a 20 eV range were acquired using a pass energy of 13 eV. These scans aimed to accurately determine the chemical state of each element and enable quantitative analysis using PHI Multipack software. The background contribution was approximated using the Shirley method, and Wagner sensitivity factors (accounting for the apparatus's transmission function) were employed to calculate the atomic concentrations. The quantification analysis was realized by survey spectrum in at least three zones with the beam diameter of 200 µm for ring/disk. The as large as possible beam diameter was selected for ball/disk tribopair (depending on the size of wear track). The average value of the analyses was calculated.

To prepare the sample surfaces for analysis, an Argon ion beam was utilized to sputter the surfaces at a 45° angle. The ion beam was accelerated at 250 V with a current density of 120 nA mm^{-2}. In addition, digital photographs of the samples were taken to identify the wear tracks. In cases where the wear tracks were not clearly visible in the photographs, particularly for ball samples, Scanning

X-ray Imaging (SXI) was performed to obtain a chemical contrast between the inside and outside of the wear tracks (refer to Figure 2.7).

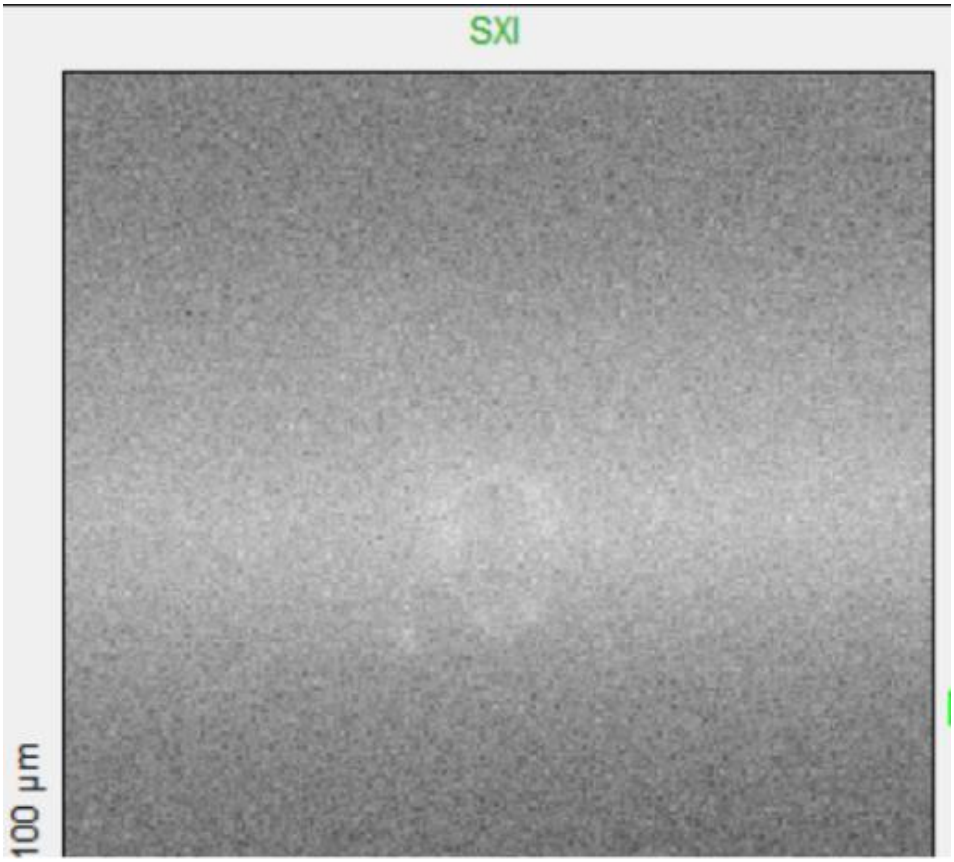

Fig. 2.7 SXI image to localize the position of wear track (white circle at center of the ball)

2.5.5 FIB machining and TEM analysis

A cross-section of the flat wear track was prepared at Manutech-USD using Dual Beam Focused Ion Microscopy. To protect the steel and a-C:H DLC surfaces during milling and prevent re-deposition, a platinum layer was deposited using a platinum gaseous precursor. The platinum layer was deposited in two steps: first, a low-energy electron beam was used to minimize damage on the DLC surface, and then a high-energy Ga ion beam was employed to accelerate the growth rate of the protective platinum film.

The resulting thin cuts were analyzed using Transmission Electron Microscopy (TEM) with a Jeol 2100F-UHR TEM instrument. The TEM was equipped with a Schottky field emission gun operating at 200 kV. Bright field images were captured using a Gatan Orius 100 CCD camera, while High-Angle Annular Dark Field (HAADF) images were acquired in Scanning Transmission Electron Microscopy (STEM) mode. For local chemical analysis, EDX (Energy Dispersive X-ray Spectroscopy) was performed using an 80 mm^2 silicon drift detector from Oxford Instruments, generating spectra or elemental maps. The EDX quantification analysis was performed in at least three zones to check the repeatability.

In the case of the thin cuts obtained from the not polished steel ring/a-C:H disk at a maximum pressure of 740 MPa, analysis was also conducted using a FEI Titan ETEM G2 electron microscope operated at 300 keV, which provides very high resolution and imaging quality. This electron microscope is equipped with a Cs image aberration corrector. Prior to analysis, the samples were plasma-cleaned with Argon for 30 seconds to prevent contamination. Compositional analyses in TEM mode were carried out using an energy dispersive X-ray spectrometer (SSD X-max 55 mm^2 from Oxford Instruments).

2.5.6 Fourier Transform Infra-Red (FTIR) Spectrometer

To complement surface chemical analyses, FTIR analysis was carried out on ring-on-disk samples using a JASCO FT/IR-6600 spectrometer. The resolution was 4.0cm^{-1} with a corresponding aperture diameter of 7.1mm. The data was exported by software SpectraManager^{TM}.

References

[1] Salinas Ruiz, V. R., Kuwahara, T., Galipaud, J., Masenelli-Varlot, K., Hassine, M. B., Héau, C., Stoll, M., Mayrhofer, L., Moras, G., Martin, J. M., Moseler, M., de Barros Bouchet, M.-I. (2021). Interplay of mechanics and chemistry governs wear of diamond-like carbon coatings interacting with ZDDP-additivated lubricants. Nature Communications, 12(1). https://doi.org/10.1038/s41467-021-24766-6

[2] Abe, E., Delyle, S.G., Alvarez, J.C.: Extraction liquide-liquide : théorie, applications, difficultés.Ann. Toxicol. Anal. 22, 51–59 (2010). https://doi.org/10.1051/ata/2010018

[3] Guibert, M.; Nauleau, B.; Kapsa, P.; Rigaud, E. CONCEPTION ET REALISATION D'UN TRIBOMETRE ALTERNATIF LINEAIRE. 2006, 11.

[4] Long, Y., Bouchet, M.-I. D., Lubrecht, T., Onodera, T., & Martin, J. M. (2019). Superlubricity of glycerol by self-sustained chemical polishing. Scientific Reports, 9(1). https://doi.org/10.1038/s41598-019-42730-9

[5] Moes, H. (1992). Optimum similarity analysis with applications to elastohydrodynamic lubrication. Wear, 159(1), 57–66. https://doi.org/10.1016/0043-1648(92)90286-h

[6] Yahiaoui, M., Mazuyer, D., & Cayer-Barrioz, J. (2023). IssyOsborne: Transient squeeze and starvation in elastohydrodynamic — OScillating bodies solving Reynolds one-dimensional equation. SoftwareX, 23, 101422. https://doi.org/10.1016/j.softx.2023.101422

Chapter 3 Control of friction in ring-on-disk configuration lubricated by fully formulated lubricant

In this section, the contact pressure effect on tribological behaviors for ring-on-disk configuration is investigated. Different counterpart materials are selected: steel self-mated (polished steel ring), steel (not polished ring)/a-C:H (disk) mixed contact and a-C:H self-mated. The tribo-pairs are lubricated by the previously described fully formulated lubricant. After the tests, surface analyses were carried out to reveal the friction mechanisms.

Introduction

According to the publications, ring-on-disk configuration is not very commonly used comparing to ball-on-disk, cylinder-on-disk or four ball tests in tribological research. The selection of this configuration aimed to simulate the conditions of piston-ring-cylinder-liner (PRCL) mechanical part. Especially when the piston ring is closed to the top dead center (TDC) and bottom dead center (BDC), as introduced in chapter 1. The selected sliding conditions for ring-on-disk configuration (see Tab. 2.2) were slightly severe than the practical PRCL in ICE. After the friction tests, optical microscope, interferometer and Scanning Electron Microscope (SEM) equipped with Energy Dispersive X-ray Spectroscopy (EDS) were employed to characterize the topography and the surface chemical composition. X-ray Photoelectron Spectroscopy (XPS) was carried out to identify the elements present onto the surfaces and their chemical states. Focused Ion Beam (FIB) was used for the cross-section preparations before Transmission Electron Microscope (TEM) observations of the tribofilm. The Fourier Transform Infra-Red (FT-IR) spectroscopy was also used to further analyze the chemical bonds on surface.

3.1 Results

3.1.1 Effect of the contact pressure (steel/a-C:H mixed contact)

3.1.1.1 Tribological results

The friction coefficient as the function of ring rotation speed at 320MPa, 500MPa, 740MPa and 1GPa is shown in Fig. 3.1. According to the Stribeck curve, it is well-known that in boundary/mixed lubrication regime, generally, the CoF raises as the sliding conditions become more severe. In consequence, as the contact pressure increases (for a same ring rotation speed), a higher CoF is expected. In our results, a reduction of the CoF with the increasing pressure is obtained. The Rq values of steel ring and a-C:H DLC after the friction tests are 240 nm ± 20 nm and 9 nm ± 1 nm, they were measured by interferometer (**Fig. A1**). The lubrication regime remains

in boundary/mixed. Therefore, it is unlikely that the friction reduction is simply driven by a self-polishing effect. On the other hand, the decrease of friction as the function of rotation speed can be explained with the Stribeck curve. An in-depth surface analyses on chemical modification induced by the friction test are necessary to understand the friction reduction mechanism.

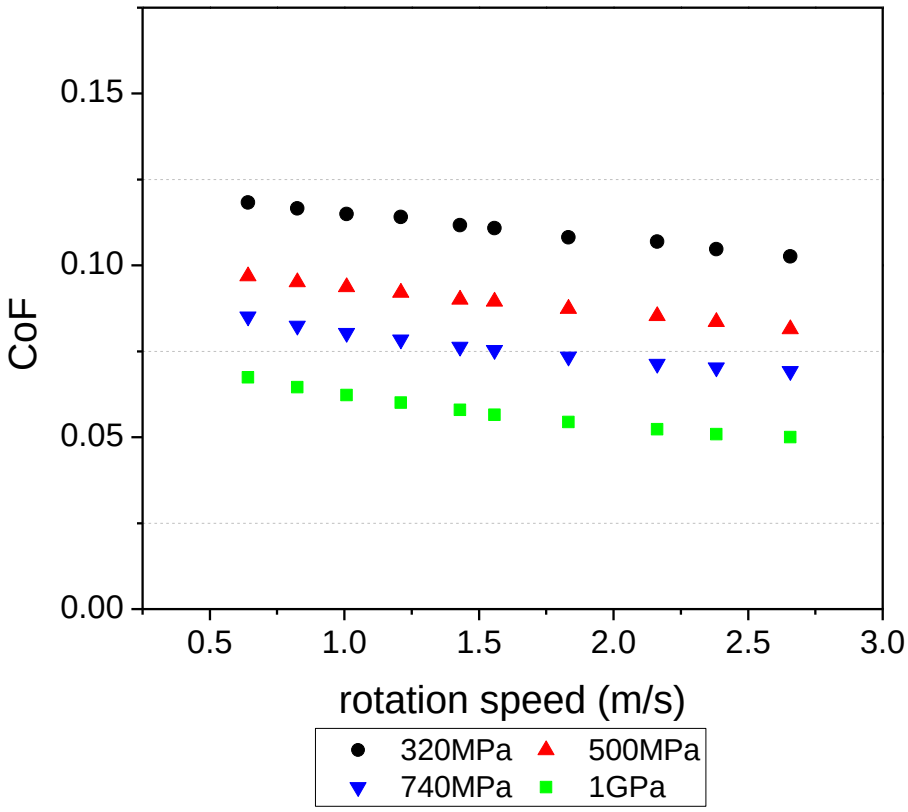

Fig. 3.1 Friction curves of steel/a-C:H at 320MPa, 500MPa, 740MPa and 1GPa

Fig. 3.2 a2, a3, a4 and a5 show the optical images recorded on the wear tracks of a-C:H DLC disks, after the friction tests. Comparing with a1 (no friction), the absence of visible tribofilm can be noticed. This indicates either the presence of a super thin tribofilm, not optically visible, or that only few chemical interactions occur between the a-C:H DLC and the lubricant. In contrary, comparing Fig. 3.2 b1 with b2, b3, b4 and b5, the presence of a tribofilm on the steel ring is

detected although the high surface roughness. The wear on the a-C:H DLC disks is measured and the results are given in Fig. 3.3. For 320MPa, 500MPa and 740MPa, the wear depth on a-C:H DLC fluctuates between 30nm to 50nm, without any correlation with the contact pressure change. At 1GPa, a significant wear (wear depth of 1.75μm, with the range of 0.75mm) is measured on start point of the wear track. On the other surface areas, the wear depth is hard to measure. For the steel ring, mainly due to the high surface roughness, the wear depth or wear volume cannot be easily identified by interferometer or profilometer. The wear can be further confirmed by FIB cut preparation, which will be introduced in the following sections.

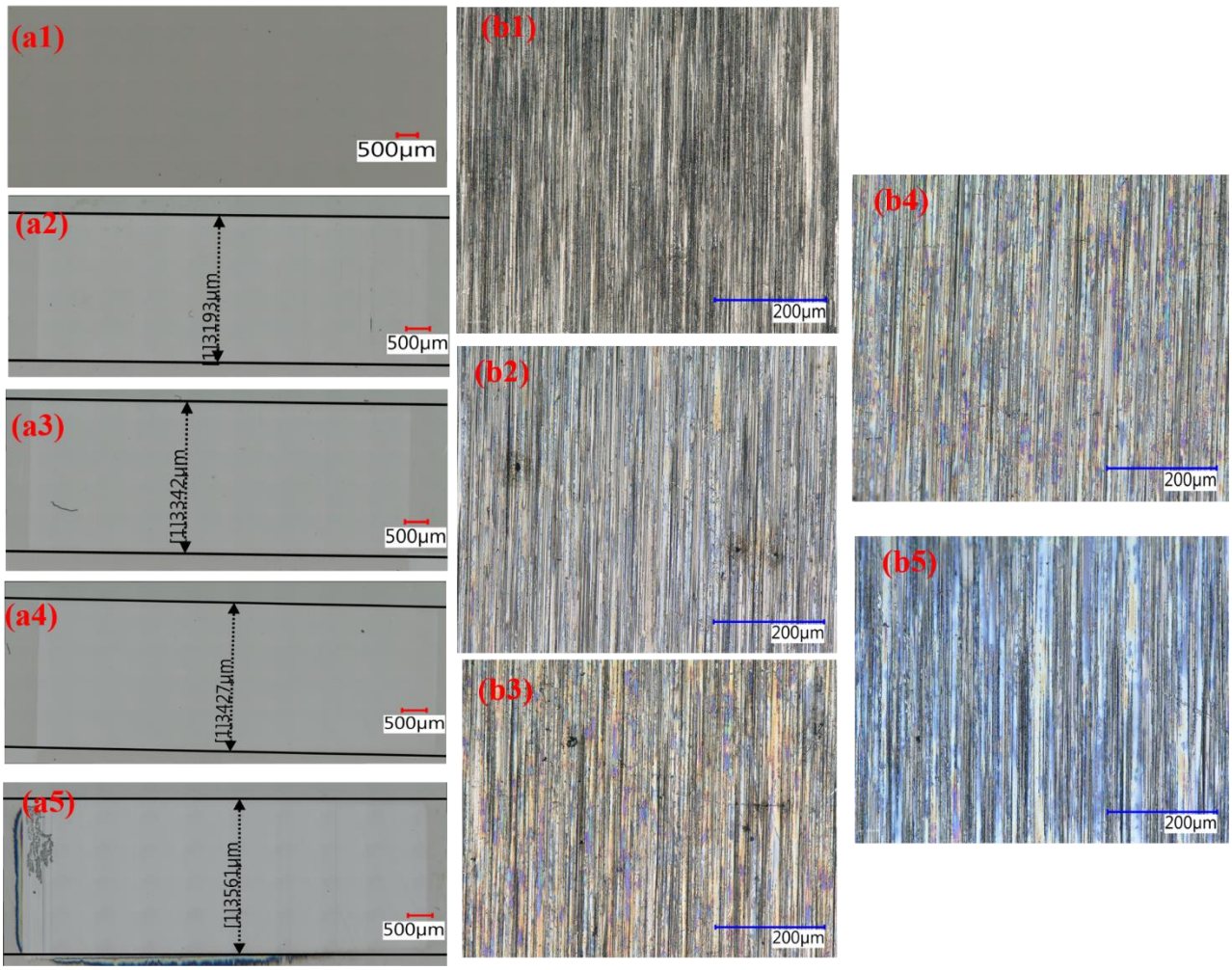

Fig. 3.2 Optical images of a-C:H DLC at 0MPa (a1, no friction), 320MPa (a2), 500MPa (a3), 740MPa (a4) and 1GPa (a5); optical images of steel rings at 0MPa (b1, no friction), 320MPa (b2), 500MPa (b3), 740MPa (b4) and 1GPa (b5).

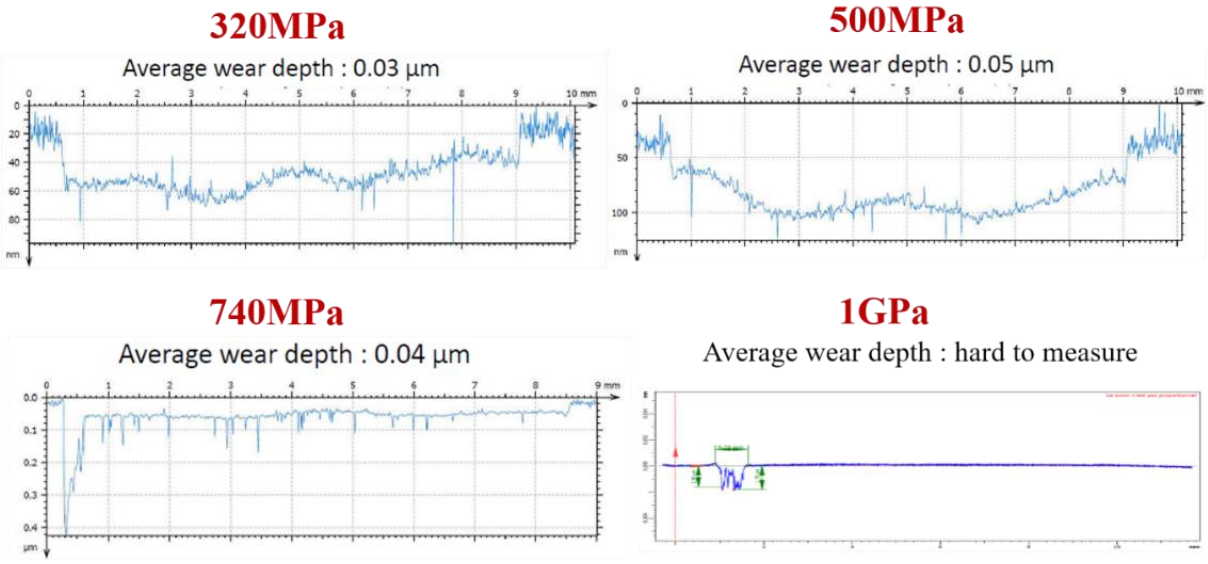

Fig. 3.3 Profiles in wear tracks on a-C:H disks at 320MPa, 500MPa, 740MPa and 1GPa.

3.1.1.2 Surface chemical analysis by XPS

X-ray Photoelectron Spectroscopy (XPS) was used to analyze inside and outside the wear tracks on topmost 10nm of a-C:H DLC disks and steel rings, with the objective to investigate the chemical composition of the rubbed surfaces.

First of all, a distinguishable quantification of characteristic elements is reported. The quantification results of characteristic elements, including P, S, Zn, and Ca on a-C:H disks and steel rings. They are listed in Tab. 3.1 (one significant figures reserved after the decimal point). For a-C:H disks, all elements display a very low concentration and a tendency of decrease as the function of pressure. The low content of these elements is consistent with the optical images (Fig.3 a2-a4) where the tribofilm could hardly be observed. On the counterpart (steel ring), the concentration of P, S, Ca and Zn is found to be higher. Until the contact pressure of 740MPa, the quantity of elements such as S and Zn also tend to decrease with the pressure, while the concentration of phosphorous increases slightly. However, at 1GPa, the concentration of P, S and

Zn dramatically increases. Unlike these elements, a continuously significant increase of the Ca is observed in a ratio of almost 90% at 1 GPa, comparing with 320MPa.

Tab.3.1 Atomic concentration of P, S, Ca and Zn on steel ring and a-C:H DLC disk as the function of pressure

Elements	Atomic concentration (%)							
	Steel ring (MPa)				a-C:H DLC disk (MPa)			
	320	500	740	1000	320	500	740	1000
P	2.0	2.4	2.8	5.3	1.1	0.6	0.2	0.2
S	3.3	2.0	1.8	5.0	0.6	0.6	0.4	0.2
Ca	6.9	9.7	11.1	12.5	2.0	1.3	0.9	0.6
Zn	4.9	3.7	3.4	9.8	0.5	0.4	0.2	0.3

Secondly, the binding energies (BEs) of photo-peaks: C1s, O1s, P2p, S2p, Ca2p3/2, Fe2p3/2, and Zn2p3/2 were analyzed. However, it is difficult to distinguish their chemical shifts induced by different contact loads on both two surfaces (as shown in Fig. A2). Ca2p doublet was fitted by a binding energy difference set at 3.60eV. The area ratio was set at Ca2p3/2 : Ca2p1/2 = 2 : 1. P2p doublet was fitted by a binding energy difference set at 0.84 eV. The area ratio was set at P2p3/2 : P2p1/2 = 2 : 1. S2p doublet was fitted by a binding energy difference set at 1.18 eV. The area ratio was set at S2p3/2 : S2p1/2 = 2 : 1.

Combining with the quantification results, it is interesting to deeply investigate the form of calcium on the steel ring. Fig. 3.4 shows the fitting results for C1s and Ca2p high resolution photo-peaks. A main peak located at about 290eV is observed in C1s for the three contact pressures, which can be assigned to carbonate contribution. On the other hand, the contribution of Ca2p3/2 located at 347.5eV is found to correspond to calcium carbonate. Full-width-half-maximum (FWHM,

identical for all C1s contributions) and detailed binding energy measured for the three pressures are given in Tab. 3.2. The small increase of FWHM of C1s contributions with the pressure is difficult to explain. This is due to the very complex composition of this tribofilm, namely, various source of carbon, such as detergent, anti-wear additive, base oil, etc. The detailed information, including FWHM, binding energy and chemical species assignment of other elements (O, P, S, Fe, Zn) is listed in **Tab. A1**.

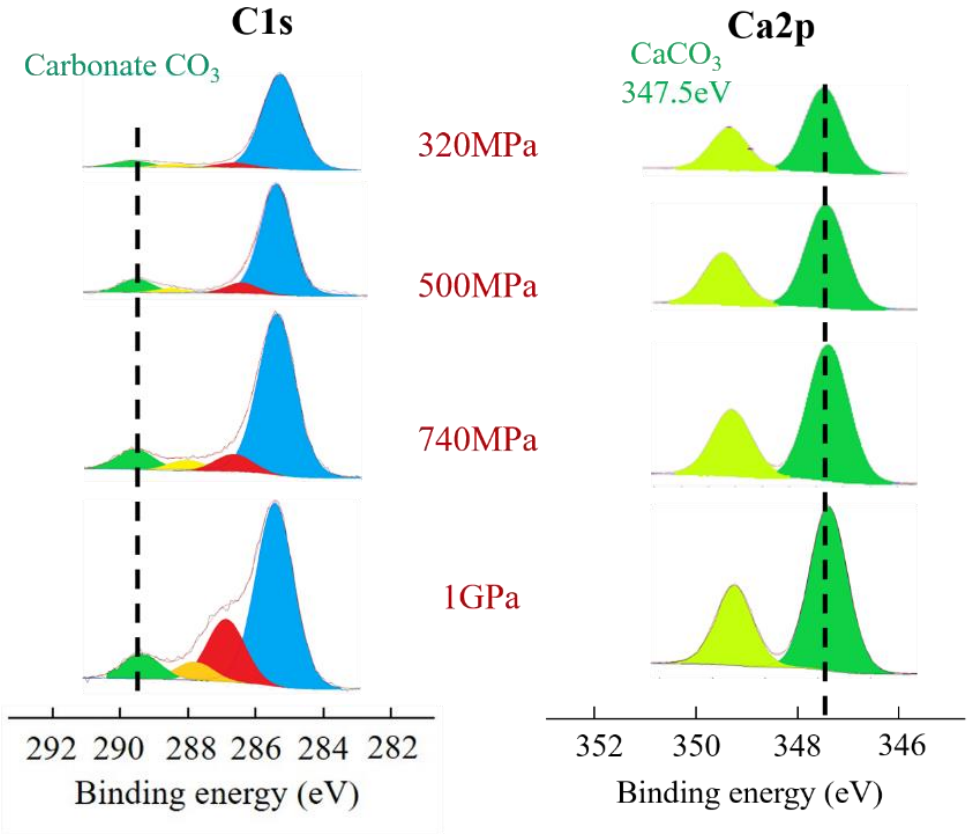

Fig. 4 Photo-peaks fitting for C1s and Ca2p at 320MPa, 500MPa and 740MPa

Tab.3.2 Full-width-half-maximum (FWHM) and binding energies (BE) of C1s and Ca2p3/2 photo-peaks

	Carbonate (C1s)				Ca2p3/2			
	320MPa	500MPa	740MPa	1GPa	320MPa	500MPa	740MPa	1GPa
BE (eV)	289.80	290.08	289.80	289.90	347.39	347.55	347.47	347.59
FWHM	1.39	1.50	1.60	1.64	1.68	1.66	1.59	1.61

The short polyphosphate chains (orthophosphate, pyrophosphate) generally provide relatively lower CoF than long polyphosphate chains (metaphosphate, etc.) [1, 2]. Therefore, it is important to consider the effect of polyphosphate chain length in friction reduction as the function of pressure. The chain length on the steel ring is determined by the area ratio of P2p/Zn3s photo-peaks from XPS fitting results [3-5]. The results are shown in Fig. 3.5. The chain length on a-C:H surfaces was not investigated due to the very low quantity of the characteristic elements. From 320MPa to 740MPa, the chain length grows from the orthophosphate (P/Zn = 0.6) to a mix of pyrophosphate (P/Zn = 1.0) and metaphosphate (P/Zn = 2.0). At 1GPa, the chain length drops back to orthophosphate (P/Zn = 0.6).

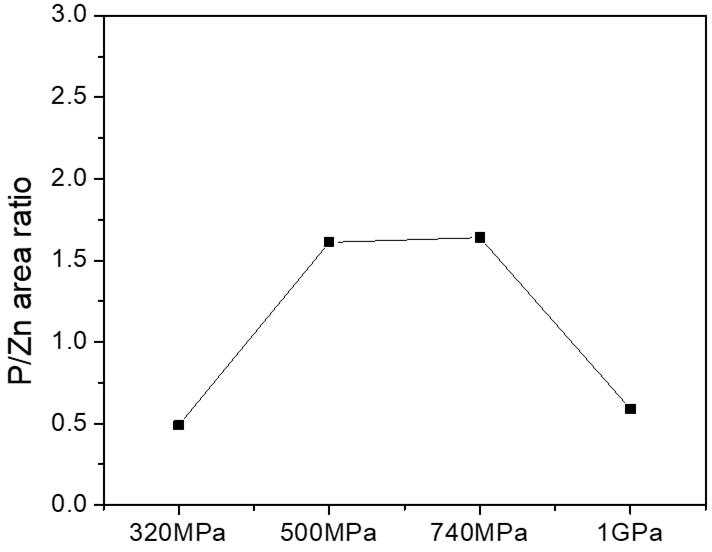

Fig. 3.5 P/Zn area ratio (polyphosphate chain length) calculation on steel ring

It should be noted that the investigation of polyphosphate chain length is realized on the very top surface of the samples rather than in the bulk (estimated 8 nm depth from the surface). Nevertheless, under the same circumstances, calcium quantity shows an increasing tendency with the contact load. On the other hand, plenty of researches have been conducted on the ZDDP polyphosphate chain length. The impact of sliding conditions (contact pressure, temperature, etc.) on ZDDP tribofilm structure and tribological behaviors can be found in many literatures [6-9]. However, given the XPS characterization results in this work, we decided to focalize on the impact of detergent additive on the tribological performances.

3.1.1.3 SEM & TEM characterizations

In order to determine the structure of calcium carbonate compound in the tribofilm formed onto the steel ring surface, TEM-FIB was carried out. First of all, SEM/EDS was used to localize a position rich in calcium element. The SEM/EDS was also performed on a-C:H DLC disks to characterize the surface morphologies. They are reported in Fig. 3.6. For each a-C:H coated disk, two points are selected for Point ID analysis of EDS. Only C and O are found on the surface. This suggests that the characteristic elements on a-C:H disks is very few and the thickness of the tribofilm is very thin. This is consistent with the findings of optical microscope. Fig. 3.7 shows the secondary electron images of steel rings at 320MPa (a), 500MPa (b), 740MPa (c) and 1GPa (d). The mapping results of C, O, P, S, Ca and Zn are presented correspondingly. According to the distribution of these characteristic elements, it is concluded that these elements are rich in dark areas observed on SEM images. The FIB cuts were conducted on these dark areas. Combining the SEM/EDS results of steel ring and a-C:H disks, it can be concluded that the tribofilm is mainly formed on steel rings. The discussion on TEM observations made on FIB cuts are focalized on the steel rings.

320MPa

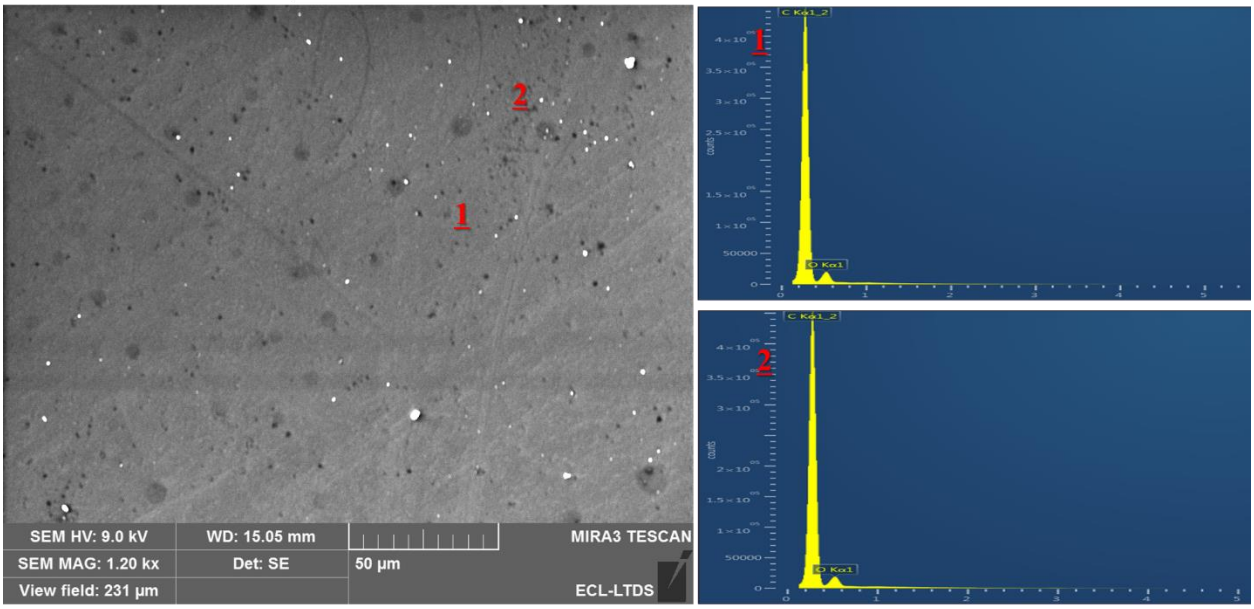

500MPa

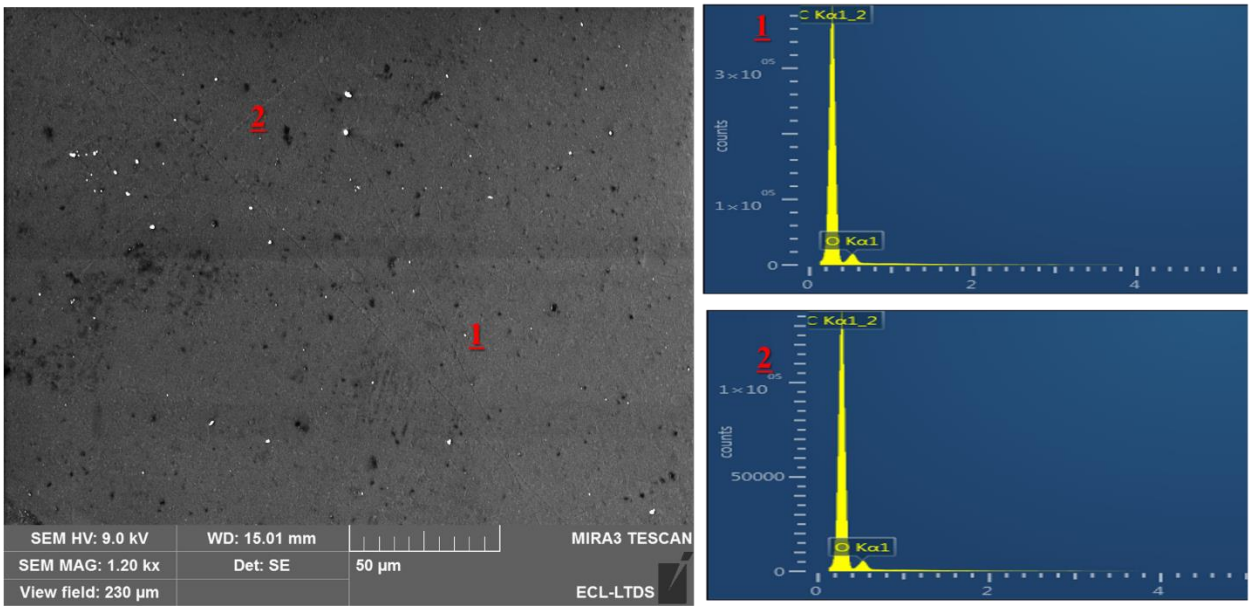

740MPa

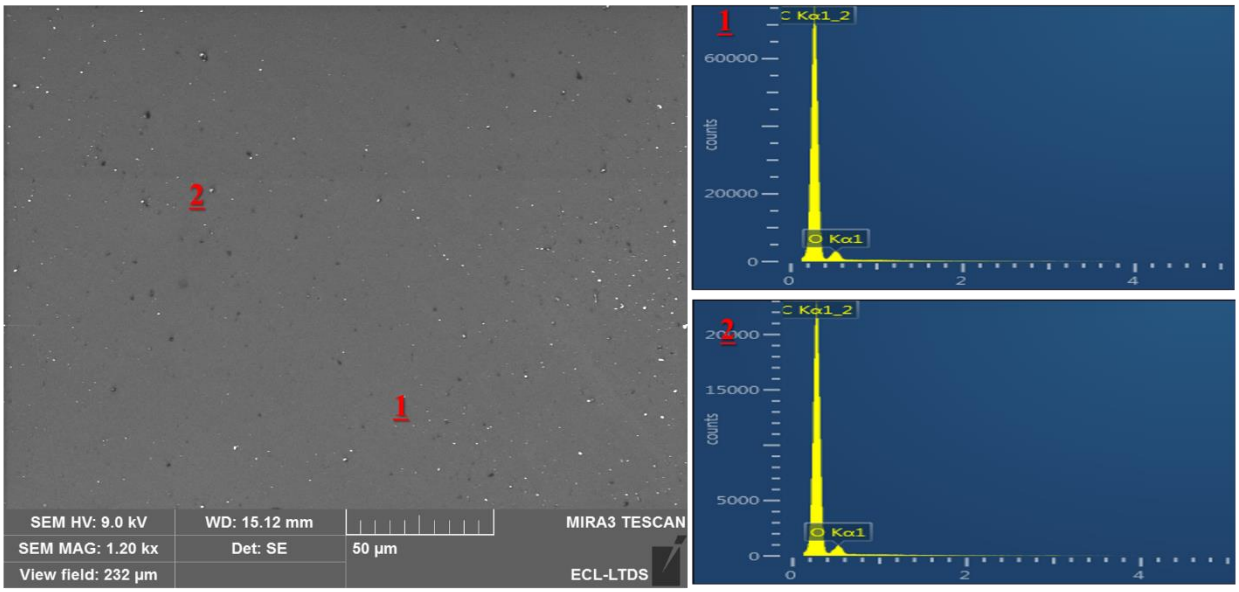

1GPa

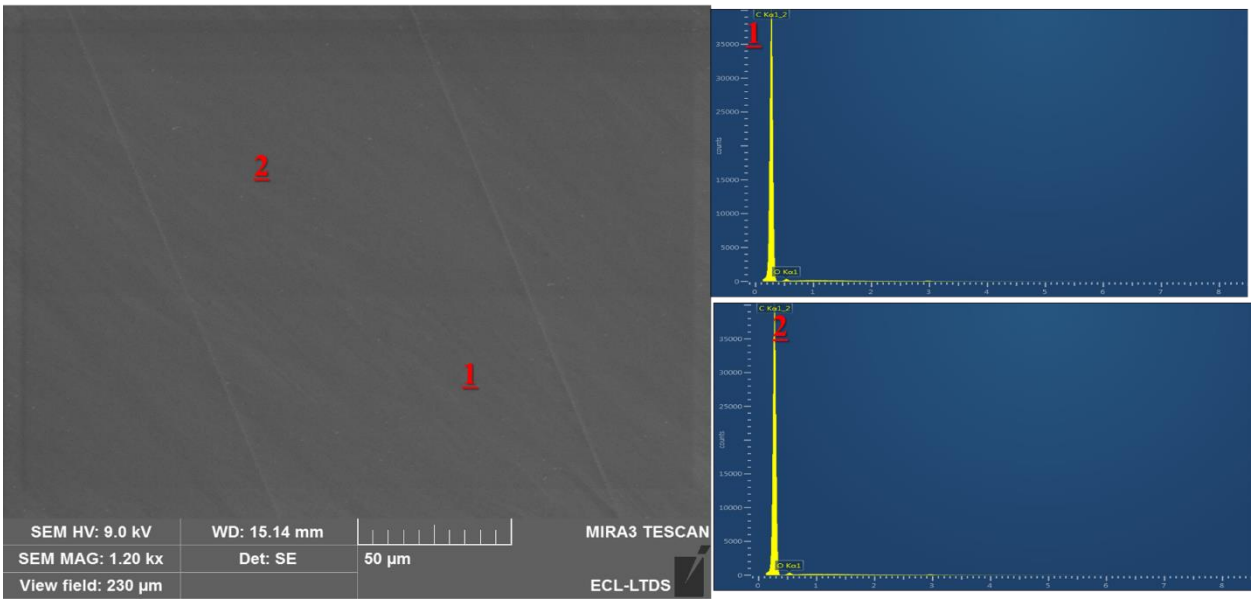

Fig. 3.6 SEM images of a-C:H coated disks for steel ring (not polished)/a-C:H disk friction test at 320MPa (a), 500MPa (b), 740MPa (c), 1GPa (d) and the corresponding EDS Point ID analysis on point 1 and 2, respectively.

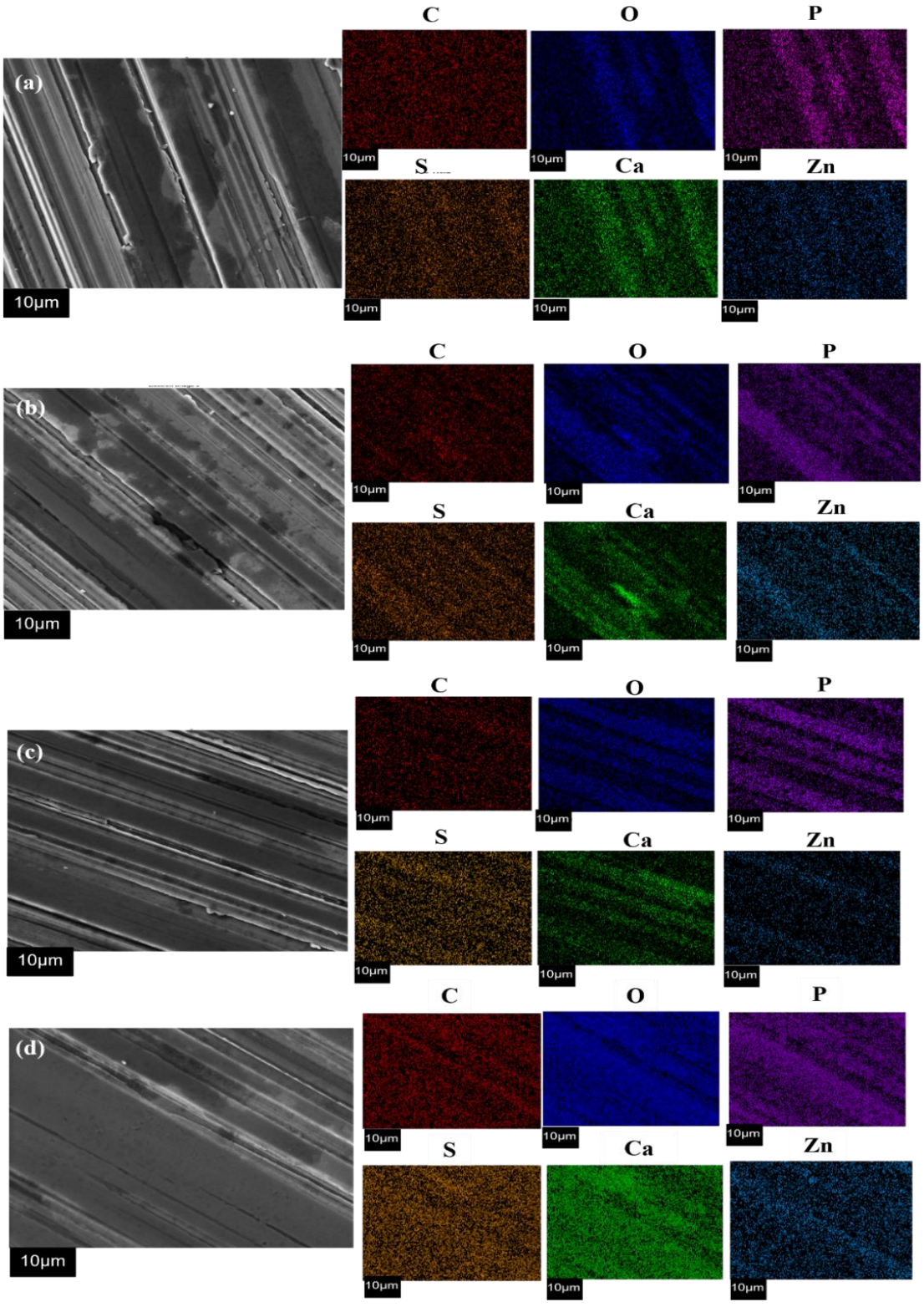

Fig. 3.7 SEM images of rings for steel ring (not polished)/a-C:H disk at 320MPa (a), 500MPa (b), 740MPa (c), 1GPa (d) and the corresponding EDS mapping results of C, O, P, S, Ca and Zn.

The observation of the steel rings' cross-section with TEM gives information on the structure and thickness of the calcium carbonate-rich tribofilms. At 320MPa, Fig. 3.8(a), the thickness of the tribofilm is in a range of 100 to 180nm due to the fact that the tribofilm was formed on a gap. This gap can either be the valley on very rough surface or an area where a piece of iron is worn from the surface during sliding tests. This will be identified in the next paragraph. Holes (marked in red circles, Fig. 3.8a) are observed in the tribofilm. This could be explained by a non-homogeneous and/or not dense tribofilm. By comparison, the tribofilm thickness at 500MPa (Fig. 3.8b) is about 110nm. The shape of the interlayer between the tribofilm and the steel substrate is more homogenous than that observed at 320MPa. At 740MPa (Fig. 3.8c), the thickness of the tribofilm is around 120nm. It is more condensed/compact compared to those observed at 320 and 500 MPa (no holes are visible anymore in the tribofilm). The shape of the interlayer between the steel substrate and the tribofilm is the most regular one. However, at 1GPa, a similar gap (Fig. 3.8d2) with 320MPa is observed. The thickness of the tribofilm varies between 120nm and 180nm (Fig. 3.8 d1 & d2). The interlayer is less regular, the tribofilm is also less compact than at 740MPa.

The difference of chemical composition on low atomic weight areas for the four steel rings was analyzed by EDS point analysis and is shown in Fig. 3.9. Low weight areas contain fewer characteristic elements (point 2 for the four steel rings). From 320MPa to 740MPa, the difference between low weight and high weight zones is less significant. At 740MPa, there is almost no difference in the amounts of elements measured on different locations. This indicates the formation of a more and more dense/compact and homogeneous tribofilm when the contact pressure increases. However, at 1GPa, the tribofilm becomes less compact again. The difference between low weight area and high weight area is observed.

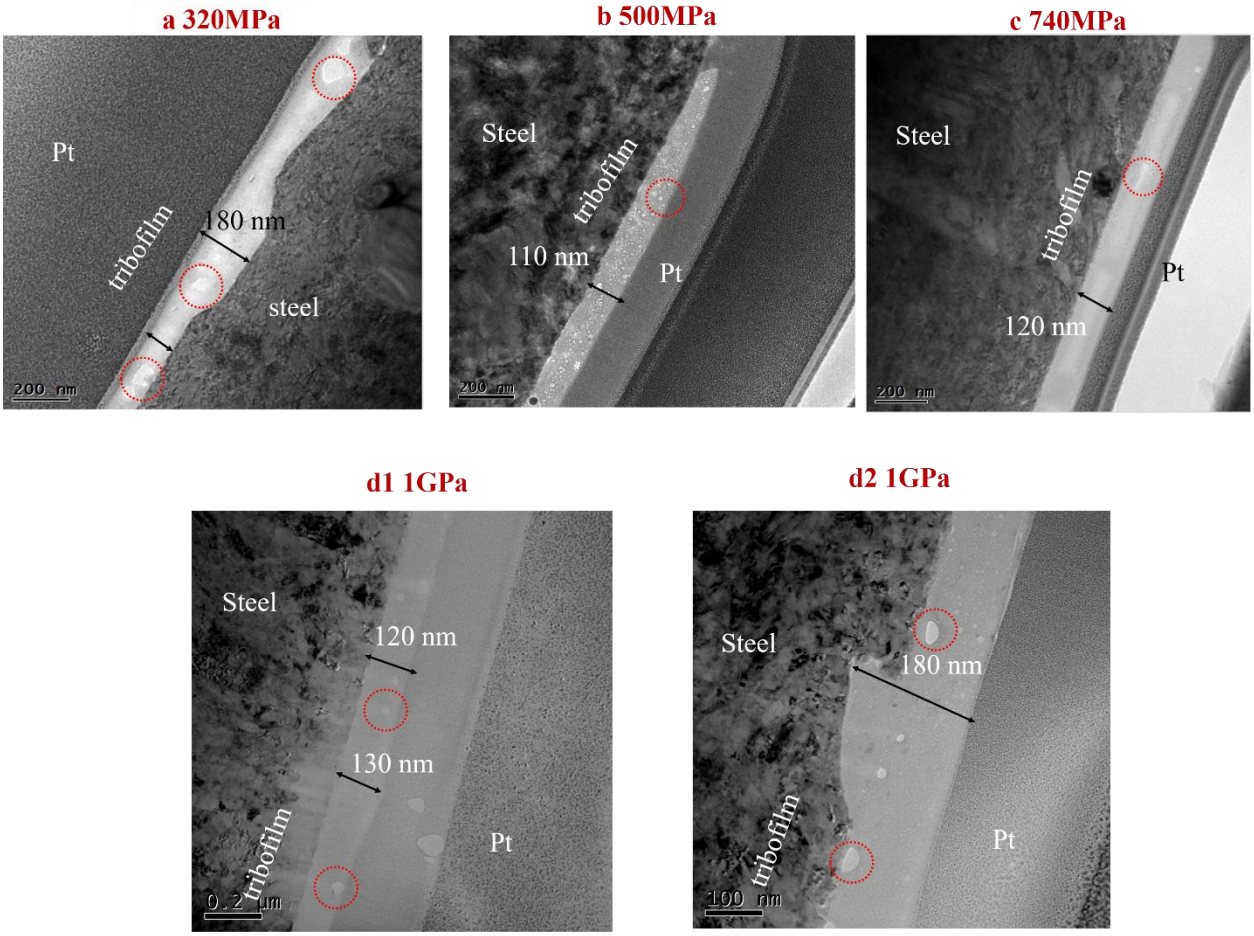

Fig. 3.8 TEM/FIB cross-section of steel rings at 320MPa (a), 500MPa (b), 740MPa (c) and 1GPa (d1, d2)

320MPa

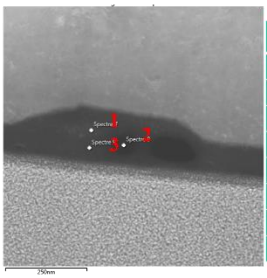

Elements	1	2	3
C	84.20	83.26	85.94
O	10.46	0.00	10.21
P	1.89	1.07	1.74
S	1.33	0.70	0.48
Ca	1.20	0.00	1.24
Fe	0.25	14.97	0.30
Zn	0.57	0.00	0.08
Total	100.00	100.00	100.00

500MPa

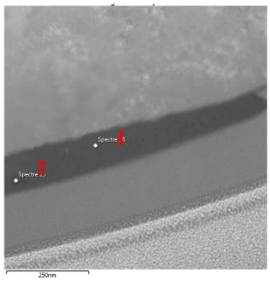

Elements	1	2
C	65.13	88.52
O	20.50	8.60
P	2.40	1.48
S	0.41	0.18
Ca	1.85	0.68
Fe	9.44	0.40
Zn	0.28	0.13
Total	100.00	100.00

740MPa

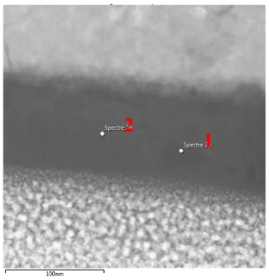

Elements	1	2
C	88.43	87.41
O	8.58	10.13
P	0.68	0.34
S	0.03	0.01
Ca	2.14	1.98
Fe	0.12	0.13
Zn	0.02	0.01
Total	100.00	100.00

1GPa

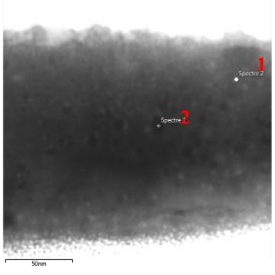

Elements	1	2
C	19.00	68.60
O	54.90	16.73
P	10.56	2.03
S	0.37	0.31
Ca	12.38	8.71
Fe	2.48	3.30
Zn	0.32	0.31
Total	100.00	100.00

Fig. 3.9 EDS point ID analysis of low and high weight zones on FIB cuts of four steel rings

EDS quantification was carried out from the four different tribofilms. Considering the fact that the tribofilm is not very homogeneous, especially at 320MPa and 1GPa, at least 3 zones were selected to ensure the accuracy. The atomic percentage of Ca, Fe and the atomic (P+S+Zn)/Ca are plotted in Fig. 3.10. The Ca quantity increases with the pressure from 320MPa to 1GPa. At the opposite, the Fe quantity dramatically decreases from 320MPa to 740MPa, then, it increases at 1GPa. The ratio of (P+S+Zn)/Ca significantly decreases until 740MPa, but at 1.0GPa, it grows again. These results indicate that the tribofilm is richer and richer in calcium when the contact pressure increase, which is also in agreement with the quantification carried out by XPS. And the content variation of Fe as the function of pressure shows that in Fig. 3.8, at 320MPa and 1GPa, the tribofilm is more possibly formed on the area where the wear occurred during the friction, rather than on the groove of very rough surface.

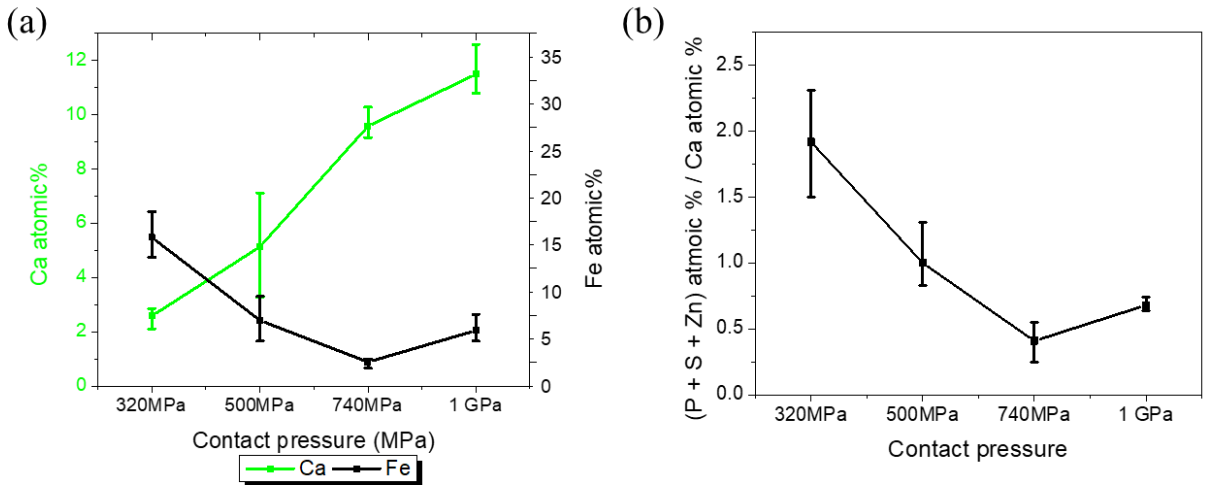

Fig. 3.10 The atomic ratio of Ca/Fe (a) and (P+S+Zn)/Ca (b) obtained by FIB-TEM/EDS

Diffraction was made from the cross-sections prepared from the steel rings. The crystal structures were determined by measuring the d-distance (measured by Gatan, GMS3) for each of the four pressures. The d-distance values are listed below. At low and medium loads (320MPa and 500MPa),

iron disulfide and vaterite (Fig. 3.11a) or aragonite (Fig. 3.11b) were found in the tribofilm. At 740MPa, iron disulfide is no more detected, and calcium carbonate is found in the form of calcite (Fig. 3.11c). To verify the calcite structure of the calcium carbonate at 740MPa, the cross-section was characterized using TITAN High Resolution HR-TEM (Fig 3.11e). The d-distance values were measured again, but more precisely thanks to the better resolution of the microscope. A good match between the experimental and theoretical values of calcite was confirmed. At 1.0GPa (Fig. 3.11d), the iron disulfide/iron oxide and calcite crystals are again found in the tribofilm. Interestingly, at 1.0GPa, it seems like that the aragonite becomes more predominant in the tribofilm comparing with 740MPa. The variation of crystal composition is consistent with the results obtained from Fig. 3.8 and Fig. 3.9. The more regular the interlayer between tribofilm and steel substrate is, the less quantity of iron related species in tribofilm.

a 320MPa

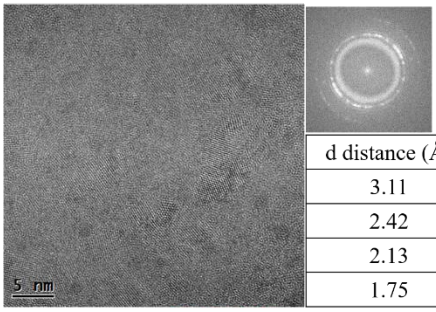

d distance (Å)	320MPa
3.11	FeS_2^*
2.42	FeS_2^*
2.13	Vaterite
1.75	Vaterite

b 500MPa

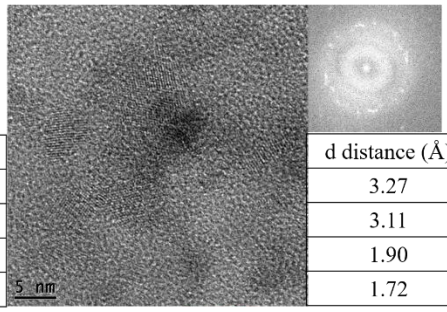

d distance (Å)	500MPa
3.27	Aragonite
3.11	FeS_2^*
1.90	Aragonite
1.72	Aragonite

c 740MPa

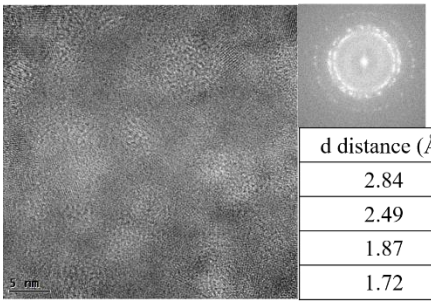

d distance (Å)	740MPa
2.84	***Calcite***
2.49	***Calcite***
1.87	***Calcite***
1.72	*Aragonite*

d 1GPa

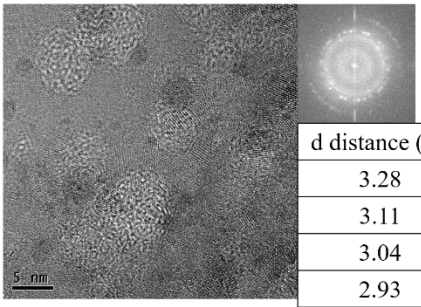

d distance (Å)	1GPa
3.28	***Aragonite***
3.11	FeS/ZnS
3.04	***Calcite***
2.93	Fe2O3
2.37	***Aragonite***
1.91	***Calcite***
1.87	***Calcite***
1.67	Fe2O3

e 740MPa (Titan)

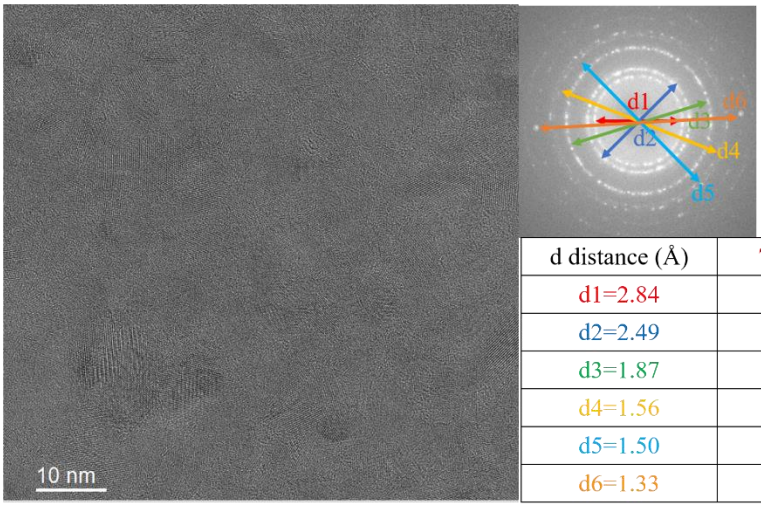

d distance (Å)	**740MPa**
d1=2.84	**Calcite**
d2=2.49	**Calcite**
d3=1.87	**Calcite**
d4=1.56	**Calcite**
d5=1.50	**Calcite**
d6=1.33	**Calcite**

Fig. 3.11 TEM diffraction mode on cross-sections and d-distance measurements at 320MPa (a), 500MPa (b), 740MPa (c), 1GPa (d) and 740MPa verified by Titan microscope (e) [6-8]

3.1.1.4 Infrared analysis

The presence of vaterite, aragonite, and calcite in the tribofilm obtained at different contact pressures was confirmed by FTIR carried out in reflection mode (Fig. 3.12). By comparing with the raw steel ring (before friction), the spectra recorded after friction tests display more significant peaks located at around 860cm^{-1} and 880cm^{-1}. The peak at 860cm^{-1} is assigned to the contribution of aragonite, while the one at 880cm^{-1} was attributed to vaterite and/or calcite [9-11]. Combining with the results obtained by TEM, it can be concluded that at 320MPa, the majority of calcium carbonate is in vaterite form together with a little of aragonite polymorph. At 500MPa, calcium carbonate is mainly in aragonite polymorph with a few vaterite/calcite. At 740MPa, the polymorph transfers significantly from aragonite to calcite. At 1GPa, the peak located at 880cm^{-1} is also more significant than the one at 860cm^{-1}. This indicates that the calcium carbonate polymorph in tribofilm is mostly composed of calcite plus a few amounts of aragonite.

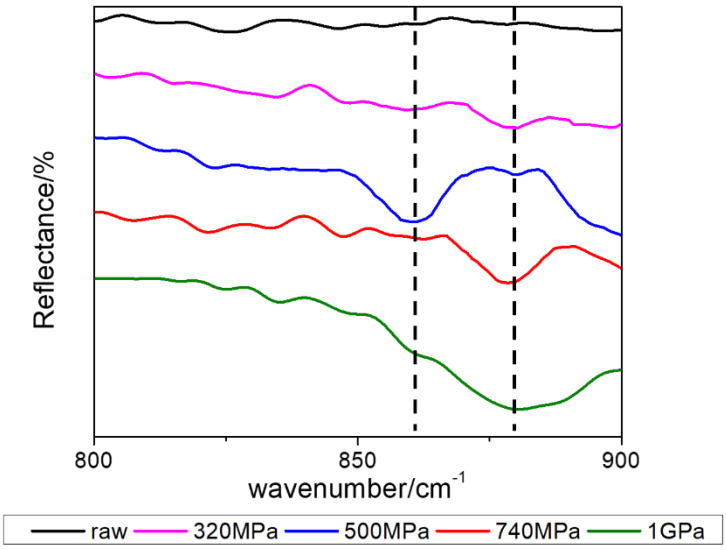

Fig. 3.12 FTIR characterization on wear tracks of steel ring at 320MPa, 500MPa, 740MPa and 1GPa

3.1.2 Effect of materials nature (steel/steel and a-C:H/a-C:H)

3.1.2.1 Tribological results

The steel/steel and a-C:H/a-C:H tribo-contacts were used to study the effect of the materials nature on the global tribological performances. The friction tests were performed at 320MPa, 500MPa and 740MPa. The friction curves are shown in Fig. 3.13. In contrary with the friction observed with the pressure increase for the steel/a-C:H mixed contact, for steel self-mated contact, the CoF increases with the contact load. For a-C:H self-mated contact, the CoF decreases at medium load, and increases again at high load. The surface roughness after friction tests were measured by interferometer (**Fig. A2**). The initial surface roughness and lubrication regime before the friction tests can be found in chapter 2 **Tab. 2.1** and **section 2.4**. The Rq values of the polished steel ring and the steel disk after the friction tests are 70 nm ± 20 nm and 20 nm ± 5 nm, respectively. The Rq values of the a-C:H ring and the a-C:H disk after the friction tests are 65 nm ± 15 nm and 15 nm ± 5 nm, respectively. The surface roughness increases after the tests for both two tribo-pairs. They remain in mixed/elasto-hydrodynamic lubrication regime after the tests.

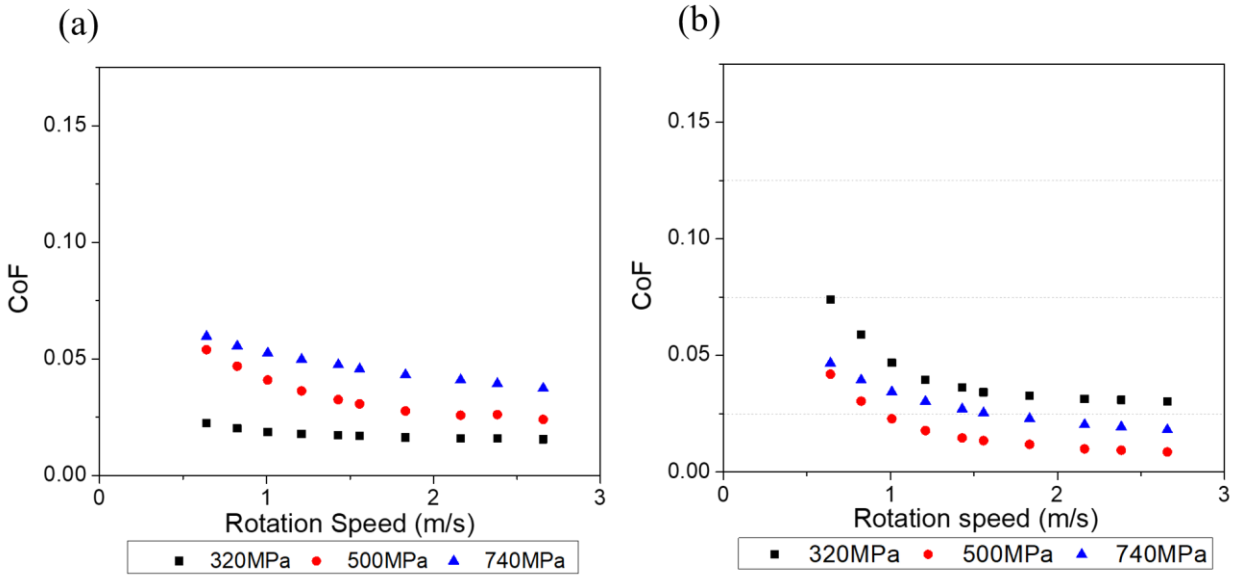

Fig. 3.13 CoF curves for steel self-mated (a) and a-C:H self-mated (b) at 320MPa, 500MPa and 740MPa.

According to the stribeck curve, it is logical to have a growth of friction as the function of pressure in this lubrication regime. Nevertheless, comparing with the friction reduction observed for the steel/a-C:H contact, it is still interesting to have a further study, especially to investigate the polymorph and allotrope structure of calcium carbonate at high contact pressure. This can be very helpful to have a deeper understanding on the friction reduction role of calcium carbonate. Therefore, the surface analyses in this section are focalized on the samples after the friction tests carried out at 740MPa.

Fig. 3.14 shows the optical images recorded on wear track after friction tests at 740MPa for steel/a-C:H mixed (a1, b1), a-C:H self-mated (a2, b2) and steel self-mated tribo-pairs (a3, b3). The absence of visible tribofilm on a-C:H surfaces (a1, a2 and b2) indicates either the presence of a super thin tribofilm, not optically visible, or that only few chemical interactions occur between a-C:H DLC and lubricants. For steel surfaces (b1, a3 and b3), the well-visible tribo-film is observed.

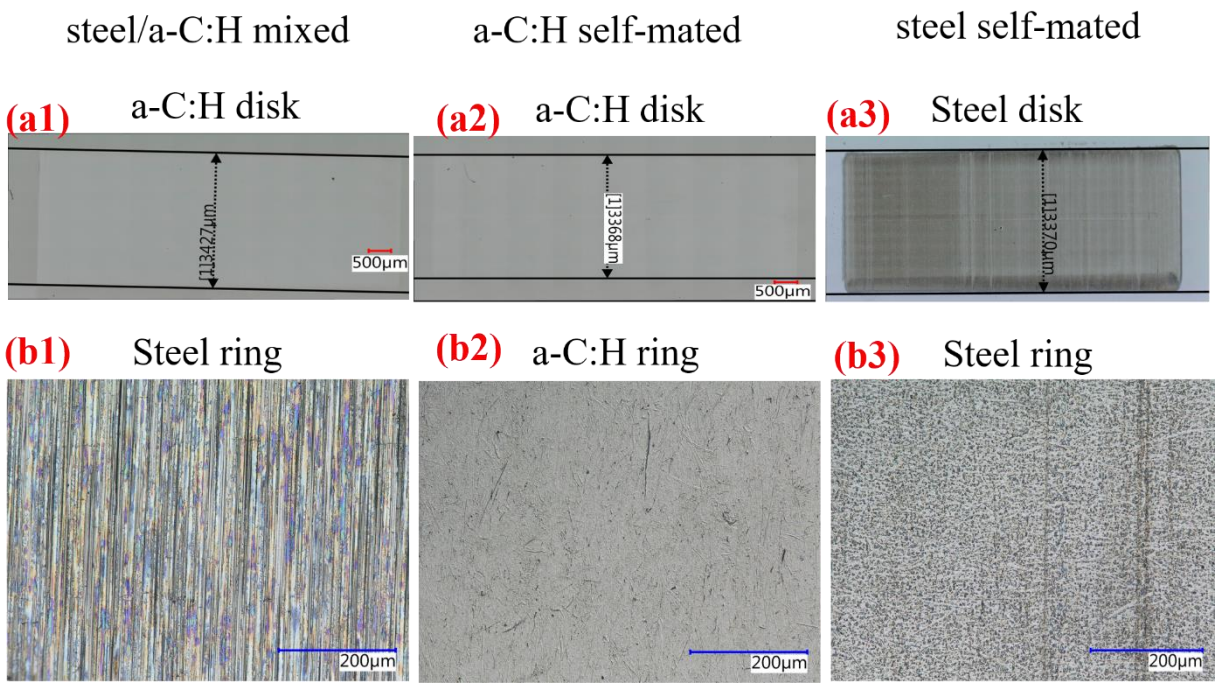

Fig. 3.14 Optical images recorded on wear tracks after friction tests at 740MPa on steel/a-C:H (a1, b1), a-C:H self-mated (a2, b2) and steel self-mated (a3, b3).

The wear after the friction tests at 740MPa on a-C:H DLC and steel disks is measured and the results are given in Fig. 3.15. The average wear depth is measured. On a-C:H disk (Fig. 14 (b), a-C:H self-mated), the wear depth is not homogenous along the wear track. A significant wear is observed in the middle of the sliding zone. The wear is not obvious on the other areas. Interestingly, the wear depth is around 0.03µm on steel disk (Fig. 3.15 (c), steel self-mated contact) even with the presence of well-visible tribofilm. This implies that the tribofilm did not completely prevent the steel disk from wear, which could possibly happen during the running-in period. For the steel ring, the wear information is hard to be measured, mainly due to the high surface roughness and more importantly, because the whole surface is in contact with the disk. It is hard to find a vertical baseline to measure the wear depth or wear volume by interferometer or profilometer. The wear can be further confirmed by FIB cut preparation, which will be introduced in the following context.

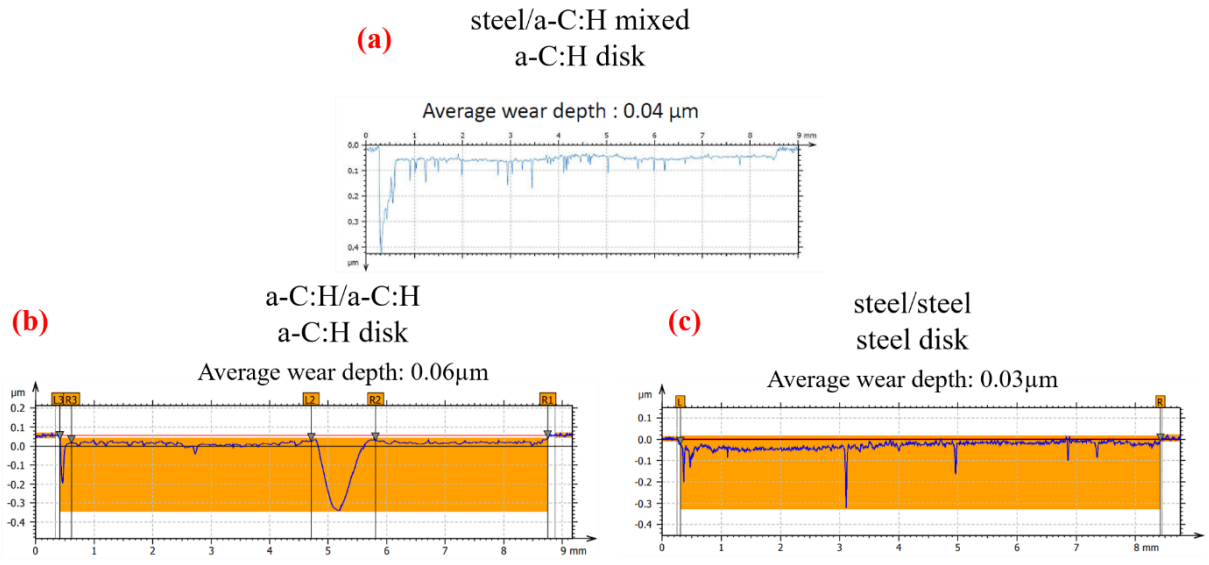

Fig. 3.15 Profiles in wear tracks after friction tests at 740MPa on a-C:H disks of steel/a-C:H (a), a-C:H/a-C:H (b) and on steel disk of steel/steel (c).

3.1.2.2 Surface chemical analysis by XPS

The XPS analysis was performed on the samples after friction tests at 740MPa. The aim of this characterization is to compare the surface composition of the different surfaces and to establish a relationship between the composition of the tribofilm and the different tribological behaviors induced by contact pressures.

The comparison of XPS quantification results is reported in Tab. 3.4 (one significant figures reserved after the decimal point). Comparing the steel/a-C:H mixed contact with a-C:H self-mated contact at 740MPa, a much lower elemental quantity can be found on a-C:H coated surfaces. This is due to the low chemical interaction between a-C:H DLC and additives. The concentration of calcium is always the most significant among the elements, thus meaning that the presence of this element is independent with the materials nature.

Tab.3.4 Atomic concentration of P, S, Ca and Zn on sliding surfaces after friction tests at 740MPa for steel/a-C:H, a-C:H/a-C:H and steel/steel

Elements	Atomic concentration (%)					
	740MPa					
	On ring			On disk		
	steel/a-C:H	a-C:H/a-C:H	steel/steel	steel/a-C:H	a-C:H/a-C:H	steel/steel
P	2.8	0.8	0.9	0.2	0.2	10.2
S	1.8	1.3	6.2	0.4	0.4	6.4
Ca	11.1	3.6	4.2	0.9	1.0	6.3
Zn	3.4	1.8	5.1	0.2	0.5	10.5

In order to verify the chemical form of calcium, XPS high resolution analysis was performed on the surfaces that are rich in calcium. The fitting strategy is the same with the one used in the previous section (contact pressure effect). Similarly, C1s and Ca2p spectra of steel ring (a) and

steel disk (b) (steel self-mated), of steel ring (c) (steel/a-C:H), of a-C:H ring (d) (a-C:H self-mated) are shown in Fig. 3.16. The contribution of carbonate (binding energy around 290 eV) is found for (b), (c) and (d). Their Ca2p3/2 peak locates at around 347.5 eV (calcium carbonate). However, (d) also displays another contribution located at 346.2eV, which is identified as calcium oxide. For (a), very few or no carbonate peak is observed. Correspondingly, the Ca2p3/2 of (b) locates at 348.2 eV, which can be assigned as calcium phosphate. The fitting results of other elements, O1s, P2p, S2p, Zn2p3/2, Fe2p3/2, can be found in **Tab. A2**.

Apparently, for both steel self-mated and a-C:H self-mated contacts, the XPS results of calcium carbonate display a difference with those of steel/a-C:H mixed contact. However, are these differences that drive the specific friction behaviors as the function of pressure? TEM/FIB analyses were performed to have a deeper understanding.

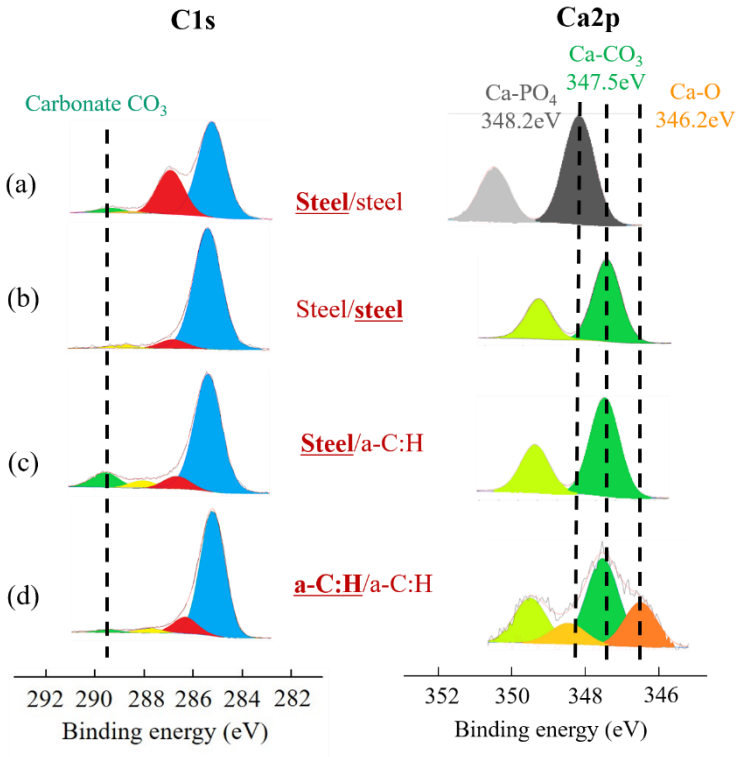

Fig. 3.16 XPS high resolution spectra of C1s and Ca2p on steel (a)/steel (b), steel (c)/a-C:H and a-C:H (d)/a-C:H

3.1.2.3 SEM & TEM observations

Based on the results of XPS high resolution spectra, TEM-FIB was carried out on the tribofilms obtained on the two surfaces of steel self-mated contact, a-C:H ring of a-C:H self-mated contact. The results were compared with steel/a-C:H mixed contact. First of all, SEM/EDS was used to localize a position rich in calcium element. Fig. 3.17 shows the secondary electron images of sliding surfaces of steel and a-C:H self-mated contacts. The mapping results of C, O, P, S, Ca and Zn are presented correspondingly. It should be noted that the presence of white spots on steel disk is due to the materials nature of M2 steel. The M2 steel disk contains tungsten whose Lα is very close with Kα of sulfur. W Lα and S Kα are the two significant peaks to identify tungsten and sulfur, respectively. The corresponding EDS justification can be found in **Fig. A3**. Therefore, in Fig. 3.17 (b), the white spots are rich in tungsten rather than sulfur (marked in red).

For steel self-mated contact, it can be seen that the shape/appearance of tribofilm on steel ring (a) is not the same with steel rings from steel/a-C:H mixed contact (Fig. 3.7 (a, b, c, d)). For steel/a-C:H mixed contact, the tribofilms on steel ring appear in the form of stripes (Fig. 3.7). By contrast, the tribofilm exhibits a dispersed pattern of small dots. The elemental distribution of Zn and S is also less obvious for steel/a-C:H mixed contact. However, it is clear that the dark area is still relatively rich in characteristic elements. On the counterpart (Fig. 3.17 (b)), calcium seems like to be present everywhere on the surface. The dark areas are rich in oxygen, phosphorous and zinc. Unfortunately, due to the existence of tungsten in M2 steel disk, the distribution of sulfur is hard to be confirmed. Nevertheless, the FIB cuts are prepared on these dark areas on both steel ring and

steel disk. From another point of view, it is for sure that the FIB cuts obtained from dark zones of steel self-mated contact are comparative with those obtained from steel/a-C:H contact.

For a-C:H self-mated contact, the FIB cut was only prepared on the ring due to the very low concentration of characteristic elements on a-C:H coated disk. On a-C:H coated disk, unlike with the results on steel, it is hard to distinguish the zone rich in tribofilm and the substrate. The results of EDS mapping can either justify the location of the tribofilm. Therefore, the FIB cut was prepared in the center of the wear track.

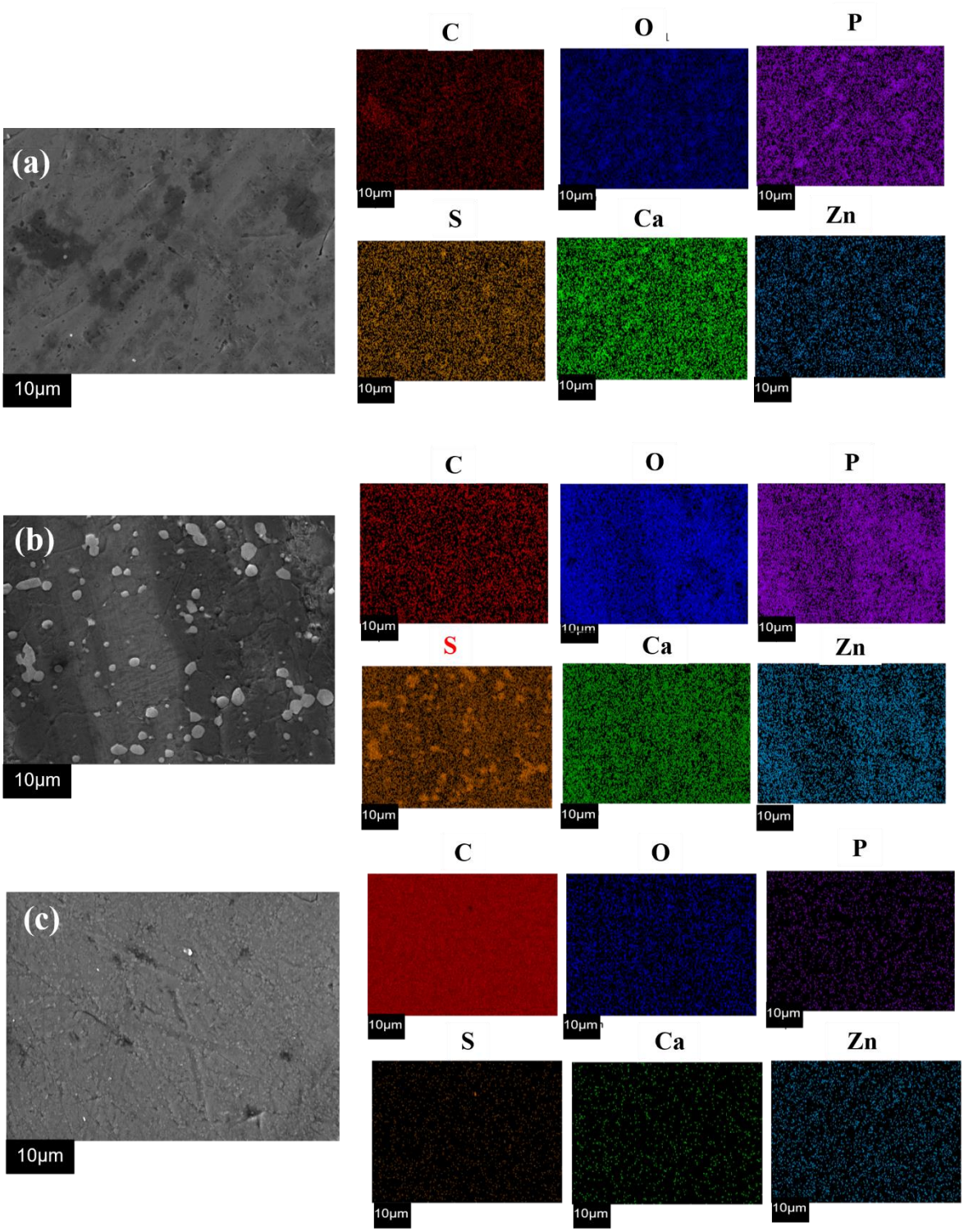

Fig. 3.17 SEM images of steel ring (a) and steel disk (b) for steel self-mated contact and a-C:H ring (c) for a-C:H self-mated contact at 740MPa and the corresponding EDS mapping results of C, O, P, S, Ca and Zn

Fig. 3.18 shows the TEM observation of FIB cuts at 740MPa of steel ring (a) and steel disk (b) from steel self-mated contact and a-C:H coated ring (c1) and (c2, higher magnification) from a-C:H self-mated contact. For steel ring in steel self-mated contact, the tribofilm is mainly formed on the hole of the surface. The EDS analysis will justify that the hole is originated from rough surface or wear during the friction. The thickness of the tribofilm varies from 30 nm (outside the hole) to 400 nm (inside the hole). On the counterpart, the much thinner tribofilm (from 20 nm to 60 nm) is observed. On both steel ring and steel disk at 740MPa, the thickness of tribofilm is not very homogeneous. This is unlike with the case of steel/a-C:H mixed contact, in which a homogeneous interlayer between the substrate and the tribofilm is observed (Fig. 3.8c). For a-C:H coated ring of a-C:H self-mated contact, the formation of the tribofilm is much less significant than the other cases. A higher resolution image of circled area is shown in Fig. 3.18 (d). It can be seen that the tribofilm is very thin and not homogeneously distributed on the surfaces. This is consistent with the XPS quantification and SEM/EDS results, in which the quantity of characteristic elements is very low and the not visible tribofilm.

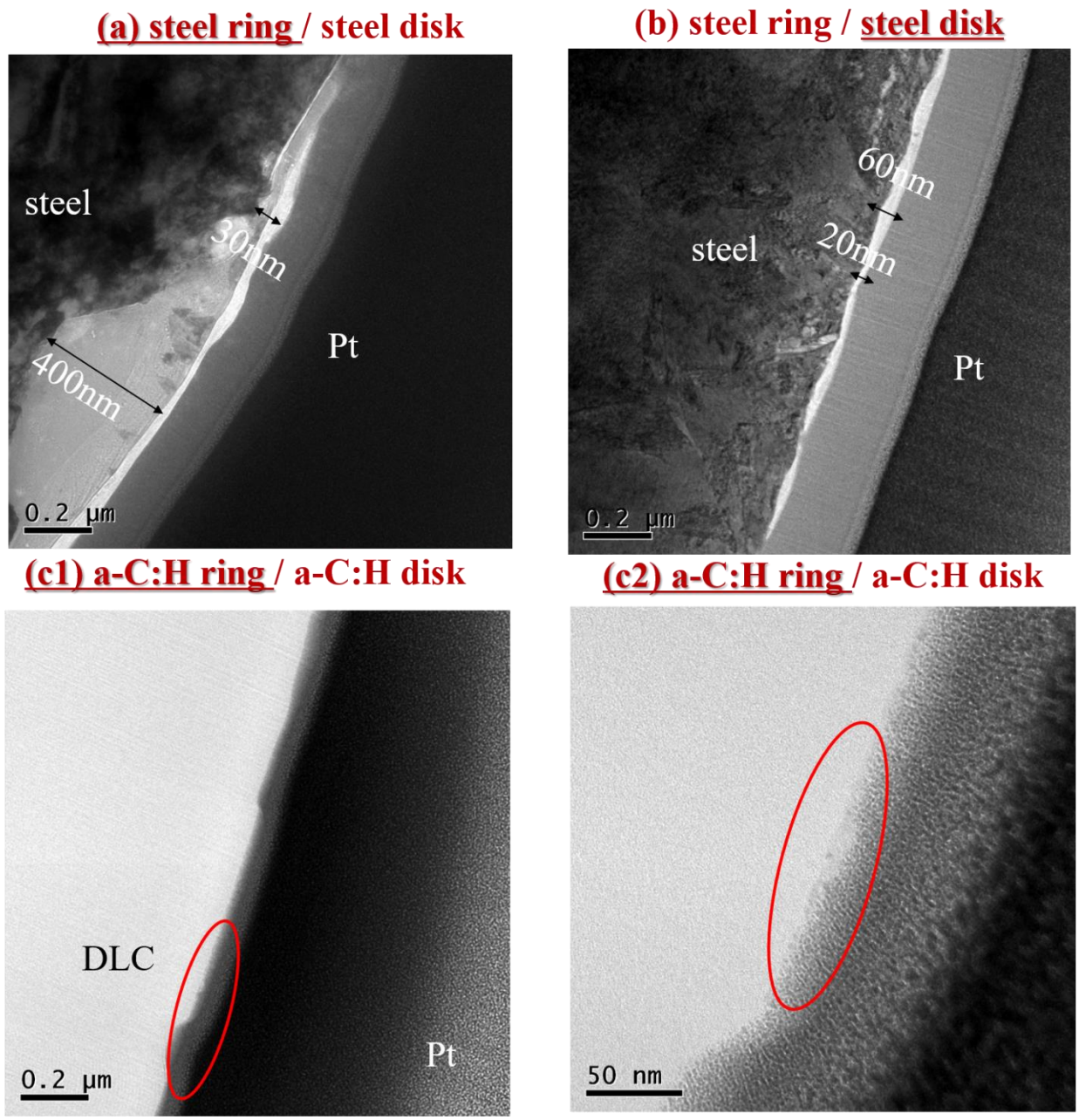

Fig. 3.18 TEM/FIB cross-section of steel ring (a) and steel disk (b) in steel self-mated contact and a-C:H ring (c1 & c2 higher magnification) in a-C:H self-mated contact.

Fig. 3.19 shows the EDS quantification analysis on the FIB cut cross section of steel ring (a) and steel disk (b, c) from steel self-mated contact and a-C:H coated ring (d) from a-C:H self-mated contact at 740MPa. In order to ensure the accuracy of the measurement and to study the distribution of the elements in the tribofilm, several zones were selected for EDS quantification. Unlike the case of steel/a-C:H mixed contact, for steel/steel contact, calcium is no longer the most significant element on both ring and disk surfaces. The large number of ZDDP-derived elements (Fig. 3.19 a, b and c) are found by EDS. This is consistent with the XPS results. On the steel ring, it seems like that the closer with the tribofilm surface (side of platinum), the more ZDDP-derived elements can be detected. Moreover, the relatively high concentration of iron element in the tribofilm indicates that the hole shown in Fig. 3.18 is mostly likely to be induced by the wear during the friction. On a-C:H coated ring, the content of all elements is very low. The content of calcium is the most significant among the characteristic elements. The concentration of phosphorous is not shown due to its very low signal in EDS spectrum. On the other hand, the super thin tribofilm on a-C:H coated ring can lead to the inaccuracy of EDS results of phosphorus, because the Pt M peak (2.048 KeV) and the phosphorous Kα peak (2.013 KeV) are very closed in EDS spectrum. In the case of a-C:H self-mated contact, the location of the tribofilm is not easy to find because the boundary between the platinum and the tribofilm is not clear. The EDS results on the a-C:H coated ring is consistent with the XPS results, in which the content of characteristic elements is much lower than on the other surfaces. This is probably due to the low chemical reactivity between the additives and the a-C:H DLC coating.

(a)

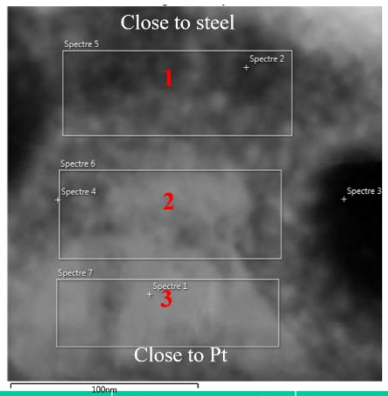

Elements	Spectrum 1	Spectrum 2	Spectrum 3
C	7.34	7.77	7.76
O	59.53	42.63	17.60
P	16.01	12.77	5.46
S	3.59	15.15	36.25
Ca	3.08	2.20	1.26
Fe	5.28	5.76	5.87
Zn	5.17	13.71	25.80
Total	100.00	100.00	100.00

(b)

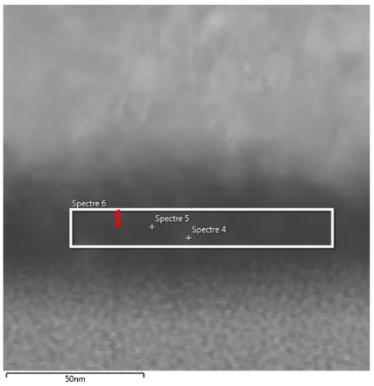

Elements	Spectrum 1
C	34.24
O	42.06
P	13.73
S	2.80
Ca	3.24
Fe	2.05
Zn	1.88
Total	100.00

(c)

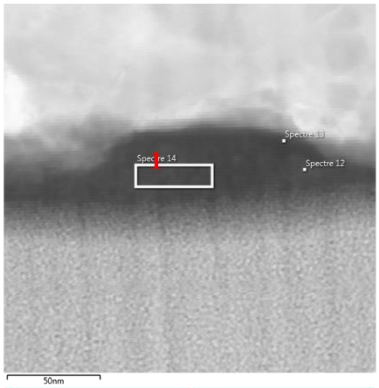

Elements	Spectrum 1
C	37.17
O	41.89
P	12.77
S	3.08
Ca	1.91
Fe	0.90
Zn	2.29
Total	100.00

(d)

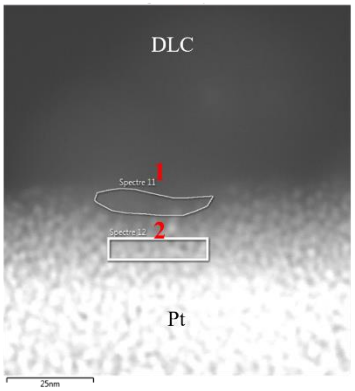

Elements	Spectrum 1	Spectrum 2
C	96.53	96.40
O	2.05	2.48
P	/	/
S	0.37	0.23
Ca	0.77	0.76
Zn	0.28	0.12
Total	100.00	100.00

Fig. 3.19 EDS analysis on the cross-section of steel ring (a) and steel disk (b) of steel self-mated contact and a-C:H DLC ring of a-C:H self-mated contact.

Fig. 3.20 shows the diffraction mode on the cross-sections of steel ring (a) and steel disk (b) of steel self-mated contact and a-C:H coated ring (c) of a-C:H self-mated contact at 740MPa. The d-distance values are listed below. On both steel ring and steel disk, the tribofilms are rich in iron sulfide and/or zinc sulfide, with probably a few amounts of iron oxide. Iron sulfide and zinc sulfide are hard to be distinguished due to their very closed d-distance values [12, 16]. Concerning the calcium carbonate, its main crystal structure is vaterite. On both the two surfaces, the calcite structure that has been observed in steel/a-C:H mixed contact is not observed for steel/steel contact. Moreover, the amount of calcium carbonate species is very low, this is consistent with XPS high resolution results, in which carbonate peak is hardly seen (Fig. 3.16a). On a-C:H coated ring, it is very difficult to obtain a clear diffraction mode image due to the very thin tribofilm. Nevertheless, the crystal plane structure can be clearly seen from TEM image, and the crystal species is confirmed to be calcite according to the d-distance measurement.

(a) steel ring / steel disk

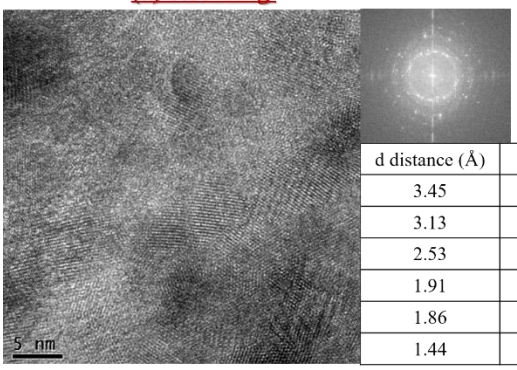

d distance (Å)	740MPa
3.45	***FeS***
3.13	***FeS/ZnS***
2.53	***Fe2O3***
1.91	***FeS/ZnS***
1.86	vaterite
1.44	***FeS***

(b) steel ring / steel disk

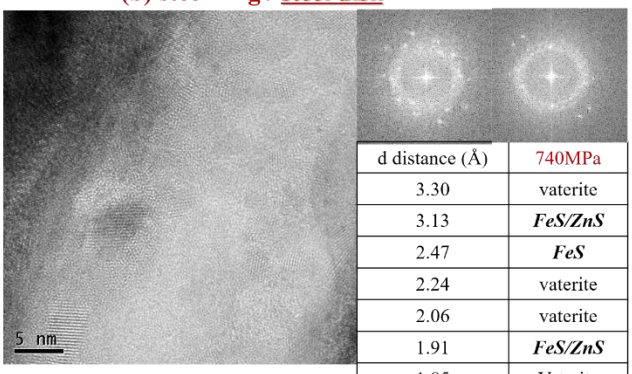

d distance (Å)	740MPa
3.30	vaterite
3.13	***FeS/ZnS***
2.47	***FeS***
2.24	vaterite
2.06	vaterite
1.91	***FeS/ZnS***
1.85	Vaterite

(c) a-C:H ring / a-C:H disk

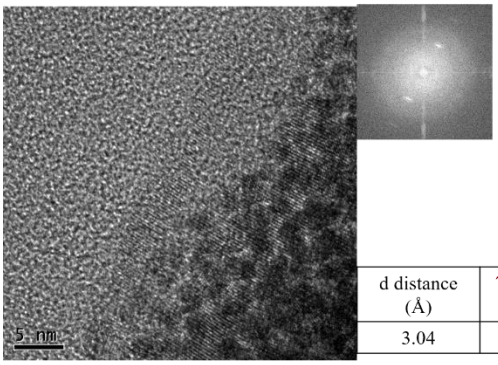

d distance (Å)	740MPa
3.04	***Calcite***

Fig. 3.20 TEM diffraction mode on cross-sections and d-distance measurements at steel ring (a) and steel disk (b) of steel self-mated contact, a-C:H DLC ring (c) of a-C:H self-mated contact at 740MPa.

3.1.2.4 Infrared analysis

In section 3.1.1.4, the crystal form of calcium carbonate in the tribofilm formed at different pressures in a steel/a-C:H mixed contact was verified by FTIR. The crystal transformation from vaterite to aragonite and calcite, which is induced by contact load, is observed thanks to the different wavenumber of these calcium carbonate polymorphs. However, for the case of steel and a-C:H self-mated contact, the allotrope of calcium carbonate is mainly either in vaterite or in calcite. The wavenumber of these two allotropes is identical, which is around 880cm^{-1}. Therefore, it is less significant and accurate to verify the existence of the calcium carbonate crystal for these two configurations.

3.1.3 TEM characterization of detergent additive in lubricant

In the study of 3.1.1 (pressure effect), the majority polymorph of calcium carbonate present in the tribofilm changes from vaterite (320MPa), to aragonite (500MPa) and finally, to calcite (740MPa & 1GPa). Its original structure in the detergent additive present in the lubricant is questionable. Therefore, the detergent particles were extracted directly from the additive (provided by TotalEnergies, France) and were observed by TEM. The extraction process is detailed in Fig. 3.21. Firstly, several drops of detergent additive were mixed with pure heptane (Chimie Plus, >99%) in glass tube in ultrasound for 10 min. Then, one small drop of liquid (detergent additive mixed with pure heptane) was deposited on the copper grid. The grid was kept in the ambient temperature and pressure until the surface was dry. After this, the grid was washed by pure heptane. The grid was put in the air to dry again. The carbon grid was also used, considering the possibility that the very

small detergent additive can probably fall in the gap on copper grid. The extraction process on carbon grid is the same. At last, the grids were ready for TEM observations.

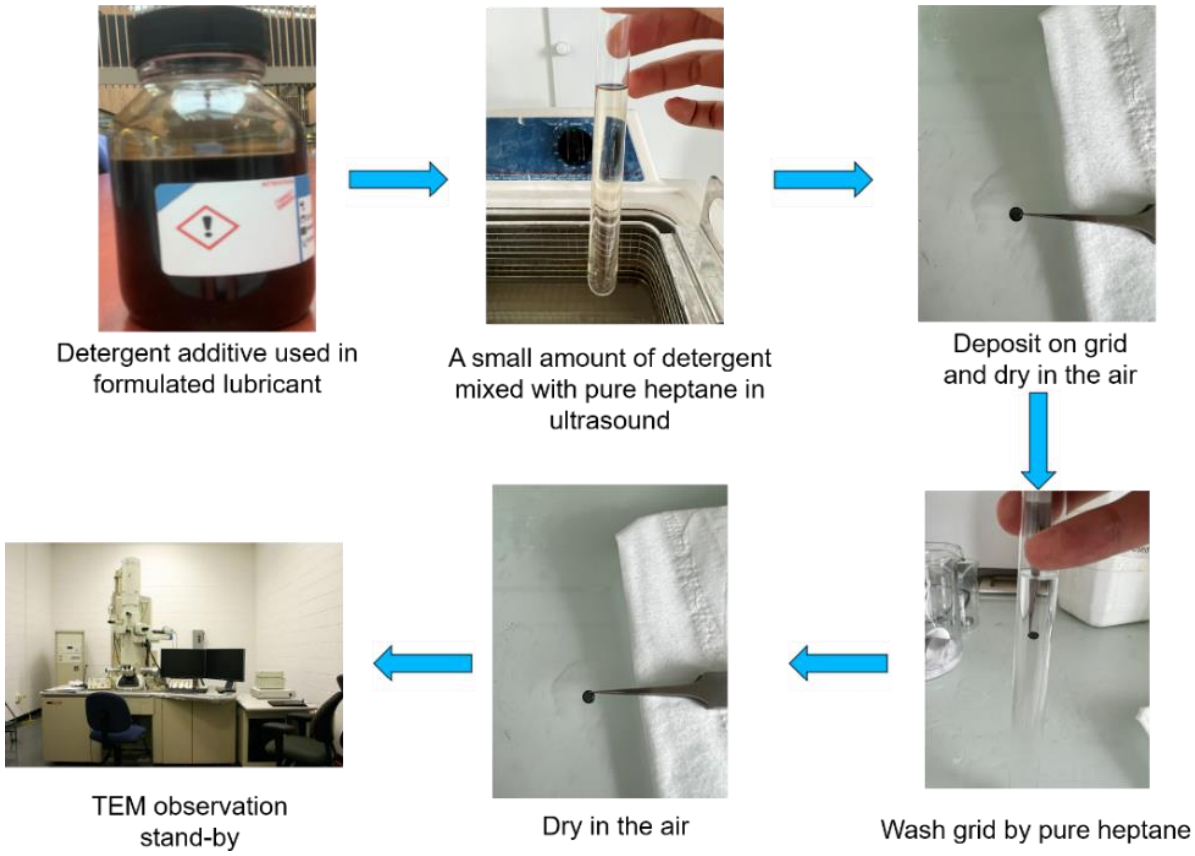

Fig. 3.21 The extraction process of detergent additive in fully formulated lubricant

The TEM observation, EDS analysis and electron diffractograms on copper grid is shown in Fig. 3.22 (a, b, c). The size of the detergent particles is in the range of 200nm to 400nm (Fig. 3.22a). The location of calcium carbonate is confirmed by EDS spectrum (Fig. 3.22 b). Diffraction mode carried out from the detergent particles clearly indicates that the structure is amorphous (Fig. 3.22c). These results would therefore mean that the detergent particles undergo significant structural modifications (crystallization) during tribological stress, these modifications being at the origin of the observed tribological properties. The nature of the crystallographic phase would also affect the tribological performance.

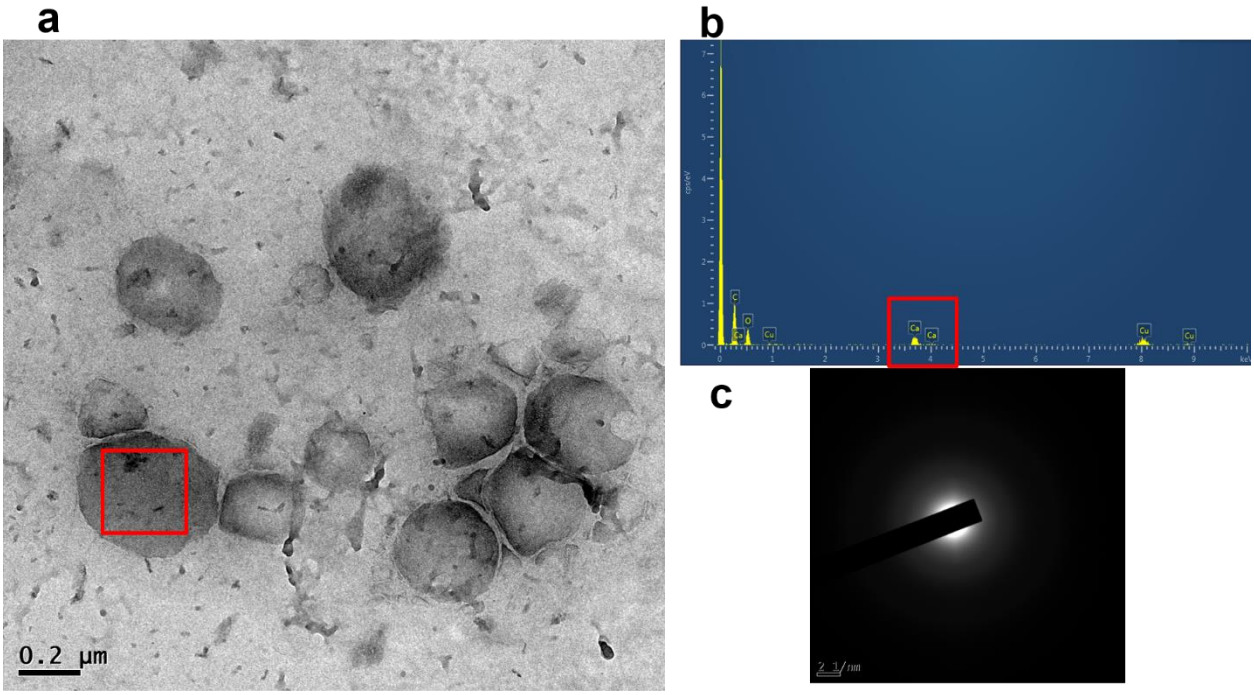

Fig. 3.22 TEM bright field image of copper detergent particles (a), the EDS pointID spectrum (b) and diffraction mode (c).

3.2 Discussion

In this chapter, the effect of contact pressure on the friction was first investigated in steel/a-C:H DLC mixed contact with a fully formulated 5W30 engine oil, in boundary/mixed lubrication regime. For this contact configuration, the coefficient of friction decreases as the function of contact pressure. A calcium carbonate-rich patchy tribofilm is found to be formed on steel. The structure of the calcium carbonate in detergent additive from engine oil is found to be amorphous. However, after the friction tests at 320MPa, 500MPa, 740MPa and 1GPa, the amorphous calcium carbonate crystallizes in vaterite, aragonite and calcite, respectively. The crystallization and crystal transformation were characterized by TEM-FIB and FTIR.

Before taking insight into the friction reduction, it would be interesting to discuss on the interaction between overbased calcium carbonate detergent and ZDDP. It should be noticed that the exact structures of the detergent additive and ZDDP antiwear additive are unknown in this study. Fortunately, the previous investigations in this field were conducted with various different structures of additives, including sulfonate, phenate and salicylate for detergent, primary and secondary alkyl chain for ZDDP. Thus, even if their detailed structures are unknown in this work, the discussion still has common worthy of attention.

Based on the results of previous researches, the anti-wear performances of ZDDP are disrupted with the presence of Ca-based detergent agents [17-26]. It should be noted that these studies were performed in steel/steel contact. This effect was not discussed on DLC coatings yet. For some early studies, the disruption was explained by the longer induction time of ZDDP induced by the overbased detergent co-additive in lubricant. In presence of overbased detergent additive, ZDDP decomposition rate is slowed down or the required decomposition temperature needs to be higher. Later on, some researches justified by XANES that the Ca^{2+} can integrate into polyphosphate chain length by replacing Zn^{2+}. The occurrence of integration was due to the fact that Ca^{2+} is a harder lewis acid than Zn^{2+}, and phosphate was also a hard lewis base. As the results, phosphates prefer to link with Ca^{2+} based on lewis acid-base theory. A common point of all these studies is that the concentration of ZDDP related elements is lower in presence of detergent. Furthermore, the presence of detergent additive could also lead to a higher CoF and reduce the anti-wear properties of ZDDP. By contrast, it was also suggested [27, 28] that neutral sulphonates act as solubilizing agents, impeding the clustering of a safeguarding antiwear film. However, the situation of overbased detergent is complex because it can also generate protective antiwear films on their own,

and the presence of ZDDP seems to enhance the efficacy of these films. Based on these studies, it seems that the combination of ZDDP and overbased detergent is not definitely a benefit to improve tribological performances.

For the study of the effect of pressure on the friction coefficient, the investigation on the tribological performances of only ZDDP or only overbased calcium carbonate detergent was not conducted to perform the comparison. However, for steel/a-C:H contact, from 320MPa to 740MPa, less wear and lower friction are observed with a decrease of the content of ZDDP derived elements. It is well-known from the literature that the ZDDP tribofilm prefers to form on steel substrate [2]. This can partially explain the fact the ZDDP tribofilm formed on DLC coatings is found to be much thinner than that on steel surface [30, 31]. An almost no visible tribofilm was observed on a-C:H DLC disks in this study. Fig. 3.8 and Fig. 3.10 show that in range of 320MPa to 740MPa, the higher the pressure, the more regular the interlayer between the steel substrate and the tribofilm is. Besides, the quantity of iron decreases. From this point of view, it seems like that the surface wear protection is assured by the well-known anti-wear property of overbased calcium detergent [31-35] by increasing the quantity of calcium carbonate and crystallization [21]. Therefore, the role of ZDDP elements is weakened between 320MPa and 740MPa, where calcium carbonate plays his role, thus improving the tribological performances. However, at 1GPa, the interlayer of tribofilm and substrate becomes less regular and the wear is observed again on steel ring (Fig. 3.8 d2). Meanwhile, the quantity of ZDDP-derived elements dramatically increases comparing with those in other contact pressures. This implies that at 1GPa, the calcium carbonate may not be sufficient to provide wear protection on ring. In other words, it cannot resist to such a high load. Therefore, ZDDP additive starts to play his part in anti-wear protection. It should be noted that the

structure of calcium carbonate remains calcite. The quantity of calcium remains the most significant element in the tribofilm.

In the study of the effect of the contact pressure on the overall tribological performances of the tribo-system, it was also found that the friction reduction as the function of pressure was tightly related to the calcium carbonate polymorph structure. The friction reduction effect of overbased detergent additive with amorphous or crystalline structures has been mentioned in references 21 and 36, but not much details were given. Meanwhile, some studies also reported that the amorphous/vaterite calcium carbonate core in detergent additive crystallized into calcite during the friction. The presence of calcite was justified by Raman spectroscopy [13], Infrared Reflection Absorption Spectroscopy by Fourier transform and Polarisation Modulation (PM-IRRAS) [37], XANES and ToF-SIMS [38]. In another study, X ray techniques justified the calcite polymorph obtained by shear strains during grinding process [39]. Based on these publications, the crystallization mechanism was basically attributed to contact pressure and shearing. On the other hand, the polymorph structure-dependent friction behavior was only reported in reference 13, but this study used crystalline calcium carbonate core rather than amorphous structure. Moreover, none of these researches present a direct observation of calcium carbonate polymorph and reveal a potential relation between CoF and polymorph structure.

In this work, the crystallization of calcium carbonate from amorph to crystal is shown. It was also demonstrated that the polymorph structure is load-dependent. These polymorph species are directly observed and characterized by TEM/FIB. However, the detailed mechanism of crystallization and crystalline transformation is extremely complex. It can be supposed that these structural changes are related to the energy dissipation induced by load, considering the order of

thermodynamic stability of the three polymorphic forms are: vaterite < aragonite < calcite. The different friction values provided by $CaCO_3$ polymorphs are also hard to explain. A more detailed explanation is expected to be given by proper numerical simulation.

In order to investigate the impact of the materials nature on the crystallization of calcium carbonate during the friction induced by the load, the friction tests were conducted using steel/steel and a-C:H/a-C:H self-mated contacts with the same lubricant in mixed/elasto-hydrodynamic lubrication regime. The tests were performed at 320MPa, 500MPa and 740MPa. For steel self-mated contact, friction increases as the function of contact load. This is in reverse with the results obtained from steel/a-C:H mixed contact. For a-C:H self-mated contact, friction decreases from 320MPa to 500MPa, and then, it increases from 500MPa to 740MPa. The surface analyses were performed on the samples after sliding tests at 740MPa to compare with steel/a-C:H mixed contact. As mentioned in section 3.1.2.1, this is to investigate if the calcite can again be obtained at high load.

For steel self-mated contact, at 740MPa, the tribofilm is found to be formed on both steel ring and steel disk. The XPS results show that the ZDDP-derived elements (P, S, Zn) become significant elements in tribofilm rather than calcium. More importantly, calcium is mainly in structure of calcium phosphate on the steel ring rather than calcium carbonate. For a-C:H self-mated contact, at 740MPa, only a few tribofilm is found to be formed on surfaces. The XPS results indicate that calcium carbonate possibly decomposed to CaO during the friction. It should be noted that, at 740MPa, the calcium element is in calcium carbonate for steel/a-C:H mixed contact. At 740MPa, TEM diffraction mode results exhibit that the calcium carbonate is mainly in vaterite structure for steel self-mated contact. While the structure of calcium carbonate is calcite for a-C:H self-mated contact, but its quantity is very low. It should be reminded that at 740MPa, the calcium is the most

significant element in the tribofilm and calcium carbonate is in calcite structure for steel/a-C:H mixed contact.

It is interesting to note that at the same contact pressure (740MPa), the polymorph of calcium carbonate is also materials-dependent. At the certain contact load, when the a-C:H DLC is employed in the tribo-pair (steel/a-C:H and a-C:H/a-C:H contacts), calcite can be found in tribofilm, although its quantity is very low for a-C:H/a-C:H contact. In the case of steel/steel contact, the polymorph of calcium carbonate is only vaterite. But the crystallization (from amorph to crystal) is still observed in steel self-mated contact. Therefore, it can be assumed that the crystallization is induced by the tribo-stressed during the friction. However, the transformation from vaterite to calcite may be ensured by the a-C:H DLC. The detailed role of a-C:H DLC to promote/catalyze the formation of calcite is unknown. No corresponding literature is found.

On the other hand, the increase of CoF as the function of pressure for steel self-mated contact can be explained by the absence of calcite in tribofilm. This partly justifies the irreplaceable role of calcite in friction reduction in steel/a-C:H configuration. The specific CoF behavior of a-C:H self-mated contact can be expected on the decomposition of calcium carbonate. We can assume that a part of calcium carbonate decomposes at high pressure (740MPa), thus resulting in a friction increase as the function of contact load.

3.3 Conclusion

This chapter investigated the mechanism of friction reduction as the function of pressure in boundary/mixed lubrication regime, for steel/a-C:H DLC-mixed contact lubricated with a commercial fully formulated 5W30 engine oil. By coupling multiple surface analysis techniques, the increase of quantity of calcium carbonate, which was originated from detergent additive, was

confirmed. The calcium carbonate not only acts to give anti-wear property but also to reduce the friction by different allotropes of crystal. The main polymorph of calcium carbonate found in the tribofilm at low contact load was vaterite, then transforming to aragonite and calcite as the contact load increases. Thanks to the 2D lamellar-like structure of aragonite and calcite, the friction control can be obtained by tuning the contact load to obtain the required polymorphic structure of calcium carbonate.

The materials impact was also investigated by employing steel and a-C:H self-mated contact, with the same lubricants in mixed/elasto-hydrodynamic lubrication regime. Steel/steel tribo-pair shows a friction increase as the function of the contact load. a-C:H self-mated tribo-pair displays a reduction and then an augmentation of the CoF. The multiple surface analyses indicate that for steel/steel configuration, calcium is no longer the most significant element in tribofilm. Calcium phosphate is found, and the allotrope of calcium carbonate remains in vaterite even at relatively high contact load. For a-C:H self-mated configuration, even though the allotrope of calcite is found in the tribofilm, it probably decomposes during the friction at high load to calcium oxide. The very different allotrope structure of calcium carbonate and tribofilm composition for steel and a-C:H self-mated contact partly justifies the essential contribution of calcium carbonate in friction reduction.

References

[1] Crobu, M., Rossi, A., & Spencer, N. D. (2012). Effect of chain-length and Countersurface on the Tribochemistry of bulk zinc Polyphosphate glasses. Tribology Letters, 48(3), 393-406. https://doi.org/10.1007/s11249-012-0034-5

[2] Spikes, H. (2004). The history and mechanisms of ZDDP. Tribology Letters, 17(3), 469–489. https://doi.org/10.1023/b:tril.0000044495.26882.b5

[3] Zhou, J. G., Thompson, J., Cutler, J., Blyth, R., Kasrai, M., Bancroft, G. M., & Yamaguchi, E. (2010). Resolving the chemical variation of phosphates in thin ZDDP Tribofilms by X-ray photoelectron spectroscopy using synchrotron radiation: Evidence for Ultraphosphates and organic phosphates. Tribology Letters, 39(1), 101-107. https://doi.org/10.1007/s11249-010-9619-z

[4] Crobu, M., Rossi, A., Mangolini, F., & Spencer, N. D. (2012). Chain-length-identification strategy in zinc polyphosphate glasses by means of XPS and ToF-SIMS. Analytical and Bioanalytical Chemistry, 403(5), 1415-1432. https://doi.org/10.1007/s00216-012-5836-7.

[5] Čoga, L., Akbari, S., Kovač, J., & Kalin, M. (2021). Differences in nano-topography and tribochemistry of ZDDP tribofilms from variations in contact configuration with steel and DLC surfaces. Friction, 10(2), 296-315. https://doi.org/10.1007/s40544-021-0491-7.

[6] Varlot, K., Kasrai, M., Martin, J. (2000). Antiwear film formation of neutral and basic ZDDP: influence of the reaction temperature and of the concentration. Tribology Letters 8, 9–16. https://doi.org/10.1023/A:1019162529554

[7] Berkani, S., Dassenoy, F., Minfray, C. (2013). Structural Changes in Tribo-Stressed Zinc Polyphosphates. Tribol Lett 51, 489–498. https://doi.org/10.1007/s11249-013-0188-9

[8] Martin, J. M., Onodera, T., Minfray, C., Dassenoy, F., & Miyamoto, A. (2012). The origin of anti-wear chemistry of ZDDP. Faraday Discussions, 156, 311. https://doi.org/10.1039/c2fd00126h

[9] Martin, J.M. (1999). Antiwear mechanisms of zinc dithiophosphate: a chemical hardness approach. Tribology Letters 6, 1–8. https://doi.org/10.1023/A:1019191019134

[10] Ye, Y., Smyth, J. R., & Boni, P. (2012). Crystal structure and thermal expansion of aragonite-group carbonates by single-crystal X-ray diffraction. American Mineralogist, 97(4), 707–712. https://doi.org/10.2138/am.2012.3923

[11] Donald, L. G. (1961). CRYSTALLOGRAPHIC TABLES FOR THE RHOMBOHEDRAL CARBONATES. THE AMERICAN MINERALOGIST, 46, November-December, 1283-1316.

[12] Gomes, A., Mendonça, M. H., da Silva Pereira, M. I., & Costa, F. M. A. (2000). Iron sulfide electrodeposits: Effect of heat treatment on composition and structure. Journal of Solid State Electrochemistry, 4(3), 168–176. https://doi.org/10.1007/s100080050015

[13] Liu, D., Zhao, G., & Wang, X. (2012). Tribological performance of lubricating greases based on calcium carbonate polymorphs under the boundary lubrication condition. Tribology Letters, 47(2), 183–194. https://doi.org/10.1007/s11249-012-9976-x

[14] Chakrabarty, D., & Mahapatra, S. (1999). Aragonite crystals with unconventional morphologies. Journal of Materials Chemistry, 9(11), 2953–2957. https://doi.org/10.1039/a905407c

[15] Ni, M. (2003). Nacre surface transformation to hydroxyapatite in a phosphate buffer solution. Biomaterials, 24(23), 4323–4331. https://doi.org/10.1016/s0142-9612(03)00236-9

[16] Suganya, S., Jothibas, M., & Muthuvel, A. (2019). Effect of temperature on different properties of ZnS nanoparticles synthesized by solid-state reaction method. Volume 5, Issue 4, 5(4), 787-790. https://doi.org/10.30799/jnst.253.19050412

[17] Wan, Y., Kasrai, M., Bancroft, G. M., & Zhang, J. (2010). Characterization of tribofilms derived from zinc dialkyldithiophosphate and salicylate detergents by X-ray absorbance near edge structure spectroscopy. Tribology International, 43(1–2), 283–288. https://doi.org/10.1016/j.triboint.2009.06.005

[18] Reyes, M., Neville, A. (2003). The effect of anti-wear additives, detergents and friction modifiers in boundary lubrication of traditional Fe-base materials. Tribology Series, 57–65. https://doi.org/10.1016/s0167-8922(03)80119-0

[19] Smith, G. C. (2000). Surface analytical science and automotive lubrication. Journal of Physics D: Applied Physics, 33(20). https://doi.org/10.1088/0022-3727/33/20/201

[20] Wan, Y., Suominen Fuller, M. L., Kasrai, M., Bancroft, G. M., Fyfe, K., Torkelson, J. R., Hu, Y. F., & Tan, K. H. (2002). Effects of detergent on the chemistry of Tribofilms from ZDDP: Studied by X-ray absorption spectroscopy and XPS. Boundary and Mixed Lubrication – Science and Applications, Proceedings of the 28th Leeds-Lyon Symposium on Tribology, 155–166. https://doi.org/10.1016/s0167-8922(02)80017-7

[21] Costello, M. T., & Urrego, R. A. (2007). Study of surface films of the ZDDP and the MODTC with crystalline and amorphous overbased calcium sulfonates by XPS. Tribology Transactions, 50(2), 217–226. https://doi.org/10.1080/10402000701271051

[22] Willermet, P. A., Dailey, D. P., Carter, R. O., Schmitz, P. J., Zhu, W., Bell, J. C., & Park, D. (1995). The composition of lubricant-derived surface layers formed in a lubricated cam/tappet contact II. Effects of adding overbased detergent and dispersant to a simple ZDTP solution. Tribology International, 28(3), 163–175. https://doi.org/10.1016/0301-679x(95)98964-f

[23] Shirahama, S., & Hirata, M. (1989). The effects of engine oil additives on Valve Train Wear. Lubrication Science, 1(4), 365–384. https://doi.org/10.1002/ls.3010010405

[24] Rounds, F. G. (1978). Additive interactions and their effect on the performance of a zinc dialkyl dithiophosphate. A S L E Transactions, 21(2), 91–101. https://doi.org/10.1080/05698197808982864

[25] Yamaguchi, E. S., Ryason, P. R., Yeh, S. W., & Hansen, T. P. (1998). Boundary Film Formation by ZnDTPs and detergents using ECR. Tribology Transactions, 41(2), 262–272. https://doi.org/10.1080/10402009808983747

[26] Kasrai, M., Vasiga, M., Suominen Fuller, M., Bancroft, G. M., & Fyfe, K. (1999). Study of the effects of ca sulfonate on antiwear film formation by X-ray absorption spectroscopy using synchrotron radiation. Journal of Synchrotron Radiation, 6(3), 719–721. https://doi.org/10.1107/s0909049598016574

[27] Zakar, A, & Vamos, E. (1986). 'Application Testing of the Additives and Additive Packages of Ready to Start Corrosion Preventative Motor and Transmission Oils', Prcc. 5th Int. Colloq. Esslingen. 'Additives for Lubricants and Operational Fluids'.

[28] Kapsa, Ph., Martin, J. M., Blanc, C., & Georges, J. M. (1981). Antiwear mechanism of ZDDP in the presence of calcium sulfonate detergent. Journal of Lubrication Technology, 103(4), 486–494. https://doi.org/10.1115/1.3251714

[29] Vengudusamy, B., Green, J. H., Lamb, G. D. & Spikes, H. A. (2013). Durability of ZDDP tribofilms formed in DLC/DLC contacts. Tribology Letters, 51(3), 469–478. https://doi.org/10.1007/s11249-013-0185-z

[30] Equey, S., Roos, S., Mueller, U., Hauert, R., Spencer, N. D., & Crockett, R. (2008). Reactions of zinc-free anti-wear additives in DLC/DLC and Steel/steel contacts. Tribology International, 41(11), 1090–1096. https://doi.org/10.1016/j.triboint.2008.03.004

[31] Najman, M., Kasrai, M., Michael Bancroft, G., & Davidson, R. (2006). Combination of ashless antiwear additives with metallic detergents: Interactions with neutral and overbased calcium sulfonates. Tribology International, 39(4), 342–355. https://doi.org/10.1016/j.triboint.2005.02.014

[32] Yin, Z., Kasrai, M., Bancroft, G. M., Fyfe, K., Colaianni, M. L., & Tan, K. H. (1997). Application of soft X-ray absorption spectroscopy in chemical characterization of antiwear films generated by ZDDP Part II: The effect of detergents and dispersants. Wear, 202(2), 192–201. https://doi.org/10.1016/s0043-1648(96)07273-0

[33] Morizur, M. F., & Teysset, O. (1992). Antiwear actions of additives in solid dispersion. Lubrication Science, 4(4), 277–299. https://doi.org/10.1002/ls.3010040405

[34] Hong, H., Riga, A.T., & Cahoon, J.M. (1993). Evaluation of overbased sulfonates as extreme pressure additives in metalworking fluids. II: Lithium and potassium overbased sulfonates. Lubrication Engineering, 51, 147-150.

[35] Mansot, J. L., Hallouis, M., & Martin, J. M. (1993). Colloidal antiwear additives 2. Tribological behaviour of colloidal additives in mild wear regime. Colloids and Surfaces A: Physicochemical and Engineering Aspects, 75, 25–31. https://doi.org/10.1016/0927-7757(93)80412-8

[36] Cao, C., Liu, G., Zhang, R., She, H., Tao, Q. (2014). Frictional characteristics of crystalline calcium sulfonate detergent in engine oil by mini-traction machine. SAE Technical Paper Series. https://doi.org/10.4271/2014-01-2789

[37] Cizaire, L., Martin, J. M., Gresser, E., Dinh, N. T., & Heau, C. (2004). Tribochemistry of overbased calcium detergents studied by Tof-Sims and other surface analyses. Tribology Letters, 17(4), 715–721. https://doi.org/10.1007/s11249-004-8078-9

[38] Palermo, T., Giasson, S., Buffeteau, T., Desbat, B., & Turlet, J. M. (1996). Study of deposit and friction films of overbased calcium sulphonate by PM-IRRAS spectroscopy. Lubrication Science, 8(2), 119–127. https://doi.org/10.1002/ls.3010080203

[39] Northwood, D. O. & Lewis D. (1968). Transformation of vaterite to calcite during grinding. THE AMERICAN MINERALOGIST, 53, November-December, 2089-2092.

[40] Blanco-Gutierrez, V., Demourgues, A., Jubera, V., & Gaudon, M. (2014). EU(III)/EU(II)-doped (ca0.7sr0.3)co3 phosphors with vaterite/calcite/aragonite forms as shock/temperature detectors. J. Mater. Chem. C, 2(46), 9969–9977. https://doi.org/10.1039/c4tc01382d

[41] Rejhon, M., Lavini, F., Khosravi, A., Shestopalov, M., Kunc, J., Tosatti, E., & Riedo, E. (2022). Relation between interfacial shear and friction force in 2d materials. Nature Nanotechnology, 17(12), 1280–1287. https://doi.org/10.1038/s41565-022-01237-7

[42] Liu, L., Zhou, M., Jin, L., Li, L., Mo, Y., Su, G., Li, X., Zhu, H., & Tian, Y. (2019). Recent advances in friction and lubrication of graphene and other 2D materials: Mechanisms and applications. Friction, 7(3), 199–216. https://doi.org/10.1007/s40544-019-0268-4

[43] Guo, Y., Zhou, X., Lee, K., Yoon, H. C., Xu, Q., & Wang, D. (2021). Recent development in friction of 2D materials: From mechanisms to applications. Nanotechnology, 32(31), 312002. https://doi.org/10.1088/1361-6528/abfa52

Chapter 4 Friction reduction in ball-on-disk configuration lubricated by fully formulated lubricant

In order to have a deeper understanding on the friction reduction mechanism proposed in chapter 3, in this chapter, additional tribological tests were performed in ball-on-disk configuration. This is not only a standard but also a simpler configuration compared to the ring-on-disk test used in chapter 3. a-C:H (ball)/steel (disk) mixed contact and a-C:H self-mated contacts were selected, steel/steel contact was used as the reference. The tribo-pairs were lubricated by the same fully formulated lubricant. After the tests, surface analyses were carried out to understand the friction mechanism.

Introduction

In the previous chapter, it has been shown that the friction reduction is tightly related to the load-dependent allotrope structure of calcium carbonate present in the tribofilm. Meanwhile, a tribo-catalytic effect induced by the a-C:H DLC coating was proposed. The aim of this chapter is to investigate if the friction reduction mechanism and the tribo-catalytic effect of the a-C:H DLC reported in chapter 3 could also be observed in ball-on-disk configuration, which is not only a standard but also a simpler and better-known one. The ball-on-disk reciprocating sliding tests were carried out with an initial maximum hertzian pressures of 0.5GPa (1.4N) and 1.0GPa (9.5N), at a temperature of 100°C, with a stroke length of 7.5mm, a frequency of 1Hz, and a test duration of 200min equivalent to 12000 cycles. At least three tests were conducted under each sliding condition to verify the repeatability. After the tests, the dimension and the depth of the wear tracks were characterized by optical microscope and interferometer. Topographical images were obtained by SEM/EDS and AFM. Surface chemical composition was analyzed by XPS. FIB cuts on tribofilms were conducted and the cross-sections were analyzed by TEM to have a deeper understanding on tribofilms' structure. The results confirmed the critical role of calcium carbonate polymorph structure in friction reduction.

4.1 Tribological results

4.1.1 Friction results

Fig. 4.1 displays the friction curves of steel/steel, a-C:H/steel and a-C:H/a-C:H at 0.5GPa (a) and 1.0GPa (b) with fully formulated oil (FFO). Only one curve is shown for each tribo-pair. The initial λ value was less than 0.1. Therefore, initially, the sliding tests were conducted in boundary lubrication regime.

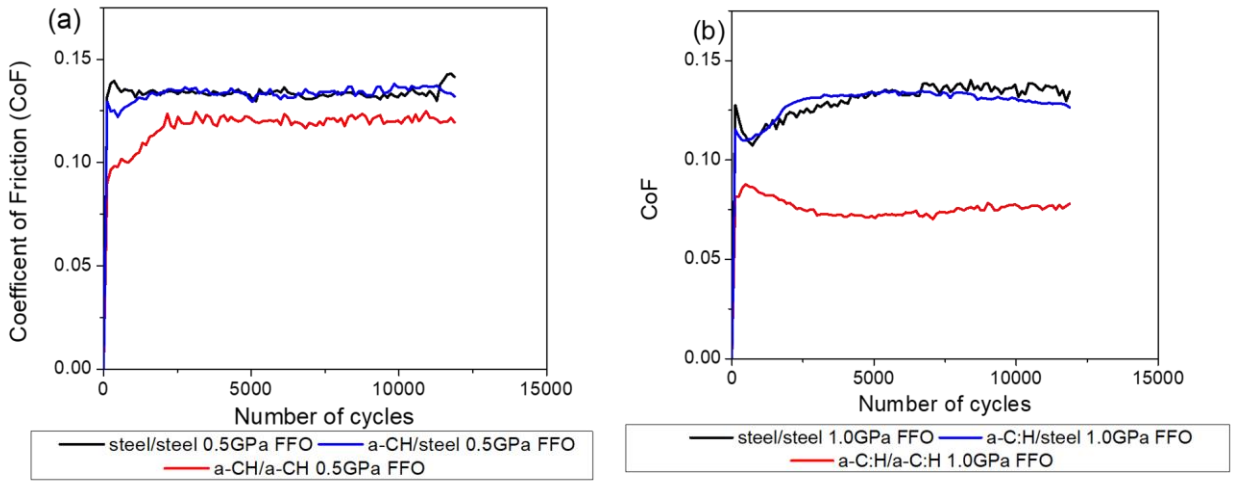

Fig. 4.1 Friction curves of steel/steel (black), a-C:H/steel (blue) and a-C:H/a-C:H (red) lubricated by fully formulated oil (FFO) at 0.5GPa (a) and 1.0GPa (b).

For steel/steel tribo-pair (black line), the steady state coefficient of friction (CoF) is obtained within 5000 cycles for the 0.5GPa and the 1.0GPa. In chapter 3, the CoF of the steel/steel in ring-on-disk configuration increased as the function of contact load. However, the effect of contact pressure on CoF is not significant for steel/steel ball-on-disk configuration The CoF is about 0.13 at both 0.5GPa and 1.0GPa.

For a-C:H/steel mixed contact (blue line), the steady state CoF is obtained within 2000 sliding cycles, which is faster than steel/steel tribo-pair. In chapter 3, the friction reduction as the function of pressure was observed for steel/a-C:H mixed contact in ring-on-disk configuration. Differently, the effect of contact pressure on the CoF is hardly seen in ball-on-disk configuration. The CoF is very similar with that of steel/steel tribo-pair.

The most interesting tribo-pair is a-C:H/a-C:H. At 0.5GPa, the friction increases at the very beginning of the test. The steady state CoF is obtained after about 3000 cycles. By contrast, at 1.0GPa, the friction decreases during the first 3000 cycles. After this, the steady state coefficient

of friction is obtained. More importantly, the friction reduction at 1.0GPa is observed. In chapter 3, the CoF of a-C:H/a-C:H decreases from 320MPa to 500MPa, and increases from 500MPa to 740MPa. Nevertheless, it should be noted that in chapter 3, for a-C:H/a-C:H tribo-pair, the CoF at 740MPa is still lower than at 320MPa (see Fig. 3.13b). The calcite was also observed by TEM (see Fig. 3.20). Therefore, to some extent, the decrease of the CoF is realized in a-C:H self-mated contact in both chapter 3 and chapter 4.

Fig. 4.2 shows the steady state CoF for three tribo-pairs at 0.5GPa and 1.0GPa.

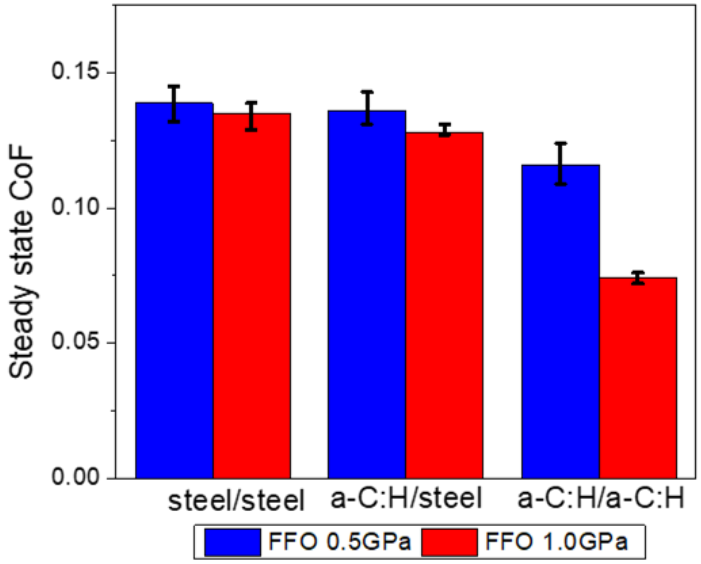

Fig. 4.2 Steady state CoF for steel/steel, a-C:H/steel and a-C:H/a-C:H at 0.5GPa and 1.0GPa

As what has been discussed previously, the significant impact of pressure on CoF is not seen for steel/steel and a-C:H/steel contacts. The steady state CoF for these two contacts is in the range of 0.13 to 0.14 at both 0.5GPa and 1.0GPa.

For a-C:H self-mated contact, the steady state CoF at 0.5GPa is around 0.12. However, the steady state CoF decreases to around 0.07 at 1.0GPa. The CoF decreases for almost 40%. Considering that the designed tests are conducted in boundary lubrication regime, the friction reduction

observed with the fully formulated oil is expected to be related with the surface chemical composition.

4.1.2 Wear results

4.1.2.1 Optical images of steel/steel

Fig. 4.3 displays the optical images of the wear tracks of steel/steel contact at 0.5GPa (a1, a2) and 1.0GPa (b1, b2).

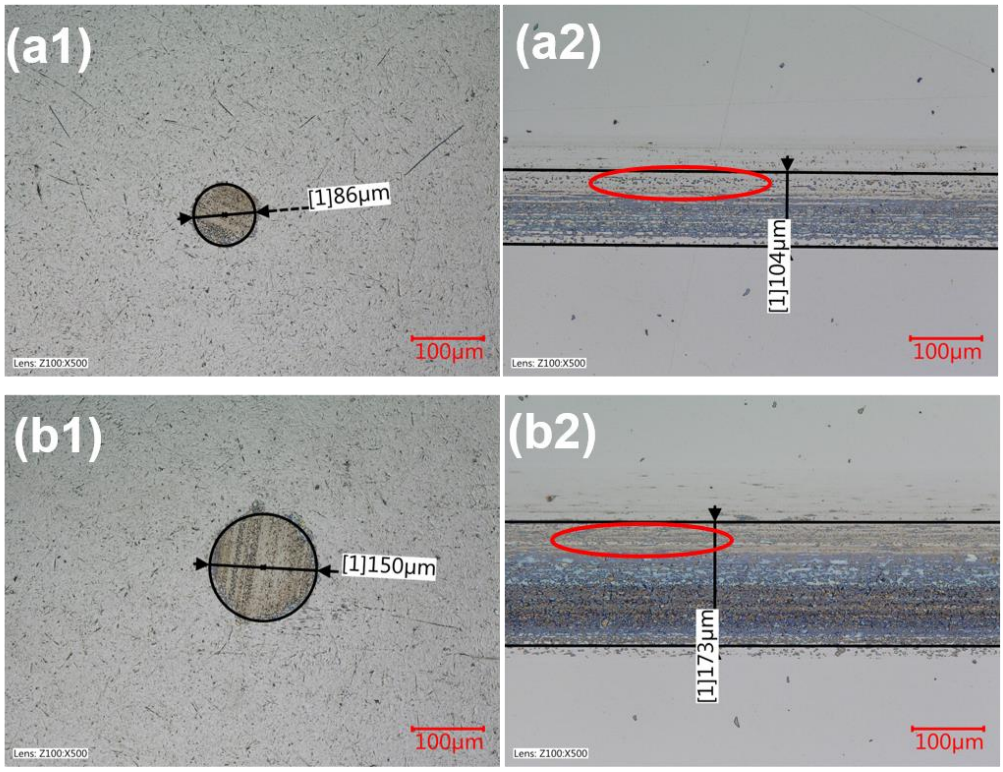

Fig. 4.3 The measurements of size of the wear track of steel/steel contact at 0.5GPa (a1, a2) and 1.0GPa (b1, b2) under optical microscope.

The tribofilms are well-visible on ball and disk. Based on the Hertz theory, the predicted size of the wear track is 70 µm and 132 µm at 0.5GPa and 1.0GPa, respectively. At both 0.5GPa and 1.0GPa, the size of the wear track is slightly higher than the hertzian values, especially on steel disks (a2, b2). At the border of the tribofilm on steel disk, the tribofilm is less continuous and less

compact than that in the center of the wear track (marked in red circle). Comparing with the contact pressure of 0.5GPa (a2), the tribofilm on steel disk of 1.0GPa (b2) exhibits a denser surface morphology and a darker color.

4.1.2.2 Optical images of a-C:H/steel

Fig. 4.4 shows the optical images of the wear tracks on steel disks of a-C:H/steel contact at 0.5GPa (a) and 1.0GPa (b).

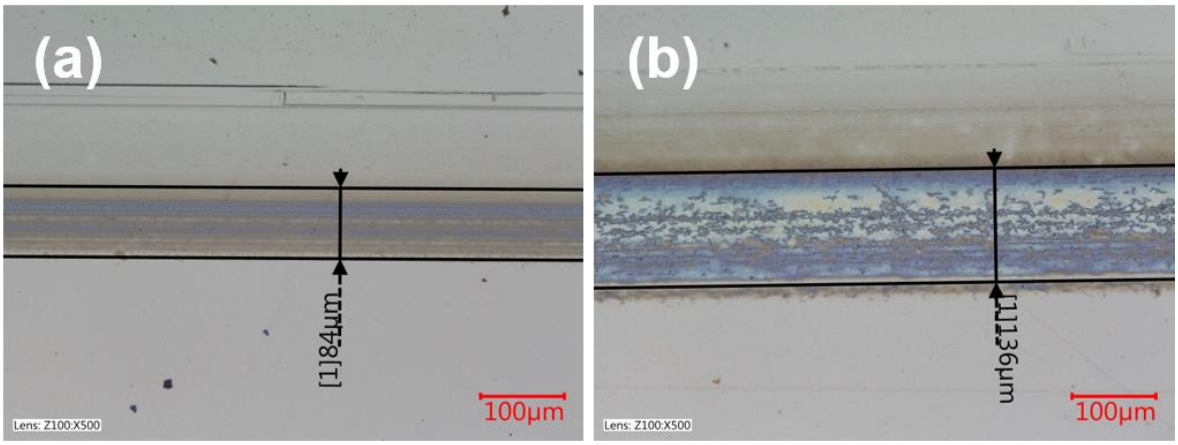

Fig. 4.4 The measurements of size of the wear track on steel disks of a-C:H/steel contact at 0.5GPa (a) and 1.0GPa (b) under optical microscope.

For a-C:H/steel contact, the wear scar on a-C:H balls is not even distinguishable from the surface where no contact occurs during the sliding tests. The size of the wear track is smaller than the steel/steel contact under the same contact pressure. The size is very closed to the predicted values based on the Hertz theory. Similarly, at 1.0GPa, the tribofilm shows a darker color and a denser surface morphology than at 0.5GPa.

4.1.2.3 Optical images of a-C:H/a-C:H

Fig. 4.5 shows the optical images of the wear tracks on steel disks of a-C:H/a-C:H contact at 0.5GPa (a) and 1.0GPa (b).

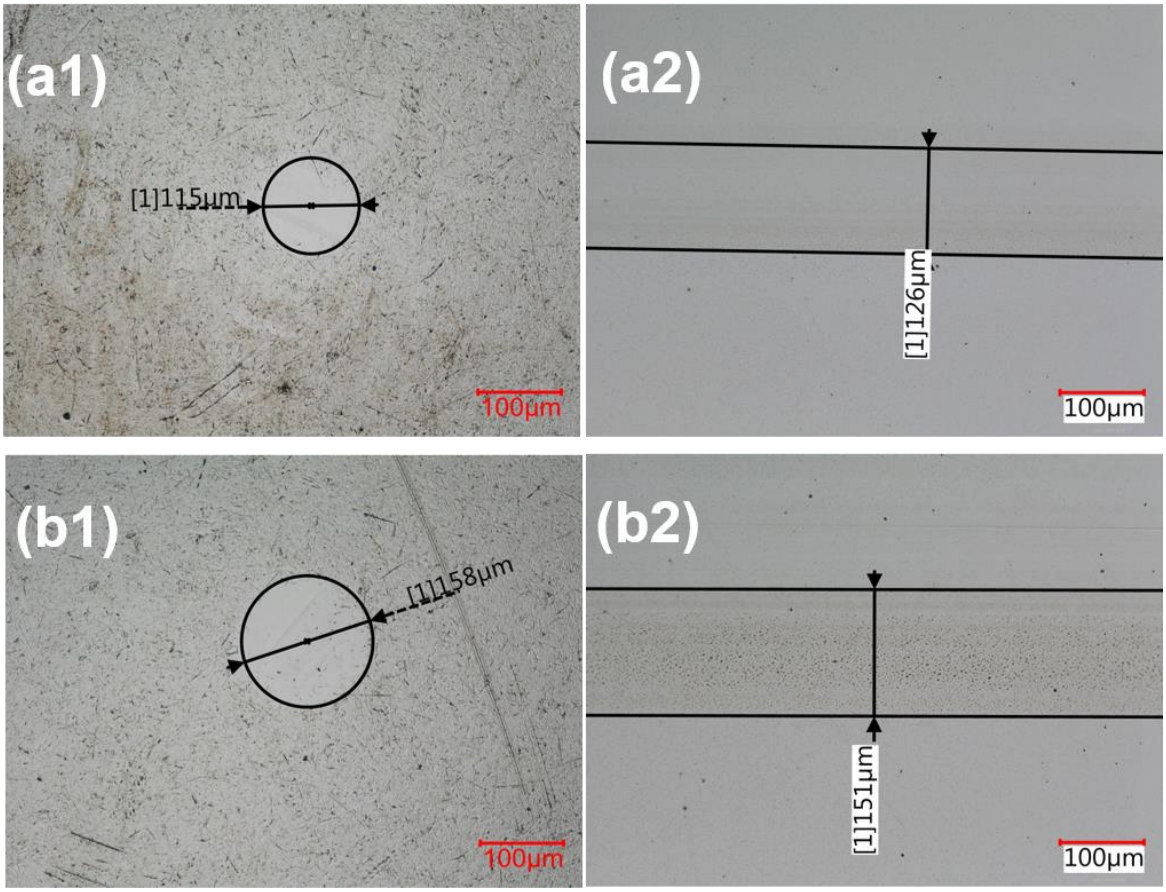

Fig. 4.5 The measurements of size of the wear track of a-C:H/a-C:H contact at 0.5GPa (a1, a2) and 1.0GPa (b1, b2) under optical microscope.

For a-C:H self-mated contact where the pressure effect in friction reduction was observed, a moderate wear is assumed by the larger wear diameter than hertzian values. Under optical microscope, it is difficult to say that a tribofilm is formed onto the surface of a-C:H coated ball. By contrast, in the wear track on a-C:H coated disks, it seems that at 1.0GPa, the scar contains some larger particles than at 0.5GPa. Unfortunately, this is not evident under optical microscope. More surface analyses were conducted and the results will be introduced in the following context.

4.1.2.4 Wear depth measurement (a-C:H/a-C:H)

The wear depth measured by interferometer on the a-C:H coated ball of a-C:H self-mated contact is shown in Fig. 4.6. In terms of the steel/steel, a-C:H/steel tribo-pairs and a-C:H coated disk from a-C:H self-mated contact, the wear diameter is very close to the hertzian predicted value thanks to the formation of the tribofilm. The wear depth is not easy to be precisely measured with the formation of these tribofilms on the surfaces.

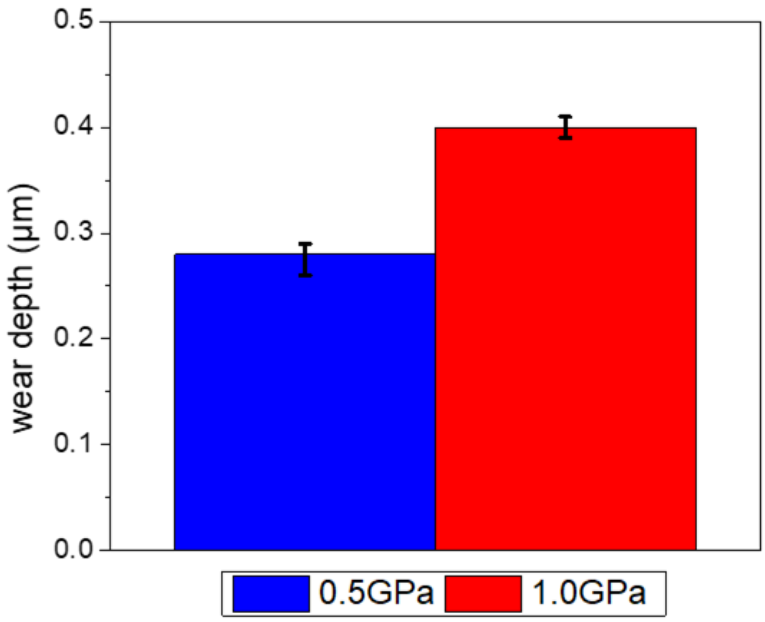

Fig. 4.6 Wear depth measured by interferometer on a-C:H coated ball from a-C:H self-mated contact at 0.5GPa and 1.0GPa.

The wear depth on a-C:H coated ball from a-C:H self-mated contact increases from 0.25 µm – 0.3 µm at 0.5GPa to around 0.4 µm at 1.0GPa. This is consistent with the increase of the wear diameter on a-C:H coated ball (see Fig. 4.5 a1, b1).

4.1.3 Contact pressure and lubrication regime verification

As shown in the optical images, the size of the wear scars is relatively larger than the size given by the hertzian theory. Therefore, the verification of real contact pressure after test can justify that

the friction reduction is not due to the pressure reduction due to the larger wear size. Besides, the surface roughness after tests is also measured to confirm the lubrication regime. These steps are particularly critical for the a-C:H self-mated contact to investigate the factors that drive the friction reduction as the function of pressure with the formulated lubricant.

The real contact pressures are given by:

$$Pcalcul. = \frac{F}{\pi a^2}$$

in which ***F*** represents the contact Force (N), ***a*** represents the contact radius (m). Tab. 4.1 presents the calculated contact pressure after the tests. It can be seen that the real contact pressure is lower than the initial values due to the larger real contact area. Fortunately, for each tribo-pair (particularly a-C:H self-mated, marked in red), the contact pressure indeed has a growth tendency. This means that the friction reduction observed for the a-C:H self-mated contact with the fully formulated oil is not driven by the decrease of the real contact pressure.

Tab. 4.1 Calculated real contact pressures after friction tests

	Steel/steel		a-C:H/a-C:H		a-C:H/steel	
Initial contact pressure (P_{max}, GPa)	0.5	1.0	0.5	1.0	0.5	1.0
Real contact pressure (GPa)	0.31	0.75	0.17	0.67	0.32	0.9

The after-test surface root mean square roughness is measured by interferometry and the values are listed in Tab. 4.2. Due to the formation of the tribofilm and/or the wear on the surfaces, the roughness is relatively higher than the initial values. For the a-C:H/steel configuration, the

roughness is not measured on the a-C:H coated ball, due to the fact that the wear scar is hardly seen under interferometry.

Tab. 4.2 The root mean square values of the surface roughness after the friction tests

Sq (nm)		steel/steel		a-C:H/a-C:H		a-C:H/steel	
		ball	disk	ball	disk	ball	disk
Formulated oil	0.5GPa	36±10	80±20	70±15	80±15	/	60±10
	1.0GPa	82±20	75±15	75±10	110±20	/	70±15

The lubrication regime is verified by using the method introduced in section 2.4. Due to the very high surface roughness after the friction tests, the lubrication regime remains in boundary. Therefore, it would be interesting to perform further surface analysis in order to investigate the factor that drives the friction reduction in a-C:H self-mated contact with the formulated oil.

4.2 Surface analysis

4.2.1 Topography (SEM + AFM)

In chapter 3, a patchy tribofilm was obtained on steel rings (polished + not polished) after the friction tests carried out with the formulated lubricant. The topography characterizations showed that the tribofilm is more spread out when the contact load increases. In this session, the SEM and AFM analyses were performed to investigate the topographical variation of the surfaces as the function of pressure. Moreover, considering that the basic elements in the tribofilm are already known from the chapter 3, together with the XPS analysis of the lubricant (C, O, P, S, Ca, Zn), EDS analysis was not performed on the surface to distinguish the tribofilm from the substrate.

4.2.1.1 Steel/steel

The secondary electron mode SEM images on the surfaces from the steel/steel contact for the initial contact pressure of 0.5GPa and 1.0GPa are shown in Fig. 4.7. The low and the high magnification were used for each sample. The white spots on the surface of the steel disks (b1, b2, d1, d2) have been explained in chapter 3, they are rich in W (Fig. **A3**).

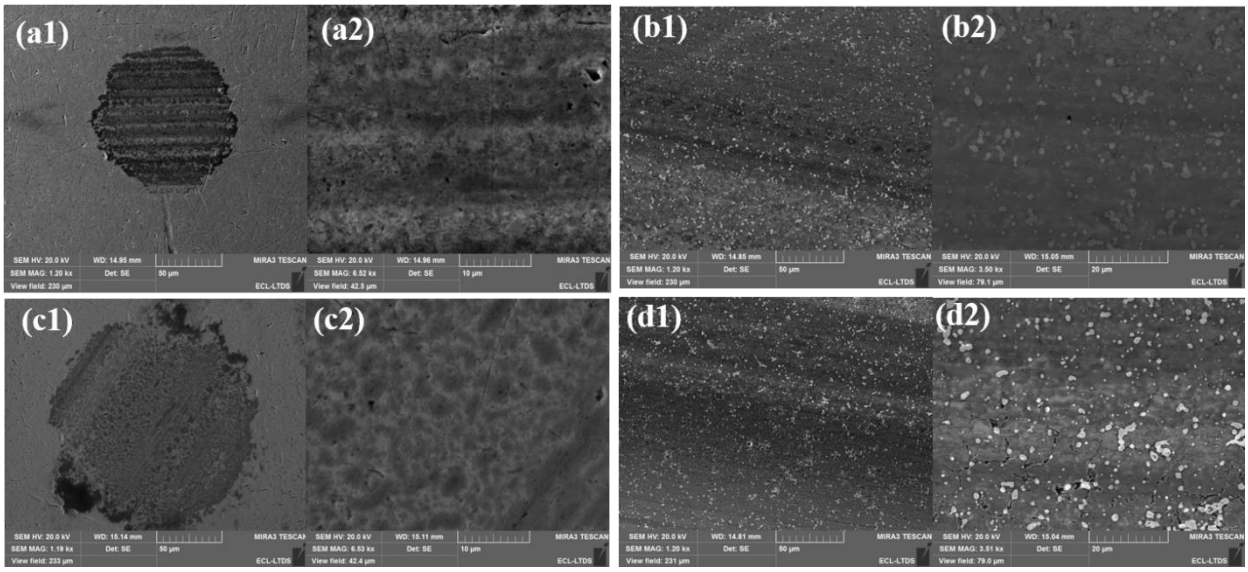

Fig. 4.7 SEM images in secondary electron mode for the steel/steel contact at 0.5GPa on the ball (a1, a2) and the disk (b1, b2), at 1.0GPa on the ball (c1, c2) and the disk (d1, d2). 1# represents low magnification, 2# represents high magnification.

Unlike the SEM results in chapter 3, the tribofilm formed for ball-on-disk configurations is more aggregated rather than patchy. With the low magnification images, the position of the tribofilm can be easily confirmed (relatively dark areas). The difference on topography between low and high initial contact pressure is not easy to be concluded for steel/steel contact. The darker and the denser surface morphology obtained at 1.0 GPa on the steel disk (Fig. 4.3 b2) is not evident in the SEM images.

The AFM images on the surfaces of the steel/steel contact is shown in Fig. 4.8.

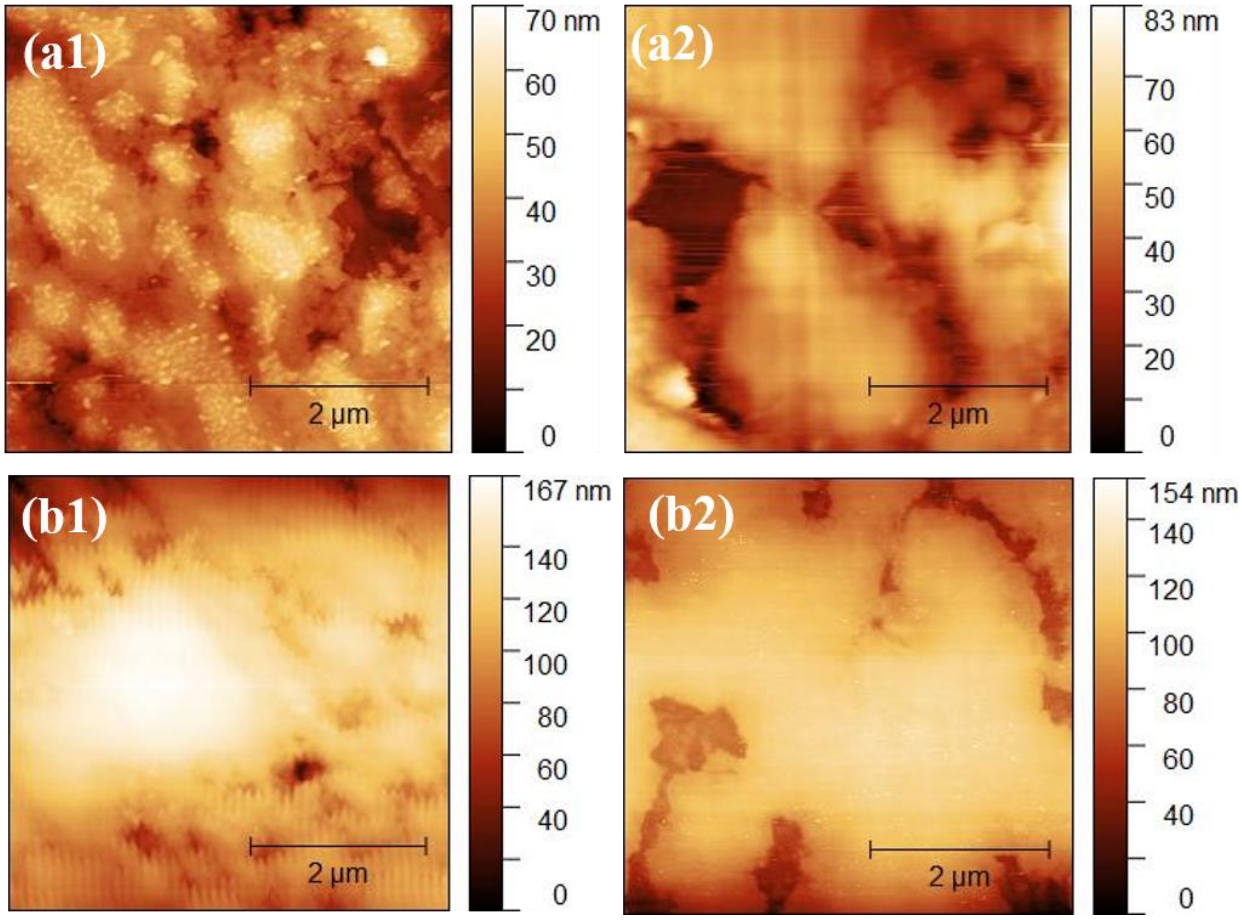

Fig. 4.8 AFM images (5µm * 5µm) on the surfaces from the steel/steel contact at 0.5GPa on ball (a1) and disk (a2), at 1.0GPa on ball (b1) and disk (b2).

For steel/steel contact, it seems that a thicker tribofilm is formed on the ball and the disk at 1.0GPa (b1, b2). The thickness of the tribofilm increases from around 75nm at 0.5GPa to around 160nm at 1.0GPa. Furthermore, the morphology of the tribofilm at 1.0GPa is smoother and more uniform (the color distribution on surfaces is more uniform). By SEM images, it is hard to tell if the tribofilm is more compact at high load. However, with AFM, it seems like that the relatively separated “isles” on surfaces are connected, and the larger “islands” are formed. Nevertheless, the morphology variations induced by the contact load does not induce different friction behaviors.

4.2.1.2 a-C:H/steel

The secondary electron mode SEM images of steel disks from a-C:H/steel contact at 0.5GPa and 1.0GPa are shown in Fig. 4.9 (a1, a2) and (b1, b2), respectively. The SEM characterization was not carried out on the a-C:H ball due to the wear track on it was not visible (see section 4.1.2.2).

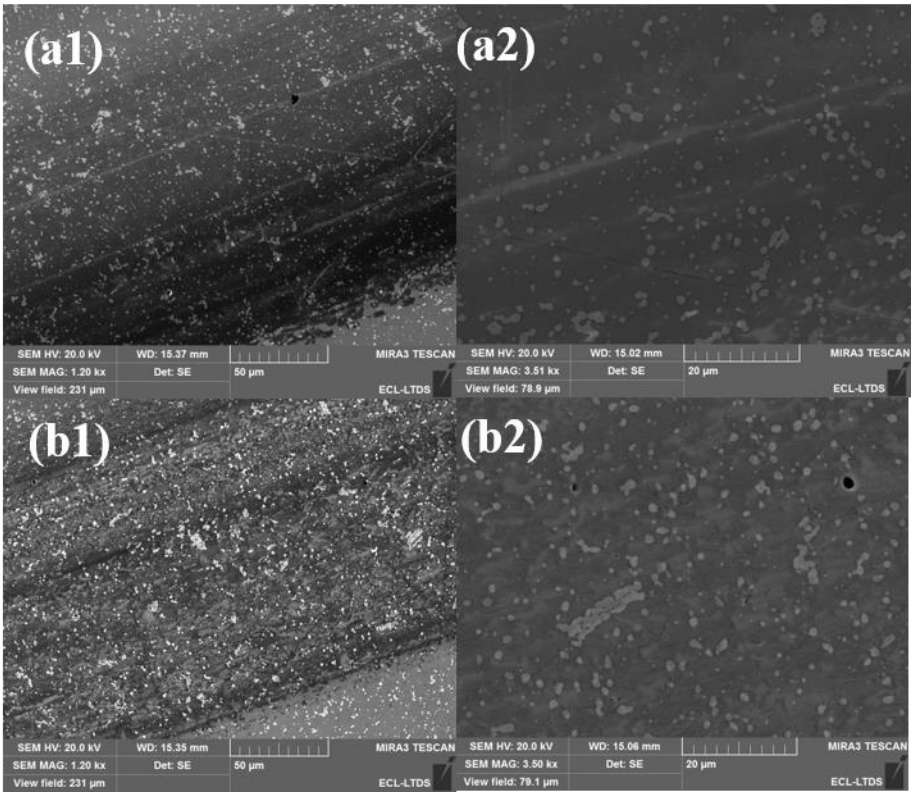

Fig. 4.9 SEM images in secondary electron mode on the steel disk from the a-C:H/steel contact at 0.5GPa (a1, a2) and at 1.0GPa on the ball (b1, b2). 1# represents low magnification, 2# represents high magnification.

Similar with the steel/steel contact (Fig. 4.7), the tribofilm is mainly located at the dark areas. It is clearer than the steel/steel tribo-pair that the surface morphology of the tribofilm is denser at 1.0GPa than at 0.5GPa. This is also evident in the AFM images of the steel disks from the a-

C:H/steel shown in Fig. 4.10 at 0.5GPa (a) and 1.0GPa (b). However, the thickness of the tribofilm does not show a significant change induced by the contact pressure.

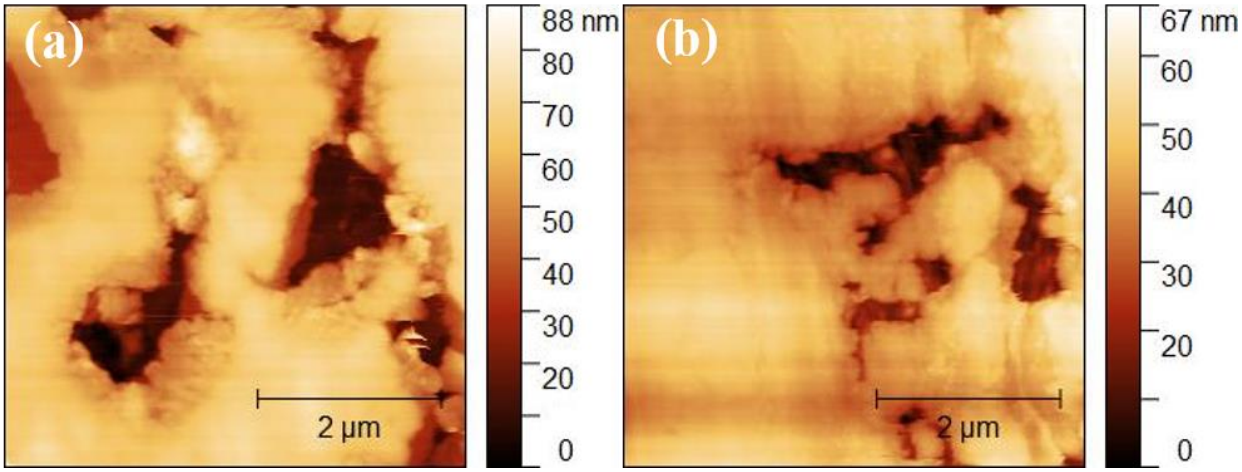

Fig. 4.10 AFM images (5μm * 5μm) on the surfaces of the steel disks from the steel/steel contact at 0.5GPa (a) and 1.0GPa (b).

4.2.1.2 a-C:H/a-C:H

The secondary electron mode SEM images on the surfaces from the a-C:H self-mated contact for the initial contact pressure of 0.5GPa and 1.0GPa are shown in Fig. 4.11.

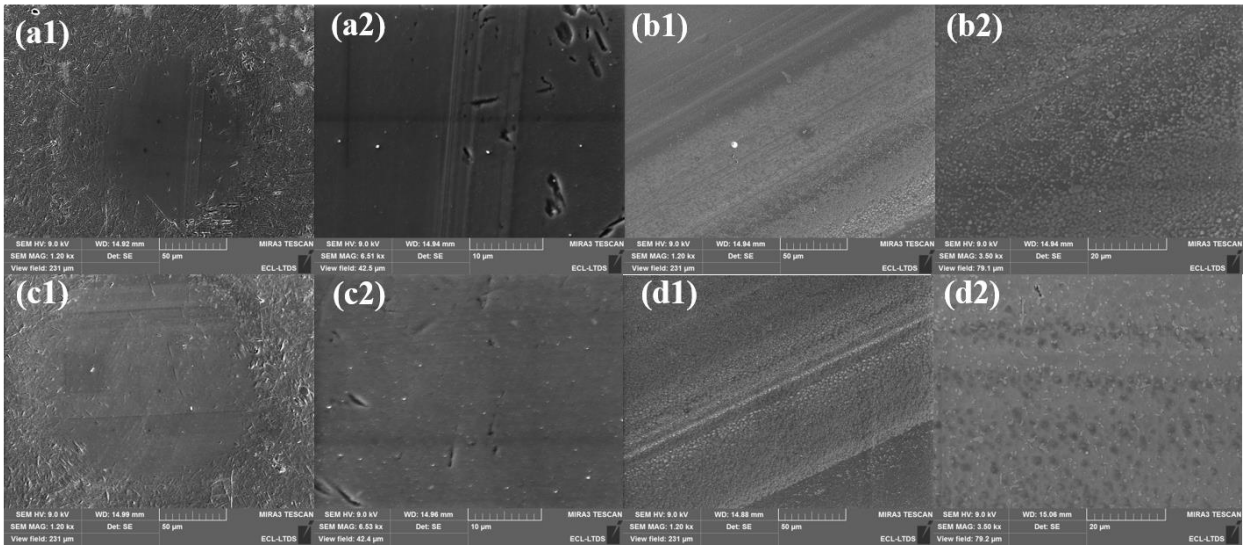

Fig. 4.11 SEM images in secondary electron mode for the a-C:H self-mated contact at 0.5GPa on the ball (a1, a2) and the disk (b1, b2), at 1.0GPa on the ball (c1, c2) and the disk (d1, d2). 1# represents low magnification, 2# represents high magnification.

As discussed in Fig. 4.5, the tribofilm on the a-C:H coated ball is hardly observed at 0.5GPa and 1.0GPa. The scar observed at 0.5GPa (a2) is probably due by the wear on the surface. On the a-C:H coated disk, it is clear that the size of the patches in the tribofilm is much larger at 1.0GPa than at 0.5GPa. This is consistent with the observation by optical microscope.

The AFM images of the a-C:H self-mated contact at 0.5GPa and 1.0GPa are shown in Fig. 4.12 (a1, a2) and (b1, b2), respectively.

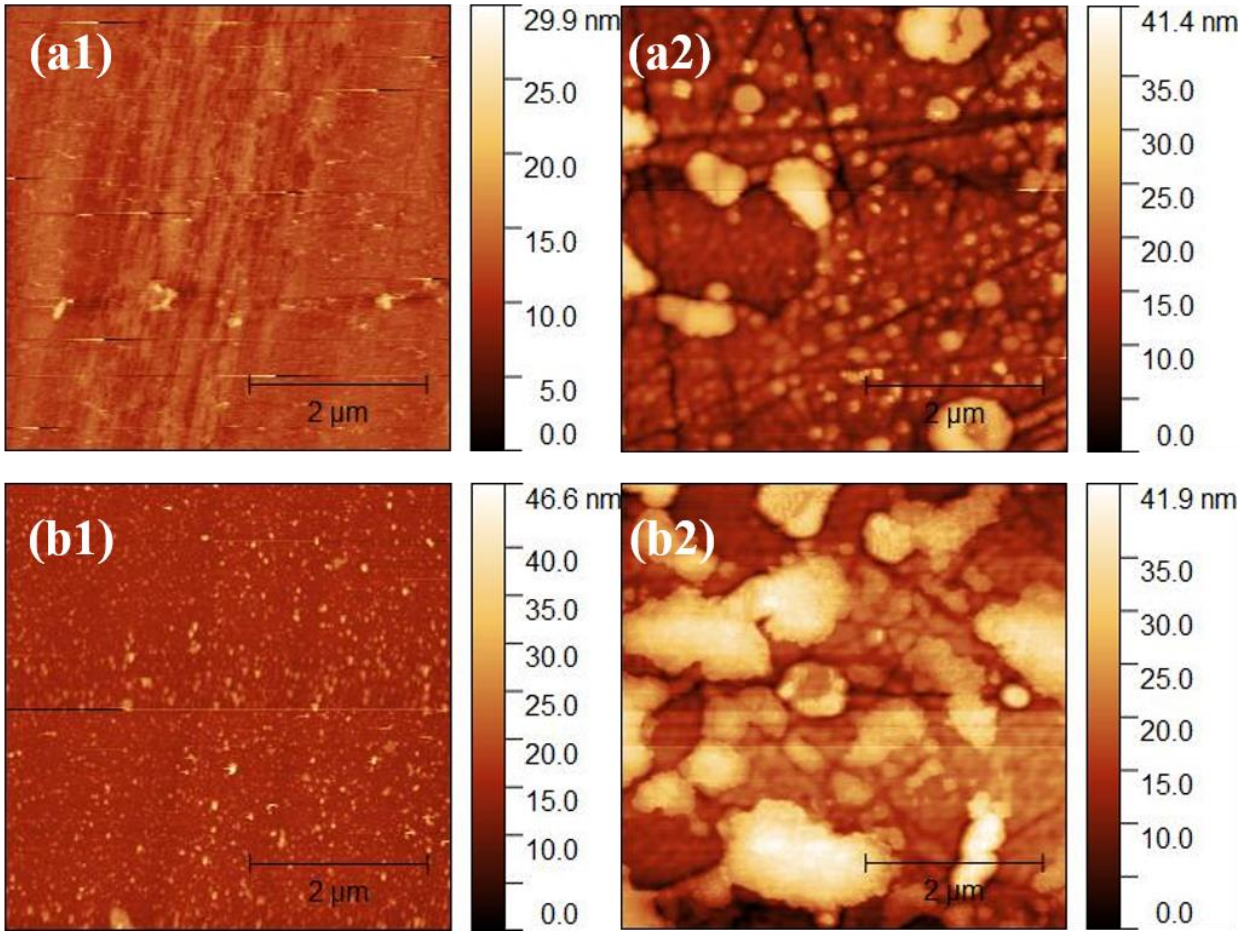

Fig. 4.12 AFM images (5μm * 5μm) on the surfaces of the a-C:H self-mated contact at 0.5GPa on ball (a1) and disk (a2), at 1.0GPa on ball (b1) and disk (b2).

In terms of the a-C:H self-mated contact, on a-C:H balls (Fig. 4.12 a1 & b1), the formation of small particles on the surfaces can be observed. These particles are relatively smaller (46 nm > 30 nm) at 0.5GPa contact load. On the counterpart (Fig. 4.12 a2 & b2), the surface height is similar for both two contact loads (42 nm). Interestingly, the size of the particles on a-C:H disks has a significant difference between 0.5GPa and 1.0GPa. For 0.5GPa, the largest particle size is about 1 μm, and the size distribution is very broad. By contrast, at 1.0GPa, the numerous much larger particles with (size between 1.5 μm and 2.0 μm) could be found. This growth of size corresponds to the conclusions of optical images (Fig. 4.5) and SEM images (Fig. 4.11). However, is the friction reduction tightly related to the size growth of particles? And what is the basic chemical composition of these particles? XPS surface analysis was performed to get the surface chemical information and will be discussed in the following section.

4.2.2 XPS analysis

In chapter 3, XPS analysis indicated that for the steel/a-C:H mixed contact where the friction decreases as the function of the pressure, the quantity of calcium carbonate increases with the growth of the contact pressure. In this part, the friction reduction in boundary lubrication regime at higher load was observed in a-C:H self-mated tribo-pair. Therefore, the XPS analysis is carried out again to analyze the relationship between the calcium carbonate quantity and the friction reduction observed at high load. For the XPS quantification, one significant figure is reserved after the decimal point.

XPS high resolution analysis was performed to investigate the chemical state of the elements present in the tribofilm. Again, similar with the case of ring-on-disk configuration, the binding energy variation of the fitting results of C1s, O1s, Fe2p3/2, Ca2p, S2p, P2p and Zn2p3/2 is hard to distinguish between 0.5GPa and 1.0GPa for ball-on-disk configuration. This implies that the contact pressure does not result in a significant different chemical environment of the species in the tribofilm. The fitting strategy of C 1s and Ca2p spectra is the same with the chapter 3 [1, 2]. These two spectra are present to investigate the chemical structure of the calcium and to compare with the chapter 3. The FWHM, binding energy and corresponding chemical species assignment of C1s, O1s, P2p, S2p, Ca2p, Fe2p3/2 and Zn2p3/2 are listed in **Tab. A3**.

4.2.2.1 Steel/steel

The XPS quantification results of the steel/steel tribo-pair are shown in Tab. 4.3.

Tab. 4.3 XPS quantification results of the steel/steel tribo-pair at initial contact pressure 0.5GPa and 1.0GPa

Elements	Atomic concentration			
	0.5GPa		1.0GPa	
	Steel ball	Steel disk	Steel ball	Steel disk
C	56.9	50.4	55.6	42.8
O	30.7	37.4	33.7	36.8
Fe	4.3	0.4	6.7	0.8
Ca	3.3	9.3	1.5	8.8

S	1.2	0.6	0.3	3.5
P	2.0	1.2	0.7	3.4
Zn	0.7	0.8	0.6	3.2

In terms of the characteristic elements (P, S, Zn, Ca), Ca always has the most significant content on both ball and disk at 0.5GPa and 1.0GPa. However, on each contact surface, the quantity of calcium element does not increase as the function of contact pressure. This is normal because the friction does not decrease as the function of pressure for steel/steel contact.

The XPS high resolution spectra of C 1s and Ca 2p of the steel/steel contact is shown in Fig. 4.13. The carbonate peak located at around 290eV in C 1s and the Ca 2p3/2 peak located at about 347.5eV confirm that the calcium element is in calcium carbonate structure.

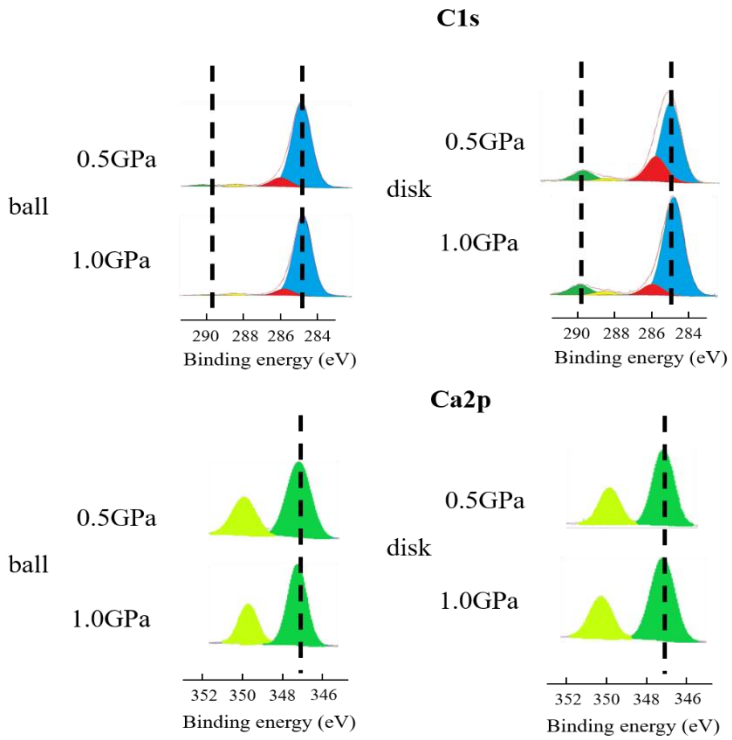

Fig. 4.13 XPS high resolution spectra of C 1s and Ca 2p of the steel/steel contact

4.2.2.2 a-C:H/steel

The XPS quantification results of the a-C:H/steel tribo-pair are shown in Tab. 4.4. The XPS analysis was only carried out on the steel disks at 0.5GPa and 1.0GPa due to the fact that the wear scar on the a-C:H coated ball was not visible.

Tab. 4.4 XPS quantification results on the steel disks from a-C:H/steel tribo-pair at initial contact pressure 0.5GPa and 1.0GPa.

Elements	Atomic concentration	
	Steel disk	
	0.5GPa	1.0GPa
C	50.4	43.3
O	37.4	34.8
Fe	0.4	1.2
Ca	9.3	7.7
S	0.6	3.9
P	1.2	4.4
Zn	0.8	3.7

Similarly with the steel/steel contact, the calcium is the most significant element among all the characteristic elements in the tribofilm of the a-C:H/steel contact. The quantity of calcium is even lower at 1.0GPa than at 0.5GPa. This is also normal because the lower friction at 1.0GPa is not observed either.

The XPS high resolution spectra of C 1s and Ca 2p of the a-C:H/steel contact are given in Fig. 4.14. Again, the calcium carbonate structure is confirmed by the carbonate peak at around 290eV in C 1s spectra and the peak located at 347.5eV in Ca 2p spectra.

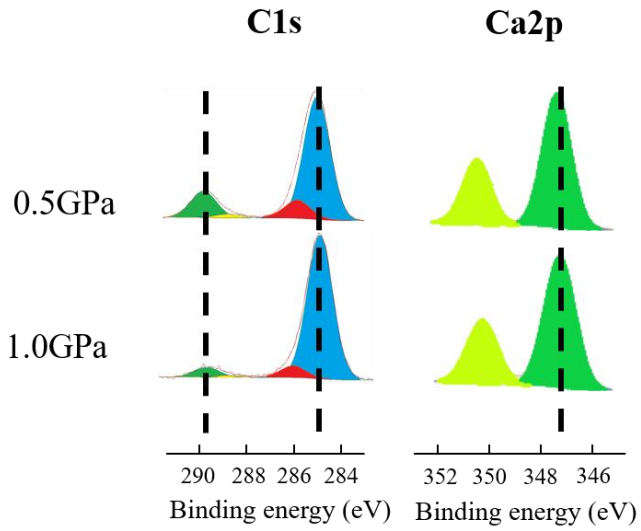

Fig. 4.14 XPS high resolution spectra of C 1s and Ca 2p recorded on the steel disks from a-C:H/steel contact at 0.5GPa and 1.0GPa.

4.2.2.2 a-C:H/a-C:H

The XPS quantification results of the a-C:H/a-C:H tribo-pair are shown in Tab. 4.5.

Elements	Atomic concentration	
	0.5GPa	1.0GPa

	a-C:H ball	a-C:H disk	a-C:H ball	a-C:H disk
C	89.8	76.8	91.1	68.4
O	7.7	**16.0**	6.5	**22.3**
Ca	1.7	3.6	1.2	6.0
S	0.2	0.7	0.20	0.7
P	0.2	1.2	0.20	1.0
Zn	0.1	0.5	0.20	0.6

The calcium is the most significant element on both a-C:H coated ball and disk. On the a-C:H coated ball, the quantity of characteristic elements (P, S, Zn, Ca) is super low on the a-C:H coated ball. This implies that only very few tribofilm is formed on the a-C:H ball. This is consistent with the findings from optical images and SEM images. More importantly, at initial contact pressure of 1.0GPa, the quantity of calcium element on the a-C:H coated disk is almost 80% higher than at 0.5GPa (underlined in color green). This variation was not observed for steel/steel and a-C:H/steel contacts. Simultaneously, the concentration of oxygen on the a-C:H coated disk increases as the function of the pressure. The discussion on the carbon concentration could be very risky due to the fact the carbon can be derived from many molecules (base oil, alkyl structure in anti-wear additive, surfactant in overbased detergent, other additives, etc.) in formulated lubricant. The increase of the calcium concentration as the function of the pressure in a-C:H self-mated tribo-pair is consistent with the results obtained in chapter 3 on not polished steel ring/a-C:H disk contact.

The XPS high resolution spectra of C 1s and Ca 2p of the a-C:H/a-C:H contact are given in Fig. 4.15. As for the steel/steel and a-C:H/steel tribo-pairs, the calcium is confirmed in the structure of calcium carbonate by the carbonate peak in C 1s and calcium peak in Ca 2p. Therefore, it is logical to observe a growth of the quantity of both oxygen and calcium because of the formula $CaCO_3$. Particularly at 1.0GPa, the atomic ratio of O/Ca is very closed to 3:1.

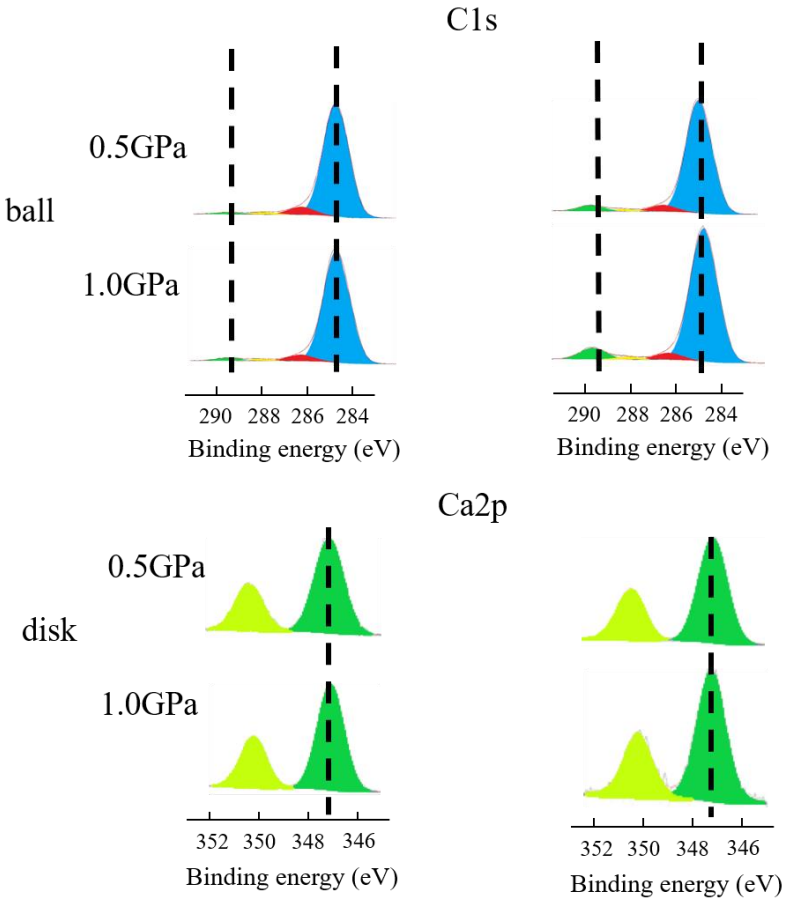

Fig. 4.15 XPS high resolution spectra of C 1s and Ca 2p recorded on the surfaces from the a-C:H self-mated contact at 0.5GPa and 1.0GPa.

It should be noted that the presence of calcium carbonate is confirmed for not only a-C:H self-mated tribo-pair, where the friction reduction occurred, but also for steel/steel and a-C:H/steel contacts. However, the growth of calcium concentration at initial 1.0GPa is only observed for a-

C:H self-mated contact. Based on the results of chapter 3, the question about the crystal structure of calcium carbonate can be raised: is it different in a-C:H self-mated contact comparing to steel/steel and a-C:H/steel, namely, more calcite allotrope for a-C:H/a-C:H tribo-pair? This question will be answered in the next section thanks to the additional FIB/TEM characterizations. On the other hand, considering the fact that the chain length of polyphosphate derived from ZDDP anti-wear additive can also have some influences on the CoF [3-6], it is determined by the area ratio of P2p/Zn3s photo-peaks from XPS fitting results [7-9].

The polyphosphate chain length calculation results are shown in Tab. 4.6. It is well-known that the short chain polyphosphates (orthophosphate, pyrophosphate) could provide relatively lower CoF than long chain polyphosphate (metaphosphate, etc.). For a-C:H self-mated contact, the calculated polyphosphate chain length slightly increases. The polyphosphate species can be assigned to a mix of pyrophosphate (P/Zn = 1) and metaphosphate (P/Zn = 2). Therefore, the possibility of friction reduction due to the formation of a shorter polyphosphate has been eliminated. There will not be further discussions on the relationship between polyphosphate chain length and the contact pressure or materials nature. The focus of this study is the role of detergent in the friction reduction.

Tab. 4.6 The area ratio of P2p/Zn3s

		P2p/Zn3s ratio		
		Steel/steel	a-C:H/a-C:H	a-C:H/steel
0.5GPa	ball	2.17	1.17	/
	disk	1.26	1.49	1.28

1.0GPa	ball	0.63	1.37	/
	disk	1.16	1.58	1.15

4.2.3 TEM/FIB analysis

In chapter 3, using TEM/FIB and FTIR, the crystallization of calcium carbonate and the formation of calcite polymorph at high pressure (740MPa, 1GPa) for steel/a-C:H contact in ring/disk configuration was shown. It was also shown that the quantity of calcium element also increases with the contact pressure. More importantly, the friction reduction was proved to be highly related to the formation of calcite. In this chapter, the reduction of the friction when the contact load increases is observed again in ball/disk reciprocating tests for a-C:H self-mated contact. The growth of calcium carbonate quantity at high pressure (1.0GPa) implies the significant role of calcium in the friction reduction. Therefore, FIB cuts were prepared on the disks of a-C:H and the steel self-mated contacts after sliding tests at 0.5GPa and 1.0GPa with the fully formulated oil. The steel self-mated contact is selected as the reference, in which no friction reduction as the function of pressure is obtained.

Fig. 4.16 shows the TEM images of the FIB cuts at different scales for the a-C:H disk at 0.5GPa (a1, a2, a3), 1.0GPa (b1, b2, b3) and for the steel disk at 0.5GPa (c1, c2, c3) and 1.0GPa (d1, d2, d3).

For the a-C:H self-mated contact, at both 0.5GPa and 1.0GPa, it can be seen that the tribofilm is not continuously and homogeneously generated on the surface. The different contact pressure does not induce a significant difference on the thickness of the tribofilm, which is always in the range of 15 nm and 20nm. These findings are consistent with the AFM results (Fig. 4.12 a2 & b2). The

interlayer between the tribofilm and a-C:H coating is relatively regular. At 1.0GPa, it seems like that the tribofilm is less homogeneous than that of 0.5GPa. If we zoom in (Fig. 4.16 b3), the crystal plane crystal structure can be found in the heterogenous zone. The clearer images can be found in Fig. 4.18, and will be discussed in the following text.

For steel self-mated contact, the tribofilm is more homogenously distributed on the surface. The thickness of the tribofilm is very slightly lower at 1.0GPa, and the thickness varies in the range of 15 nm and 60 nm. This is not consistent with the AFM results, in which a thicker tribofilm is expected at 1.0GPa. There are several possibilities to explain these results. Firstly, AFM is not exactly a technique as reliable as FIB/TEM to measure the tribofilm thickness. Secondly, the selected analysis areas for two techniques are not the same. Even though the analyzed area was carefully chosen (always in the center of the tribofilm), it is likely that in some specific areas, the tribofilm thickness can be significantly different. For both of the two pressures, we can always find some big particles (c1 and d2) in the bulk of the tribofilm. They will be identified in the following text.

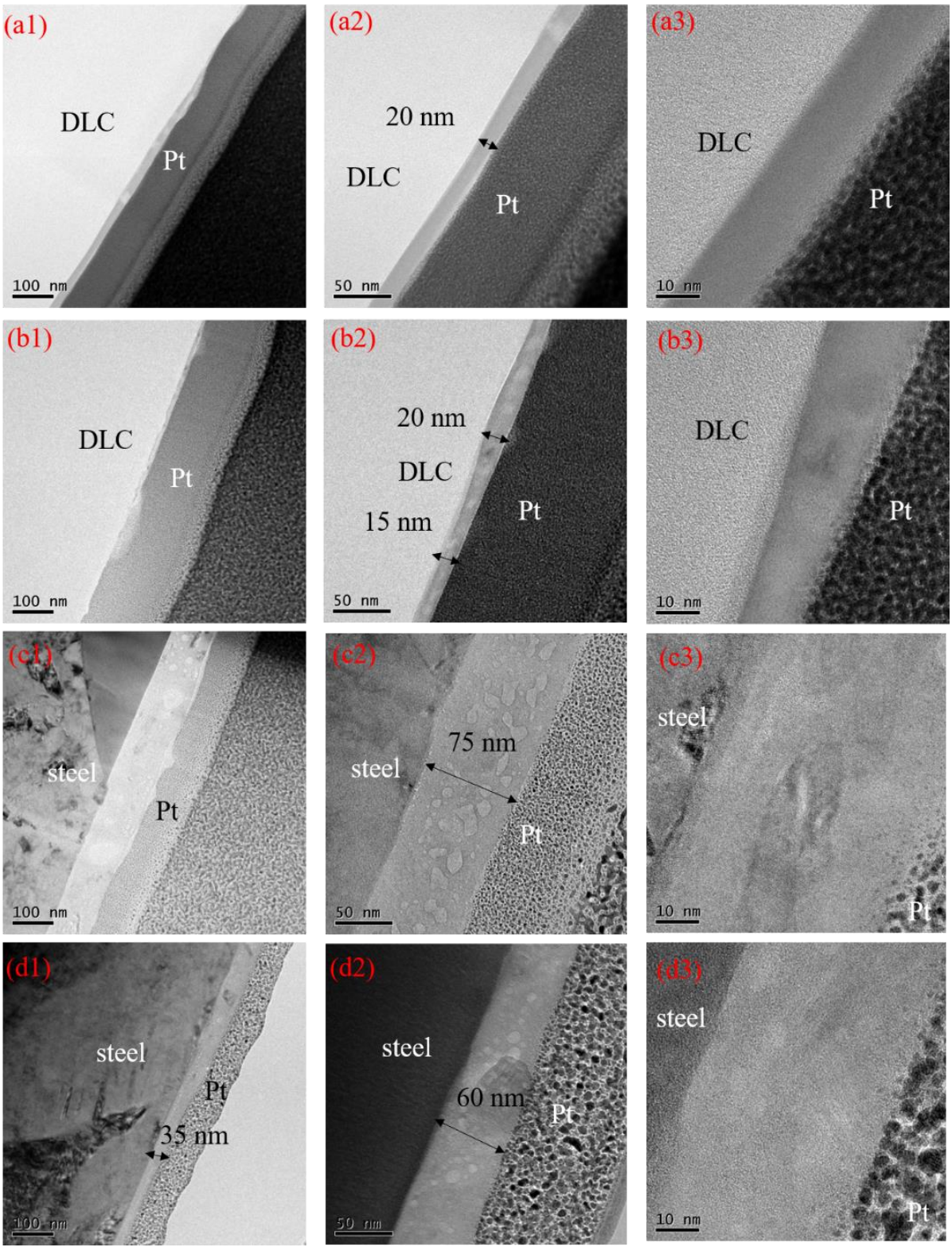

Fig. 4.16 TEM/FIB images at different scales of a-C:H self-mated contact at 0.5GPa (a1, a2, a3), at 1.0GPa (b1, b2, b3) and of steel self-mated contact at 0.5GPa (c1, c2, c3), at 1.0GPa (d1, d2, d3).

Tab. 4.7 shows the EDS quantification results of the characteristic elements present in the tribofilm (obtained from the cross-section). It should be noted that the absolute quantity obtained by EDS is not reliable. It is the ratio between the elements that should be investigated. Therefore, it would be interesting to do the ratio between for example, O and Ca, (Zn + Fe) and S, whose ratio are supposed to be close to 3 ($CaCO_3$) and 1 (ZnS/FeS), respectively. The calculation with carbon is risky considering the fact that carbon can be related to many structures in the tribofilm. The chemical bond of carbon is even more complex and less predictable than oxygen.

Tab. 4.7 EDS quantification on FIB cross-section.

Elements	Atomic Concentration			
	a-C:H disk		steel disk	
	0.5GPa	1.0GPa	0.5GPa	1.0GPa
C	87.6	88.7	26.7	13.2
O	8.8	7.9	44.5	53.6
P	0.7	0.7	6.6	6.4
S	0.3	0.4	6.5	6.3
Ca	2.9	2.5	9.3	15.0
Fe	/	/	1.3	1.1
Zn	0.2	0.3	4.6	4.5

For steel disk, the ratio between O and Ca is 4.78 at 0.5GPa and 3.57 at 1.0GPa. The ratio is little higher than 3 due to the presence of polyphosphate that contains oxygen. Interestingly, at higher pressure, the ratio between O and Ca is closer to 3. If we make the ratio between Zn plus Fe and S, it can be seen that the values are very close to 1. The quantity of Zn is much higher than Fe, which means that S is mainly bonded with Zn rather than Fe. For a-C:H disk, the ratio between O and Ca is very close to 3, which are 3.03 and 3.16 at 0.5GPa and 1.0GPa, respectively. This is partially due to the low concentration of phosphorous, thus low concentration of polyphosphate. The ratio between Zn and S is also very close to 1 at both high and low pressures.

The combination between Ca and O, Zn and S is justified by the EDS mapping results in Fig. 4.17. For a-C:H self-mated contact at 0.5GPa (a1) and 1.0GPa (a2), the mapping results of Zn and S are not given due to the very low signal (low concentration). The tribofilm is rich in Ca and O. For steel self-mated contact at 0.5GPa (b1) and 1.0GPa (b2), the distribution of Zn is well-visibly together with S (marked in red circle). Ca and O are rich in other areas.

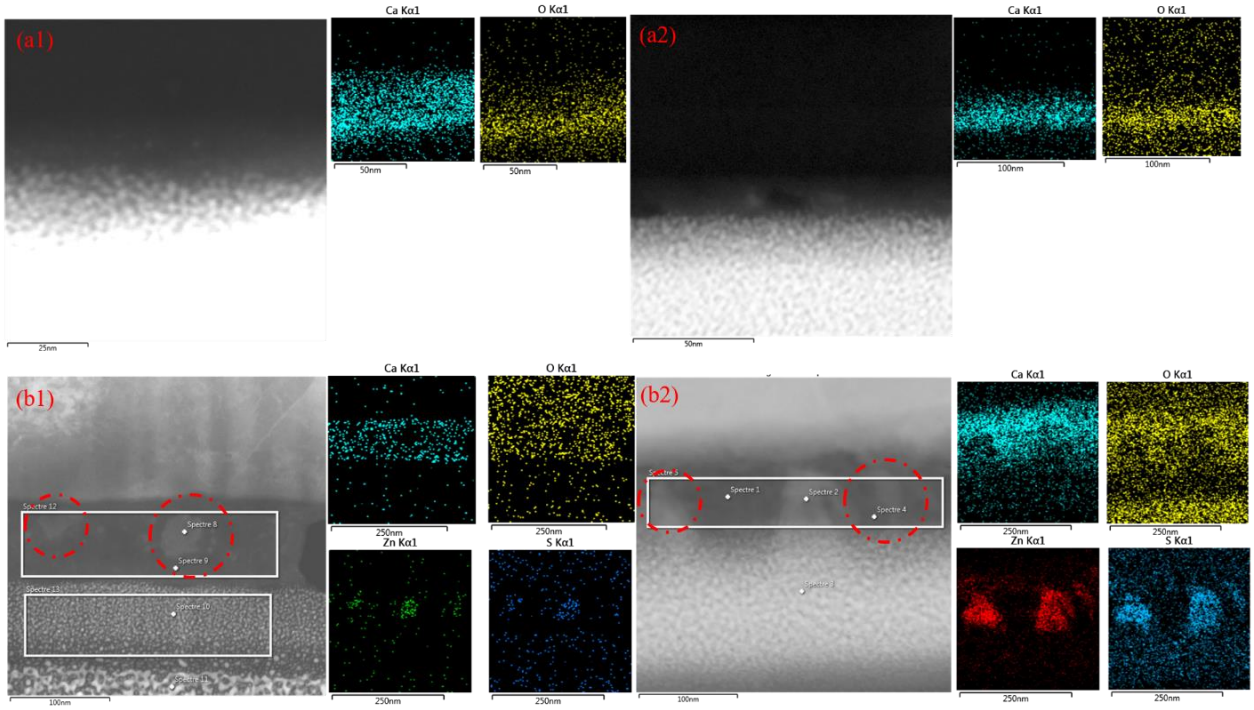

Fig. 4.17 EDS mapping results on the cross-sections of a-C:H self-mated contact at 0.5GPa (a1) and 1.0GPa (a2) and steel self-mated contact at 0.5GPa (b1) and 1.0GPa (b2).

Fig. 4.18 shows the images obtained in diffraction mode performed on the a-C:H disk (a1, a2) and the steel disk (b1, b2) at 0.5GPa and 1.0GPa, respectively. The d-distance of the plane of the crystal is measured by using Gatan GMS 3.

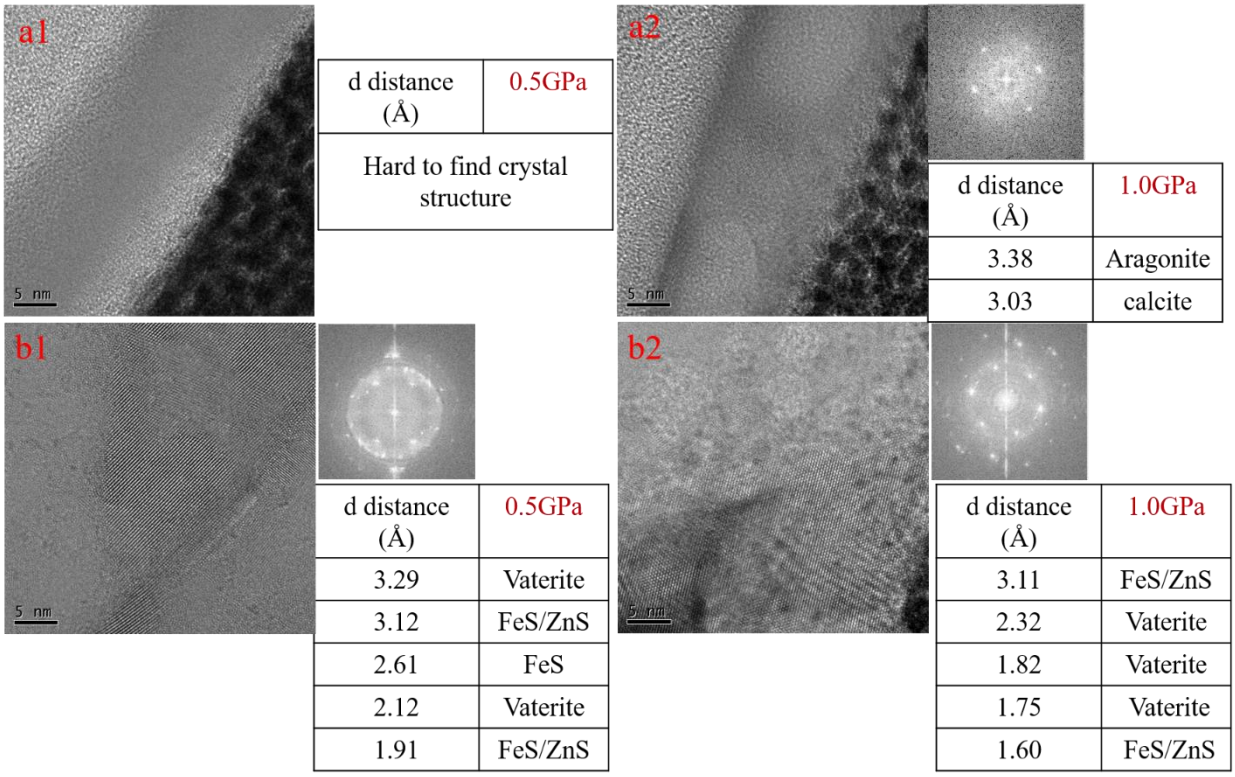

d distance (Å)	0.5GPa
Hard to find crystal structure	

d distance (Å)	1.0GPa
3.38	Aragonite
3.03	calcite

d distance (Å)	0.5GPa
3.29	Vaterite
3.12	FeS/ZnS
2.61	FeS
2.12	Vaterite
1.91	FeS/ZnS

d distance (Å)	1.0GPa
3.11	FeS/ZnS
2.32	Vaterite
1.82	Vaterite
1.75	Vaterite
1.60	FeS/ZnS

Fig. 4.18 TEM diffraction mode on cross-sections and d-distance measurements at a-C:H disk at 0.5GPa (a1) and 1.0GPa (a2), and steel disk at 0.5GPa (b1) and 1.0GPa (b2).

For the a-C:H disk, at 0.5GPa (Fig. 4.18 a1), it is hard to find the crystal structure in the tribofilm. However, at 1.0GPa, very clear crystal structure can be observed in it. The d-distance measurement shows that the crystals are mainly aragonite and calcite [10]. For steel disk, the huge crystal size can be observed in the tribofilm. The measurements show the presence of a mix of ZnS/FeS

together with calcium carbonate [11-12]. It is difficult to distinguish the ZnS and FeS as their d-distance values are very close. It is interesting to notice that the polymorph of calcium carbonate is vaterite even at 1.0GPa (Fig. 4.18 b2). It should be reminded that the friction reduction as the function of pressure was observed for a-C:H self-mated tribo-pair rather than steel self-mated tribo-pair.

4.3 Discussion

In this chapter, the friction tests were performed with a ball/disk configuration, lubricated by the fully formulated lubricant. The friction behaviors were investigated at two contact pressures of 0.5GPa and 1.0GPa for steel/steel, a-C:H (ball)/steel (disk), and a-C:H/a-C:H. The friction reduction at 1.0GPa is observed for the a-C:H self-mated contact. On a-C:H disk (a-C:H self-mated), SEM and AFM show that the size of the patches (rich in calcium carbonate) in tribofilm at 1.0GPa is 1.5 to 2 times larger than at 0.5GPa. Moreover, the higher Ca quantity at 1.0GPa is confirmed by XPS. This is not found in steel/steel and a-C:H/steel tribo-pairs. The FIB/TEM analysis confirms the presence of calcite in the tribofilm formed on the a-C:H disk at 1.0GPa of the a-C:H self-mated tribo-pair. However, at 0.5GPa, the crystal structures are hardly found. FIB/TEM analysis was also conducted on the steel disk (steel self-mated) tribo-pair as reference. The polymorph of calcium carbonate is mainly vaterite, at both 0.5GPa and 1.0GPa. Therefore, the friction reduction at high pressure obtained in a-C:H self-mated contact is tightly related to the formation of calcite with the 2D lamella-like structure (Fig. 3.22). The result is consistent with the chapter 3.

In chapter 3, the friction reduction as the function of pressure is observed in steel/a-C:H mixed contact. For a-C:H self-mated contact, the friction decreases from 320MPa to 500MPa and then

increases from 500MPa to 740MPa. This variation is probably caused by the decomposition of the calcium carbonate characterized by XPS high resolution spectra. The friction reduction is attributed to the formation of calcite in the tribofilm for both steel/a-C:H and a-C:H/a-C:H contacts. Friction reduction is not observed in steel self-mated. The form of calcium carbonate is also vaterite, which is a less 2D lamella-like structure than calcite. Therefore, the catalytic effect from a-C:H DLC is proposed in chapter 3.

In this chapter, the friction reduction is only found for the a-C:H self-mated contact. The tribofilm is also thicker than in chapter 3. On the other hand, we proposed the tribo-catalytic effect based on the a-C:H DLC coating in chapter 3. The inconsistency of the tribo-pair that can provide friction reduction cannot overturn the assumption of tribo-catalytic effect. Because firstly, the very different tribological behaviors can probably be induced by the very different tribometer, tribo-pair configuration and sliding conditions. However, it is difficult to give detailed explanations on how the different sliding methods and sliding conditions influences on the tribological performances. Secondly, the friction reduction and calcite are found in the a-C:H DLC involved tribo-pair. The difference is that a-C:H must be employed on both of the two sides to obtain the friction reduction for ball-on-disk configuration. Interestingly, for both ring/disk and ball/disk configurations, calcite always prefers to be formed at higher contact pressure. And it always plays an irreplaceable effect in friction reduction.

4.4 Conclusions

This chapter investigated the mechanism of friction reduction as the function of pressure in boundary lubrication regime by employing ball-on-disk configuration. The friction tests were performed with steel and a-C:H DLC self-mated contacts and a-C:H DLC/steel mixed contact

lubricated with the same engine oil that the one used in chapter 3. The friction reduction as the function of pressure was only observed in a-C:H self-mated. By coupling multiple surface analysis techniques, the increase of quantity of calcium carbonate on the a-C:H disk is confirmed for the a-C:H self-mated contact. At 0.5GPa, the calcium carbonate kept the amorphous structure which was originated from the detergent additive. However, it crystallizes to calcite at 1.0GPa. By comparison, the allotrope structure of calcium carbonate was always vaterite for steel self-mated contact at both 0.5GPa and 1.0GPa. The friction reduction provided by calcite is attributed to its 2D lamella-like structure. This is consistent with the findings in chapter 3.

References

[1] NIST X-ray photoelectron spectroscopy (XPS) database, version 3.5. (2012, September 15). https://srdata.nist.gov/xps/Default.aspx.

[2] X-ray photoelectron spectroscopy (XPS) reference pages. (n.d.). X-ray Photoelectron Spectroscopy (XPS) Reference Pages. https://www.xpsfitting.com/search/label/About%20This%20Site

[3] Ueda, M., Kadiric, A., & Spikes, H. (2019). On the crystallinity and durability of ZDDP Tribofilm. Tribology Letters, 67(4). https://doi.org/10.1007/s11249-019-1236-x

[4] Zhang, J., Ueda, M., Campen, S., & Spikes, H. (2020). Boundary friction of ZDDP Tribofilms. Tribology Letters, 69(1). https://doi.org/10.1007/s11249-020-01389-4

[5] Spikes, H. (2004). The history and mechanisms of ZDDP. Tribology Letters, 17(3), 469-489. https://doi.org/10.1023/b:tril.0000044495.26882.b5

[6] Cen, H., Morina, A., Neville, A., Pasaribu, R., & Nedelcu, I. (2012). Effect of water on ZDDP anti-wear performance and related tribochemistry in lubricated steel/steel pure sliding contacts. Tribology International, 56, 47-57. https://doi.org/10.1016/j.triboint.2012.06.011

[7] Zhou, J. G., Thompson, J., Cutler, J., Blyth, R., Kasrai, M., Bancroft, G. M., & Yamaguchi, E. (2010). Resolving the chemical variation of phosphates in thin ZDDP Tribofilms by X-ray photoelectron spectroscopy using synchrotron radiation: Evidence for Ultraphosphates and organic phosphates. Tribology Letters, 39(1), 101-107. https://doi.org/10.1007/s11249-010-9619-z

[8] Crobu, M., Rossi, A., Mangolini, F., & Spencer, N. D. (2012). Chain-length-identification strategy in zinc polyphosphate glasses by means of XPS and ToF-SIMS. Analytical and Bioanalytical Chemistry, 403(5), 1415-1432. https://doi.org/10.1007/s00216-012-5836-7.

[9] Čoga, L., Akbari, S., Kovač, J., & Kalin, M. (2021). Differences in nano-topography and tribochemistry of ZDDP tribofilms from variations in contact configuration with steel and DLC surfaces. Friction, 10(2), 296-315. https://doi.org/10.1007/s40544-021-0491-7.

[10] Donald, L. G. (1961). CRYSTALLOGRAPHIC TABLES FOR THE RHOMBOHEDRAL CARBONATES. THE AMERICAN MINERALOGIST, 46, November-December, 1283-1316.

[11] Gomes, A., Mendonça, M. H., da Silva Pereira, M. I., & Costa, F. M. A. (2000). Iron sulfide electrodeposits: Effect of heat treatment on composition and structure. Journal of Solid State Electrochemistry, 4(3), 168–176. https://doi.org/10.1007/s100080050015

[12] Patel, P. C., Srivastava, N., & Srivastava, P. C. (2013). Synthesis of wurtzite ZnS nanocrystals at low temperature. Journal of Materials Science: Materials in Electronics, 24(10), 4098-4104. https://doi.org/10.1007/s10854-013-1367-z

Chapter 5 Friction reduction in ball-on-disk configuration lubricated by base oil blended with detergent additive

Following by chapter 4, the identical tribo-pairs were selected in this chapter to verify the role of the detergent additive in the friction reduction observed as the function of the contact pressure. The tribo-pairs were lubricated by the base oil blended with the detergent additive used in the fully formulated lubricant. After the tests, surface analyses were carried out to reveal the friction mechanism.

Introduction

Chapter 3 showed that for ring-on-disk configuration, the friction reduction was obtained by the formation of aragonite and calcite into the contact area. Both structures were obtained from amorphous calcium carbonate. Its crystallization and the formation of the different allotrope structures was obtained by combining contact pressure shear stress. In chapter 4, the friction reduction was again justified to be related to the calcite crystal for ball-on-disk configuration in reciprocating sliding tests. The aim of this chapter is to verify and to emphasize the role of the detergent additive in the friction reduction observed when the contact pressure increases. Therefore, the detergent additive alone was blended with the base oil in concentration of 1wt%, which is the commonly used concentration of other additives like ZDDP, MoDTC and other friction modifiers.

The sliding conditions were the same that in chapter 4. At least three tests were conducted under each sliding condition to verify the repeatability. After the tests, the dimension and the depth of the wear tracks were characterized by optical microscope and interferometer. Topographical images were obtained by SEM and AFM. Surface chemical composition was analyzed by XPS. FIB cuts on tribofilms were conducted and the cross-sections were analyzed by TEM to have a deeper understanding on tribofilms' structure.

5.1 Tribological results

5.1.1 Friction results

Fig. 5.1 displays the friction curves of steel/steel, a-C:H/steel and a-C:H/a-C:H at 0.5GPa and 1.0GPa with base oil containing 1wt% detergent additive (referred as BoD) used in the fully formulated lubricant. Only one curve is shown for each tribo-pair. The initial λ value was less than 0.1. Therefore, initially, the sliding tests were conducted in boundary lubrication regime.

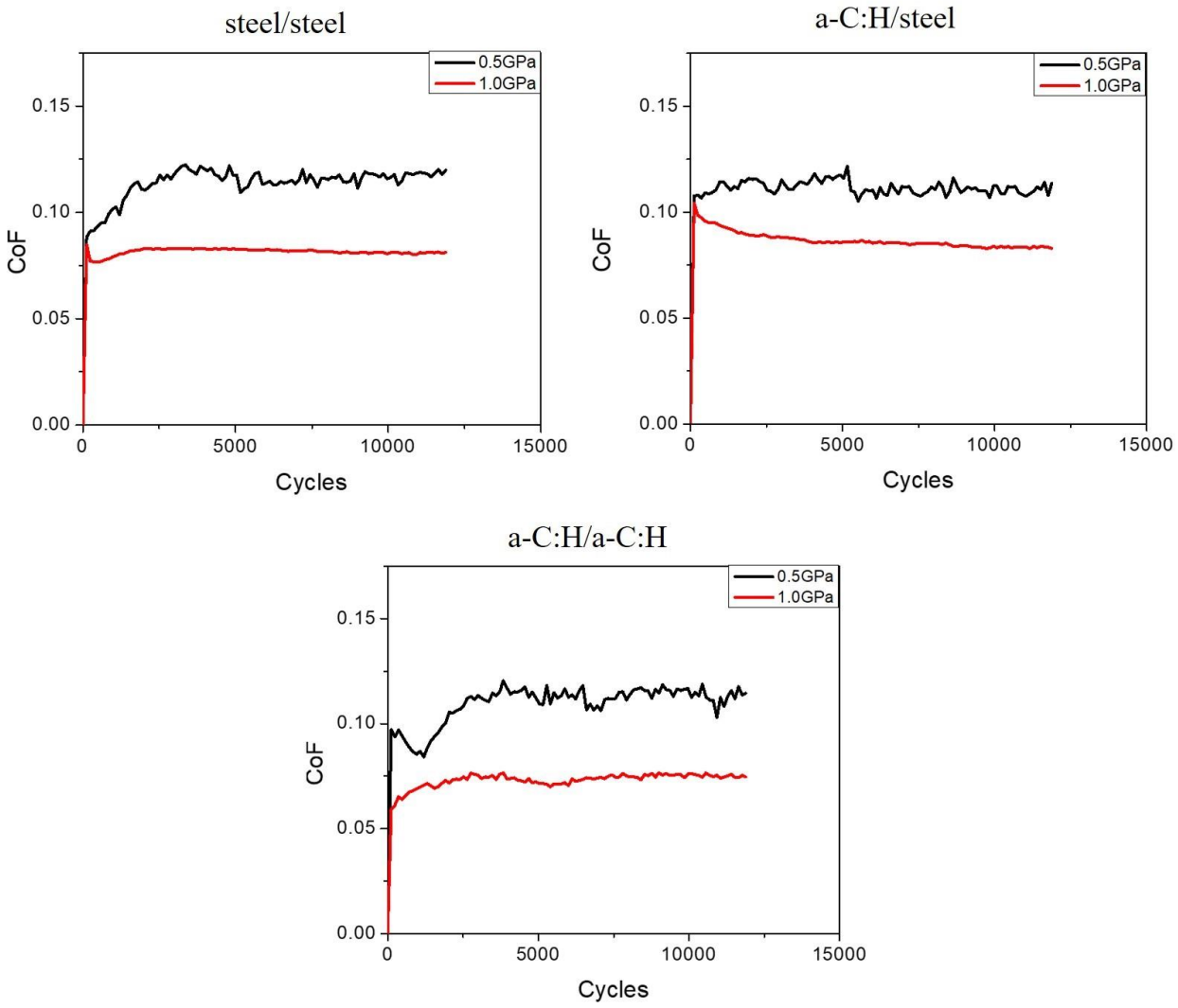

Fig. 5.1 Friction curves of steel/steel, a-C:H/steel and a-C:H/a-C:H at 0.5GPa and 1.0GPa lubricated by base oil blended with 1wt% detergent additive.

At 0.5GPa, for each of the tribo-pair, the steady state CoF is reached after 5000 cycles. At 1.0GPa, the steady state CoF is obtained much more rapidly, in less than 3000 cycles. In chapter 4, the friction decreased as the function of the contact pressure for a-C:H self-mated contact. However, this friction reduction is observed in steel self-mated contact and a-C:H/steel mixed contact as well, when the BoD is used as lubricant.

The steady state CoF is given in Fig. 5.2. The CoF is decreased for about 25% to 30% at 1.0GPa for each of the tribo-pair. At both 0.5GPa and 1.0GPa, the steady state CoF is very similar for each tribo-pair, which is around 0.11 and 0.08, respectively. Interestingly, the CoF at 0.5GPa with BoD (~0.11) is lower than the CoF (0.13 – 0.15) obtained when using the fully formulated lubricant (see Fig. 4.2).

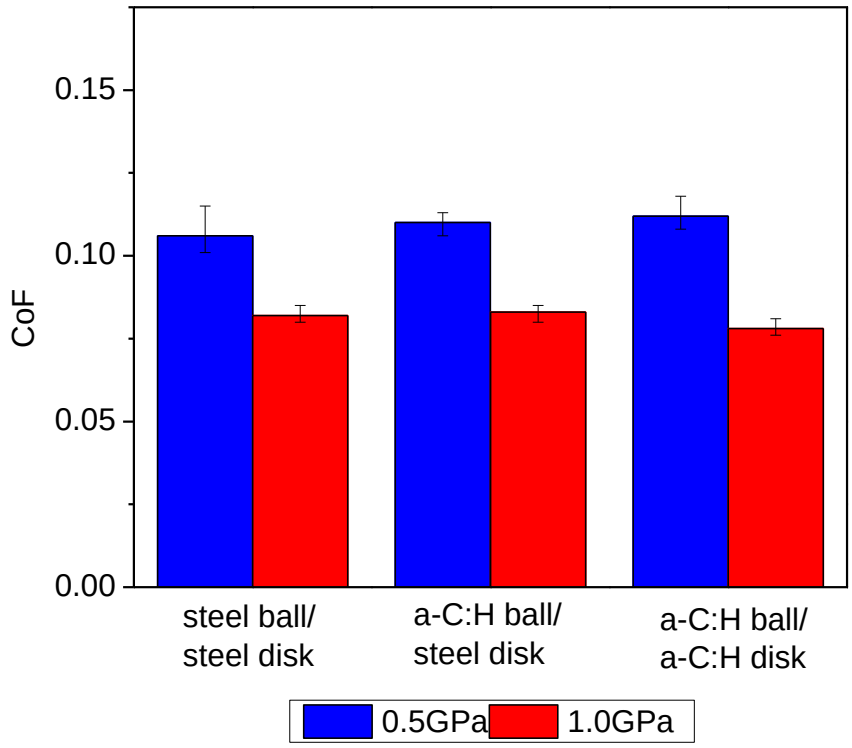

Fig. 5.2 Steady state CoF at 0.5GPa and 1.0GPa for steel/steel, a-C:H/steel and a-C:H/a-C:H tribo-pairs, using BoD as lubricant

5.1.2 Wear results

5.1.2.1 steel/steel

Fig. 5.3 shows the optical images of the wear scars for steel/steel tribo-pair when BoD lubricant is used.

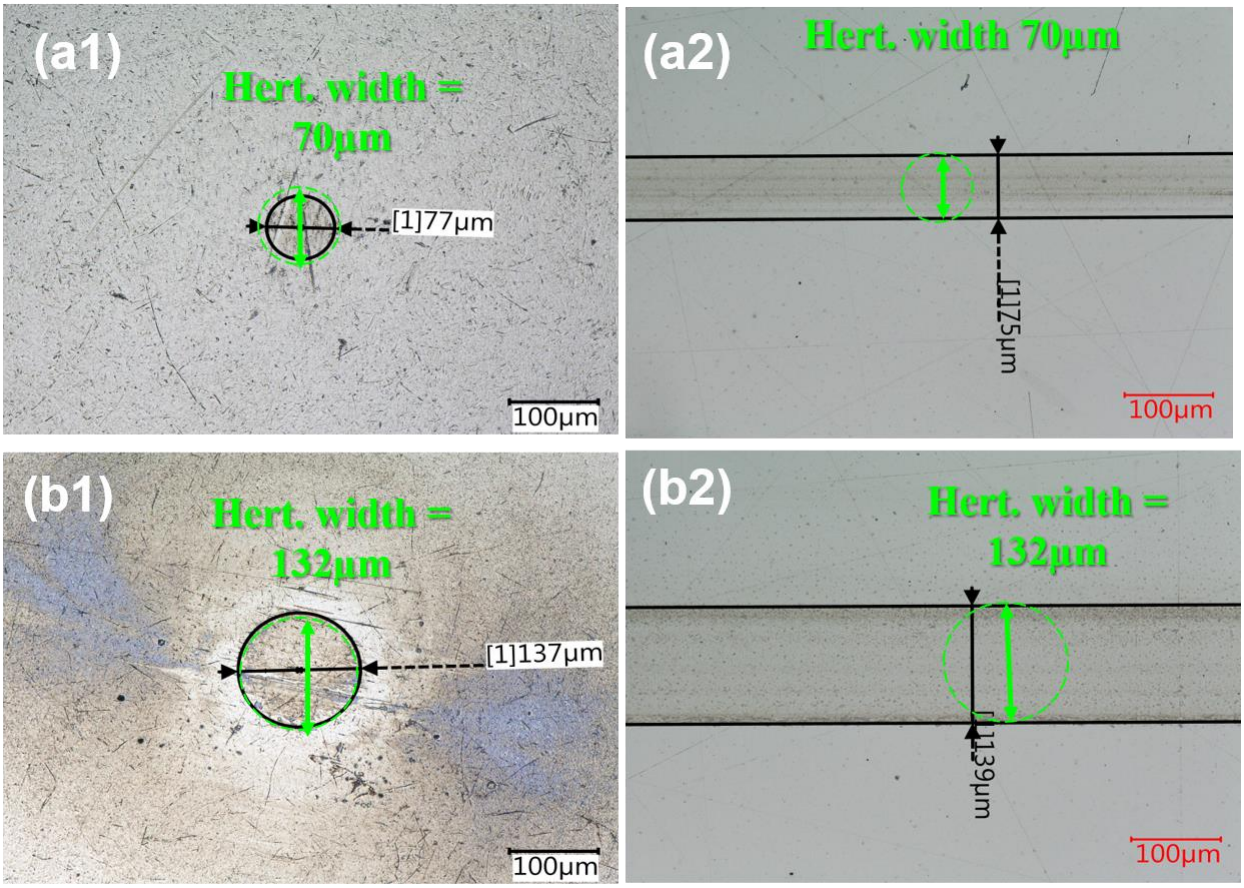

Fig. 5.3 The optical images of wear scar after friction tests with BoD in the steel/steel tribo-pair at 0.5GPa (a1, a2), and at 1.0GPa (b1, b2)

For steel/steel contact, the diameter of the wear scar follows well the hertzian values (marked in green circle) and the tribofilm is well-visible on both ball and disk. Comparing with the Fig. 4.3, the use of BoD lubricant slightly reduces the size of the wear track. The morphological difference between 0.5GPa and 1.0GPa is not clear.

5.1.2.2 a-C:H/steel

Fig. 5.5 shows the optical images of the wear scars for a-C:H/steel tribo-pair when BoD lubricant is used.

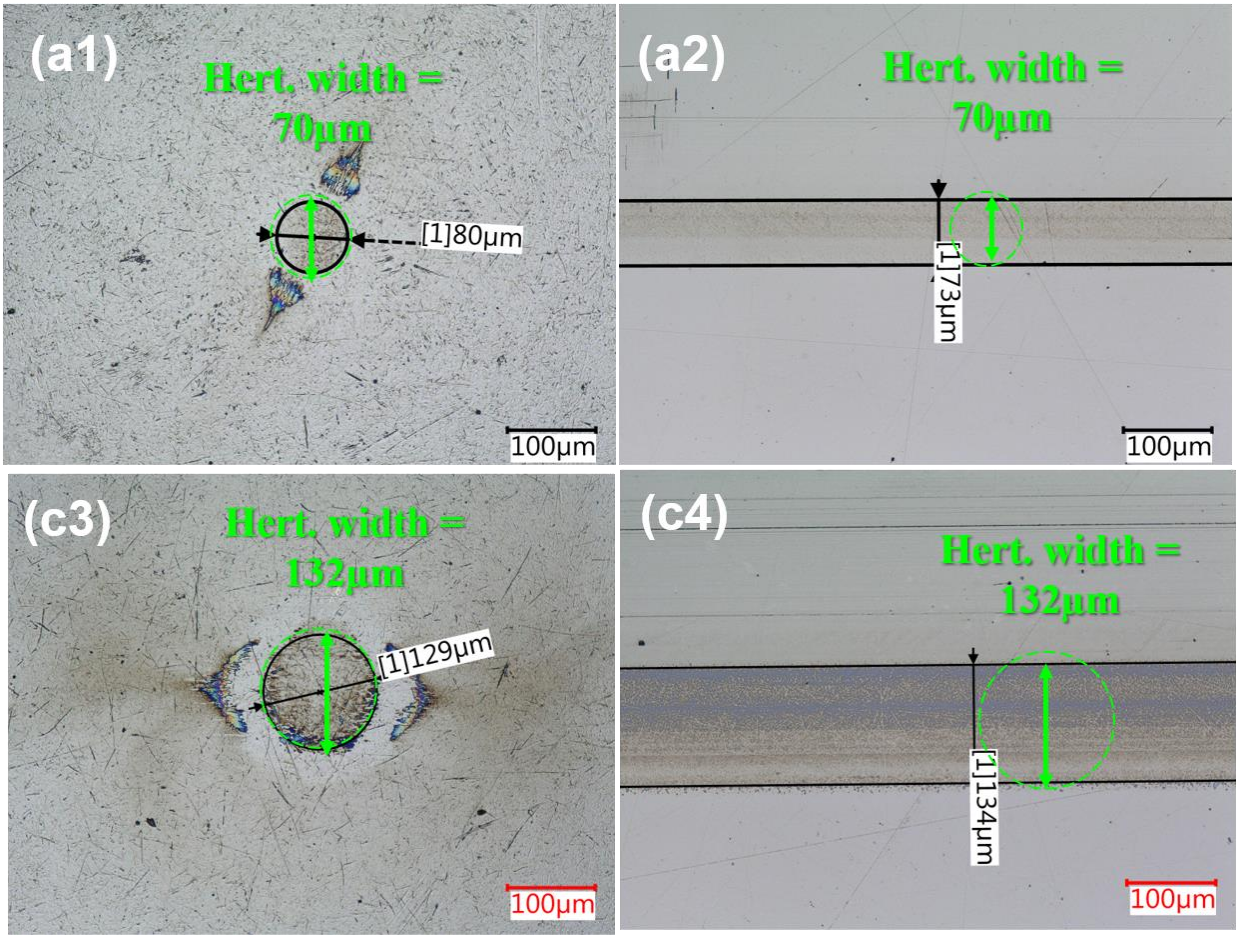

Fig. 5.5 The optical images of wear scar after friction tests with BoD in the a-C:H/steel tribo-pair at 0.5GPa (a1, a2), and at 1.0GPa (b1, b2)

For a-C:H/steel contact, the tribofilm is only observed on steel surface when fully formulated oil is used (see Fig. 4.4). On the a-C:H surface, the wear scar is not even visible. By contrast, the tribofilm is visible on both a-C:H and steel when BoD is used. This implies that the chemical reactivity between detergent additive and a-C:H DLC ball depends on the formulation of the lubricant. The other additives present in the fully formulated lubricant can probably limit the

chemical reaction between the detergent and the a-C:H DLC. The wear diameter follows well the values proposed by the hertzian theory. The wear on the surfaces is expected to be neglectable. This partially justifies the anti-wear role of the detergent additive.

5.1.2.3 a-C:H/a-C:H

Fig. 5.6 shows the optical images of the wear scars for a-C:H/a-C:H tribo-pair when BoD lubricant is used.

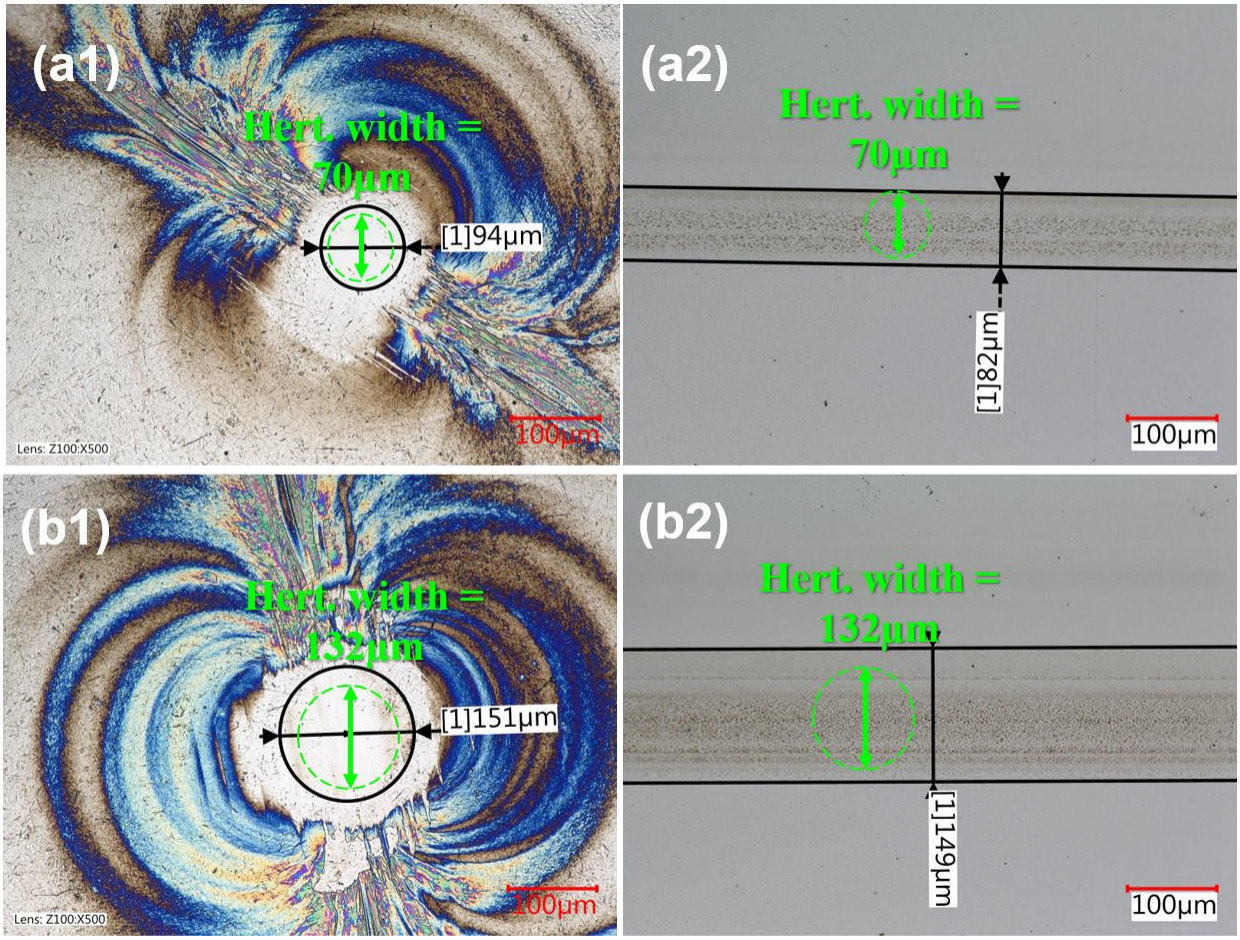

Fig. 5.6 The optical images of wear scar after friction tests with BoD in the a-C:H self-mated tribo-pair at 0.5GPa (a1, a2), and at 1.0GPa (b1, b2)

For a-C:H DLC self-mated contact, it seems like that the surface of the a-C:H coated ball rubbed by BoD (Fig. 5.6 a1, b1) is less clean than the surface of the a-C:H coated ball rubbed by the fully

formulated oil (Fig. 4.5 a1, a2). This may due to the lower concentration of detergent additive in BoD than in the fully formulated oil [1,2]. In a commercial fully formulated oil, the concentration of detergent additive can be more than 10%. Outside the wear track of the ball, the “blue traces” are assumed to be the wear particles and/or oil residues. The tribofilm is not well-visible. The tribofilm is mainly formed on the a-C:H coated disk. It seems like that the tribofilm is more condensed at 1.0GPa (the particles in the tribofilm are closer). This will be characterized by SEM and AFM in the following context. The wear diameter on the both two surfaces is slightly larger than the values predicted by the Hertz theory, which are 70µm and 132µm at 0.5GPa and 1.0GPa, respectively. Therefore, it suggests that the moderate wear happens in a-C:H self-mated contact.

5.1.3 Contact pressure and lubrication regime verification

In chapter 4, the contact pressures after the friction tests were calculated due to the measured wear diameter larger than those calculated by hertz theory. However, in this chapter, the wear size corresponds well to the hertz theory for the tribo-pairs of steel/steel and a-C:H/steel. For the a-C:H self-mated contact, the size of the wear scar measured in this chapter is also closer to the hertzian values than the size measured in chapter 4. Therefore, the contact pressure after the friction tests was not calculated to verify that the increase of the real contact pressures.

But the root mean square (Sq, nm) surface roughness after friction tests is measured by interferometer and listed in Tab. 5.1 for lubrication regime calculation. Comparing with the initial surface roughness, after the friction tests, the surface roughness notably increases due to the formation of the tribofilm. Therefore, it can be concluded that the friction tests remain in boundary lubrication regime. The friction reduction at 1.0GPa for all the tribo-pairs is not induced by a change of lubrication regime during the tests.

Tab. 5.1 Root mean square surface roughness of each tribo-pair after friction tests

Sq (nm)		steel/steel		a-C:H/a-C:H		a-C:H/steel	
		ball	disk	ball	disk	ball	disk
Base oil+ 1wt% detergent	0.5GPa	62±12	25±5	52±9	90±23	40±12	88±10
	1.0GPa	65±8	26±2	55±6	125±25	54±8	120±20

5.2 Surface analysis

5.2.1 Topography (SEM+AFM)

After the friction tests, the samples were characterized by SEM in secondary electron mode. Low and high magnifications were used for each sample. The AFM characterization was performed in a smaller scale (5µm*5µm) to verify the eventual topography variations induced by the contact load. In chapter 4, the larger particle size in the tribofilm is observed on a-C:H disk of a-C:H self-mated contact. For the steel/steel and a-C:H/steel tribo-pairs, the friction reduction as the function of pressure is not observed and the growth of the particle size in the tribofilm is not clear either. Therefore, in this chapter, the growth of the particle size in the tribofilm is expected to be characterized for each of the tribo-pair.

5.2.1.1 steel/steel

The secondary electron mode SEM images on the surfaces from the steel/steel contact for 0.5GPa and 1.0GPa are shown in Fig. 5.7 (a1, a2, b1, b2) and (c1, c2, d1, d2). The white spots on the surface of the steel disks (b1, b2, d1, d2) have been explained in chapter 4.

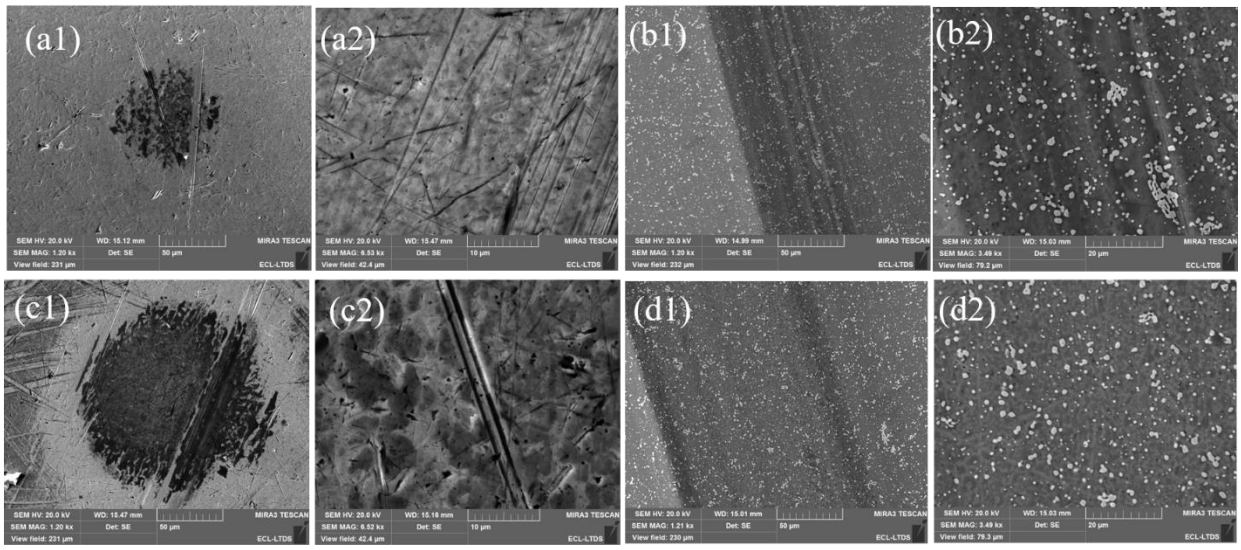

Fig. 5.7 SEM images in secondary electron mode for the steel/steel contact at 0.5GPa on the ball (a1, a2) and the disk (b1, b2), at 1.0GPa on the ball (c1, c2) and the disk (d1, d2). 1# represents low magnification, 2# represents high magnification.

The tribofilm is clearly observed (dark areas) on both the steel ball and the steel disk. The size of the patches on the steel ball is a little larger at 1.0GPa (c2) than at 0.5GPa (a2). On the steel disks, it's difficult to discern the morphological changes brought by the contact pressure.

The AFM images on the surfaces of the steel/steel contact is shown in Fig. 5.8.

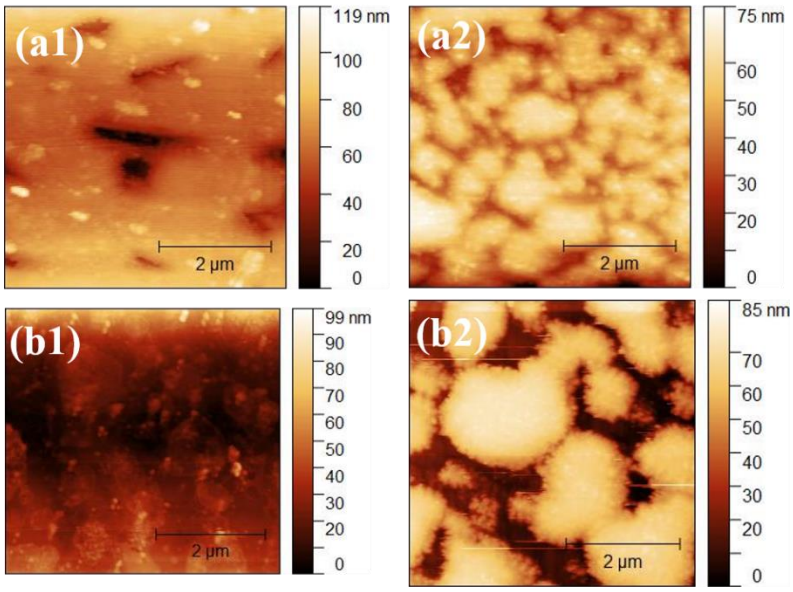

Fig. 5.8 AFM images (5μm * 5μm) on the surfaces from the steel/steel contact at 0.5GPa on ball (a1) and disk (a2), at 1.0GPa on ball (b1) and disk (b2).

For steel/steel contact, it seems that the size of the patches in the tribofilm at 1.0GPa is slightly bigger than 0.5GPa. This is not very clear under SEM characterization. However, the thickness of the tribofilm is not notably modified by the contact pressure. The thickness is around 80 nm on the steel disk, and 100 nm to 120 nm on the ball. The larger particle size observed by SEM at 0.5GPa on the steel ball is not clear under AFM characterization.

5.2.1.2 a-C:H/steel

The secondary electron mode SEM images on the surfaces from the a-C:H/steel contact for 0.5GPa and 1.0GPa are shown in Fig. 5.9 (a1, a2, b1, b2) and (c1, c2, d1, d2).

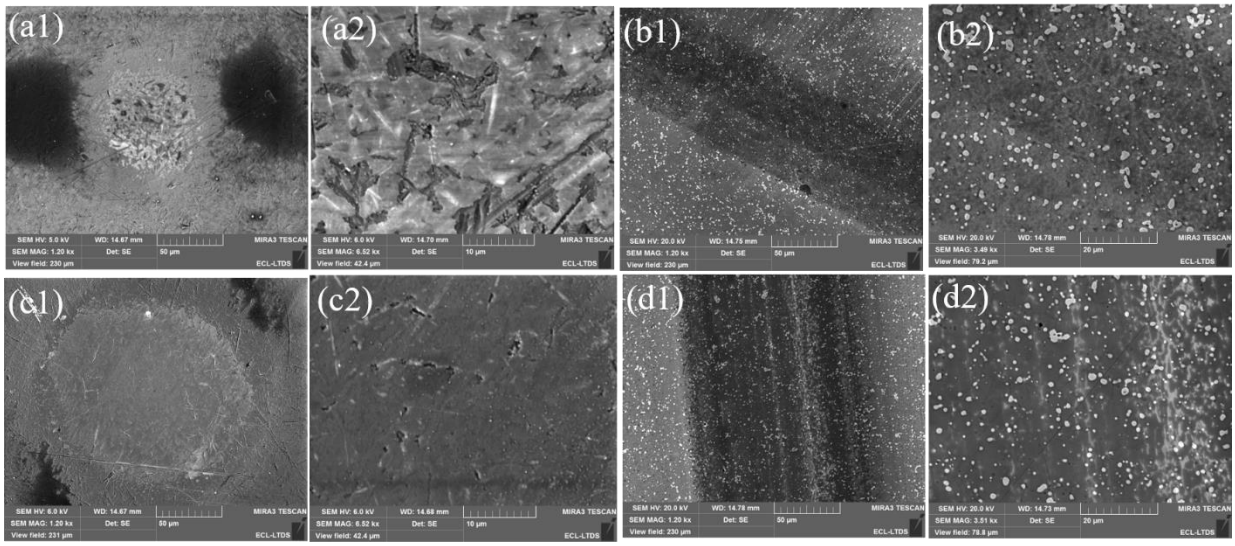

Fig. 5.9 SEM images in secondary electron mode for the a-C:H/steel contact at 0.5GPa on the ball (a1, a2) and the disk (b1, b2), at 1.0GPa on the ball (c1, c2) and the disk (d1, d2). 1# represents low magnification, 2# represents high magnification.

The patchy tribofilm is observed on both of the two surfaces. On the a-C:H coated ball, at 1.0GPa, the “islands” in the tribofilm are connected with each other (c2). By comparison, at 0.5GPa, these

islands are separated on the surface of the a-C:H coated ball. On the steel disk, the tribofilm is also more compact at 1.0GPa (d2).

The AFM images on the surfaces of the a-C:H/steel contact is shown in Fig. 5.10.

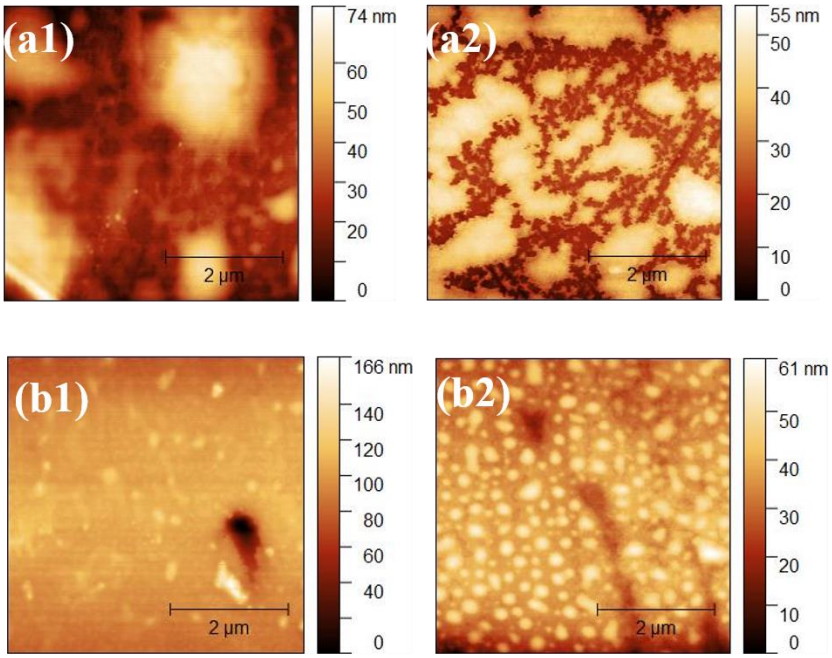

Fig. 5.10 AFM images (5µm * 5µm) on the surfaces from the a-C:H/steel contact at 0.5GPa on ball (a1) and disk (a2), at 1.0GPa on ball (b1) and disk (b2).

For a-C:H/steel contact, the thickness of the tribofilm on the steel disk is about 60 nm at both 0.5GPa and 1.0GPa. By contrast, the tribofilm is much thicker on the a-C:H coated ball at 1.0GPa (166 nm) than at 0.5GPa (74 nm). The small "islands" can be found on a-C:H surface at 0.5GPa (a1). At 1.0GPa, these "islands" are connected with each other. Similarly, on steel disk, the separated patches at 0.5GPa (a2) are connected with each other at 1.0GPa (b2). This is consistent with the findings in Fig. 5.9.

5.2.1.3 a-C:H/a-C:H

The secondary electron mode SEM images on the surfaces from the a-C:H self-mated tribo-pair for 0.5GPa and 1.0GPa are shown in Fig. 5.11 (a1, a2, b1, b2) and (c1, c2, d1, d2).

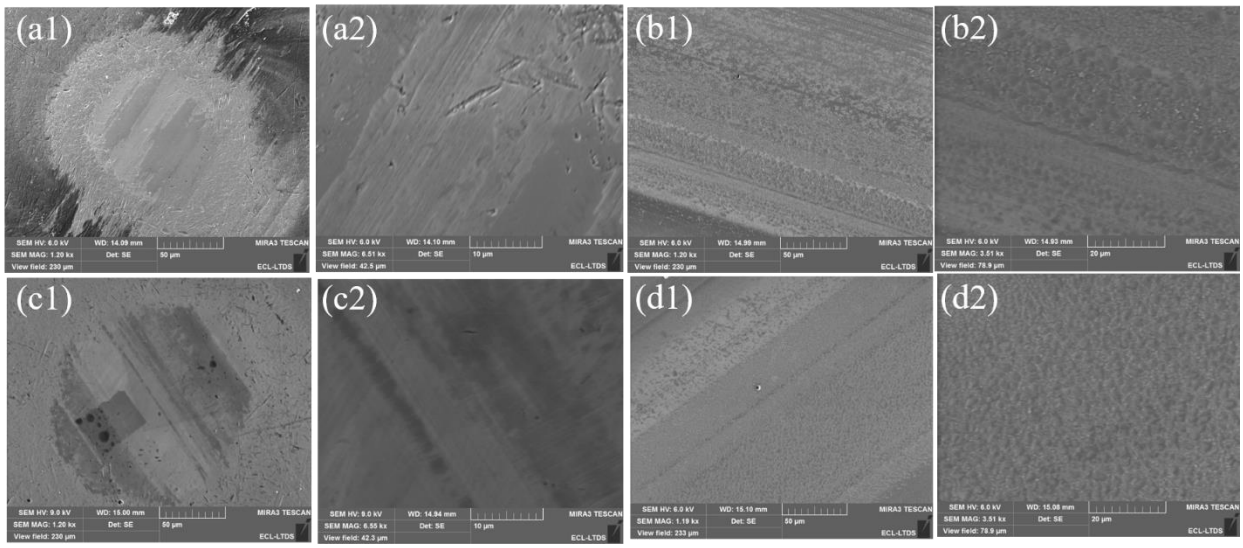

Fig. 5.11 SEM images in secondary electron mode for the a-C:H self-mated contact at 0.5GPa on the ball (a1, a2) and the disk (b1, b2), at 1.0GPa on the ball (c1, c2) and the disk (d1, d2). 1# represents low magnification, 2# represents high magnification.

For the a-C:H self-mated contact, optical microscope shows that the triboiflm mainly forms on the a-C:H disk (Fig. 5.6 a2, b2). However, in the SEM images (a1, a2, c1, c2) a certain amount of tribofilm can also be observed through the contrast between dark and bright areas. On the counterpart, the well-visible tribofilm is observed. Unlike the findings of large patches on the a-C:H disk at 1.0GPa in chapter 4, the size of patches is similar at both 0.5GPa and 1.0GPa when BoD is used. The difference is that at 1.0 GPa, there are more large particles on the surface, and their distribution is more compact.

The AFM images on the surfaces of the a-C:H self-mated contact is shown in Fig. 5.12.

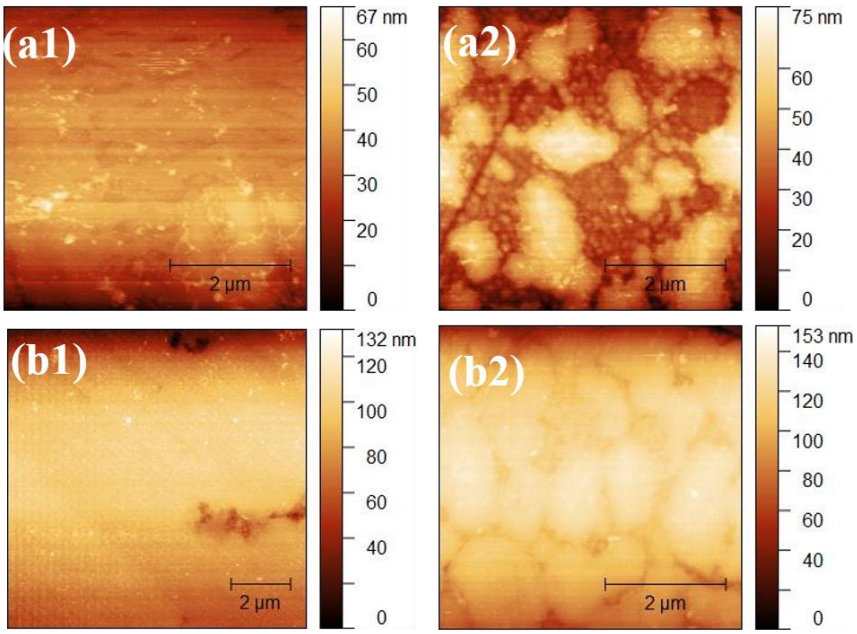

Fig. 5.12 AFM images (5µm * 5µm) on the surfaces from the a-C:H/a-C:H contact at 0.5GPa on ball (a1) and disk (a2), at 1.0GPa on ball (b1) and disk (b2).

On the a-C:H balls (Fig. 5.12 a1, b1), the thickness of the tribofilm is significantly increased at 1.0GPa, from 67 nm to 132 nm. On the counterpart (Fig. 5.5 a2, b2), the thickness of the tribofilm also notably grows from 75 nm at 0.5GPa to 153 nm at 1.0GPa. As mentioned by the results of SEM, the tribofilm includes both large and small partilces at 0.5GPa. At 1.0GPa, the quantity of large particles increases. This is not the same as using fully formulated lubricant. Therefore, the surface height difference cannot be simply explained by the formation of larger particles that are induced by the higher load. It is possible that these particles are physically overlapped or chemically changed by the contact pressure. More details can be given after the analyses of XPS and FIB/TEM.

One of the interesting points is that, the growth of the particles size is observed on disk for each tribo-pair. The friction reduction at higher load is also obtained for each tribo-pair. In chapter 4, the growth of particle size is only observed in a-C:H self-mated contact, which is the only case of

friction reduction at high contact load. Therefore, it can be suggested that the growth of particle size induced by the contact load can probably imply the occurrence of friction reduction at the corresponding pressure.

5.2.2 XPS analysis

In chapter 4, the lower friction was obtained for a-C:H self-mated tribo-pair when fully formulated lubricant is used. The quantification and the high resolution spectra of XPS showed that the quantity of calcium was the most significant element in the tribofilm. The quantity of calcium carbonate was found to be higher at 1.0GPa than at 0.5GPa. This finding is consistent with the chapter 3. For the steel self-mated and a-C:H/steel mixed tribo-pairs, XPS does not show any variation in the amount of calcium. The friction reduction is not obtained either.

In this chapter, the friction reduction is observed for each of the tribo-pair. Based on the findings of the previous chapters, an increase of the calcium quantity at higher pressure is expected. The fitting strategy of C 1s and Ca2p spectra is the same that in the chapters 3 and 4. Two spectra are presented to investigate the chemical structure of the calcium and to compare with chapter 3 and chapter 4. The FWHM, binding energy and corresponding chemical species assignment of C 1s and Fe 2p3/2 are listed in **Tab. A4**.

5.2.2.1 steel/steel

The XPS quantification results of steel/steel tribo-pair are shown in Tab. 5.2. Only C, O, Ca and Fe are observed on the surfaces because the lubricant is made by blending detergent additive with pure base oil. The base oil is composed by C and O, while detergent additive is composed by C, O and Ca.

Tab. 5.2 The XPS quantification results of the steel/steel tribo-pair

Samples		Contact pressure	Atomic concentration			
			C	O	Ca	Fe
Steel/steel	steel ball	0.5GPa	51.1	37.7	**7.2**	4.0
		1.0GPa	51.5	36.9	**10.2**	1.5
	steel disk	0.5GPa	61.2	28.9	***7.0***	2.9
		1.0GPa	51.7	36.8	***10.9***	0.6

For the steel/steel tribo-pair, the concentration growth of the calcium element is observed on both steel ball and steel disk (marked in green). The calcium increases for almost 30% at 1.0GPa. The O/Ca ratio is closer to 3 at 1.0GPa than at 0.5GPa. This suggests that the calcium carbonate is more dominant in the tribofilm at very extreme high pressure.

The XPS high resolution spectra on the steel ball and the steel disk are shown in Fig. 5.13 (a) and (b), respectively.

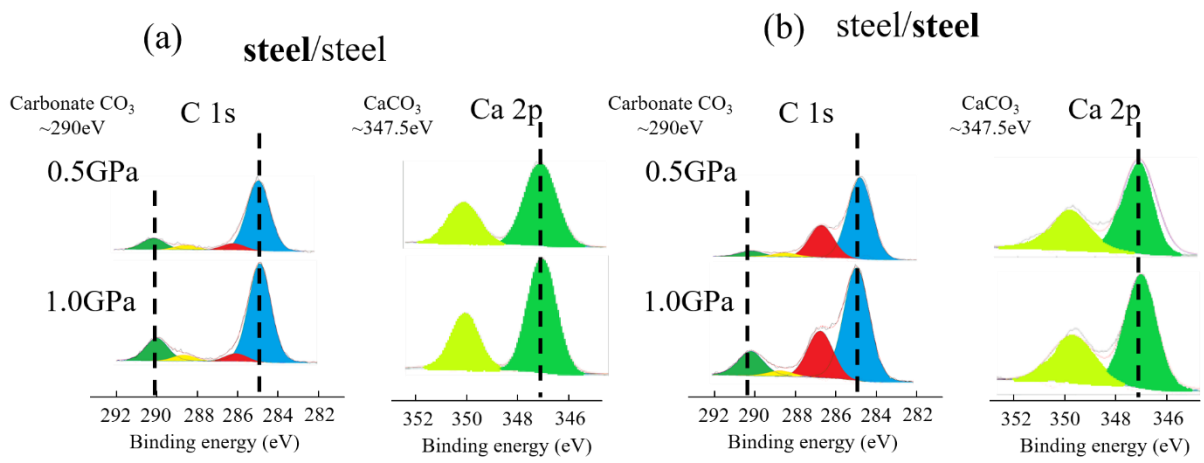

Fig. 5.13 XPS high resolution spectra of C 1s and Ca 2p on the steel ball (a) and on the steel disk (b) from the steel/steel contact

For the C1s photo-peak, the contribution located at 284.8eV, 286.1eV, 288.4eV and 290.0eV can be assigned as C-C (calibration), C-O, C=O and carbonate, respectively. For Ca2p photo-peak, one doublet located at around 347.5eV is found. Therefore, it can be confirmed that the calcium element remains in the form of calcium carbonate.

5.2.2.2 a-C:H/steel

The XPS quantification results of steel/steel tribo-pair are shown in Tab. 5.3.

Tab. 5.3 The XPS quantification results of the a-C:H/steel tribo-pair

Samples		Contact pressure	Atomic concentration			
			C	O	Ca	Fe
a-C:H/steel	a-C:H ball	0.5GPa	92.8	6.1	1.8	/
		1.0GPa	74.3	19.6	6.1	/
	steel disk	0.5GPa	70.6	22.5	5.3	1.6
		1.0GPa	70.3	22.6	7.3	0.1

The quantity of calcium increases for 200% (marked in green) on a-C:H coated ball in a-C:H/steel mixed contact. In contrast, the quantity increases for only 30% on the counterpart. Similarly, the O/Ca ratio is closer to 3 at 1.0GPa. On the other hand, the iron element is not detected on the a-

C:H coated ball. This implies that the materials transfer from the steel disk to a-C:H ball did not happen in this case.

The XPS high resolution spectra on the a-C:H ball and the steel disk are shown in Fig. 5.14 (a) and (b), respectively.

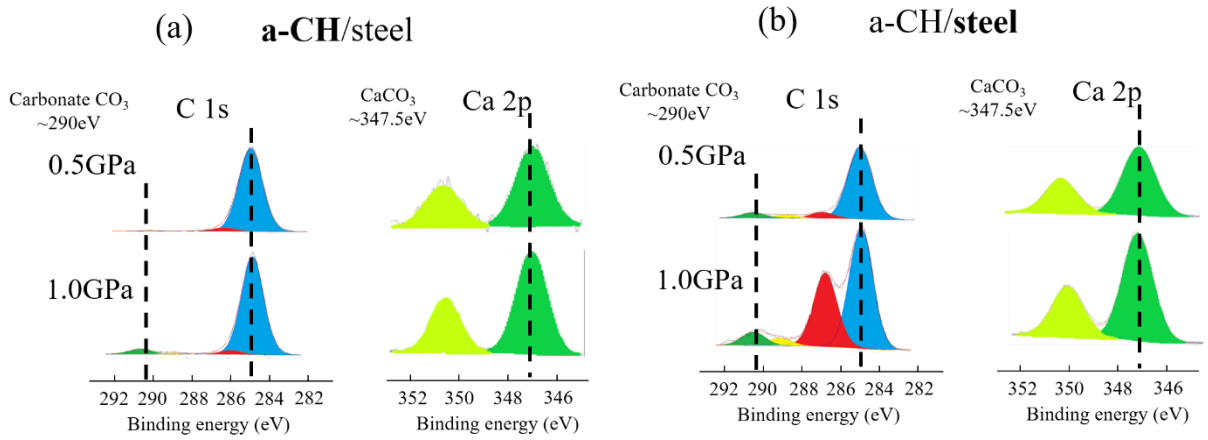

Fig. 5.14 XPS high resolution spectra of C 1s and Ca 2p on the a-C:H ball (a) and on the steel disk (b) from the a-C:H/steel contact

Similarly with the steel/steel contact, for the C1s photo-peak, the contribution located at 284.8eV, 286.2eV, 288.2eV and 290.1eV can be assigned as C-C (calibration), C-O, C=O and carbonate, respectively. It should be noted that the intensity of the carbonate contribution is very low at 0.5GPa on the a-C:H ball. This is consistent with the very low concentration of calcium element shown in Tab. 5.3. For Ca2p photo-peak, one doublet located at around 347.5eV is found. Therefore, it can be confirmed that the calcium element remains in the form of calcium carbonate in the a-C:H/steel tribo-pair.

5.2.2.3 a-C:H/a-C:H

The XPS quantification results of a-C:H self-mated tribo-pair are shown in Tab. 5.4.

Tab. 5.4 The XPS quantification results of the a-C:H/a-C:H tribo-pair

Tribo-pair		Contact pressure	Atomic concentration		
			C	O	Ca
a-C:H/ a-C:H	a-C:H ball	0.5GPa	81.7	14.8	3.6
		1.0GPa	65.6	27.6	7.1
	a-C:H disk	0.5GPa	83.4	13.3	3.3
		1.0GPa	60.5	30.0	9.5

For a-C:H self-mated contact, the calcium quantity increases for about 200% on the a-C:H disk, while the quantity increases for 100% on the counterpart. The XPS high resolution spectra in Fig. 5.15 confirm that the calcium remains in the form of the calcium carbonate.

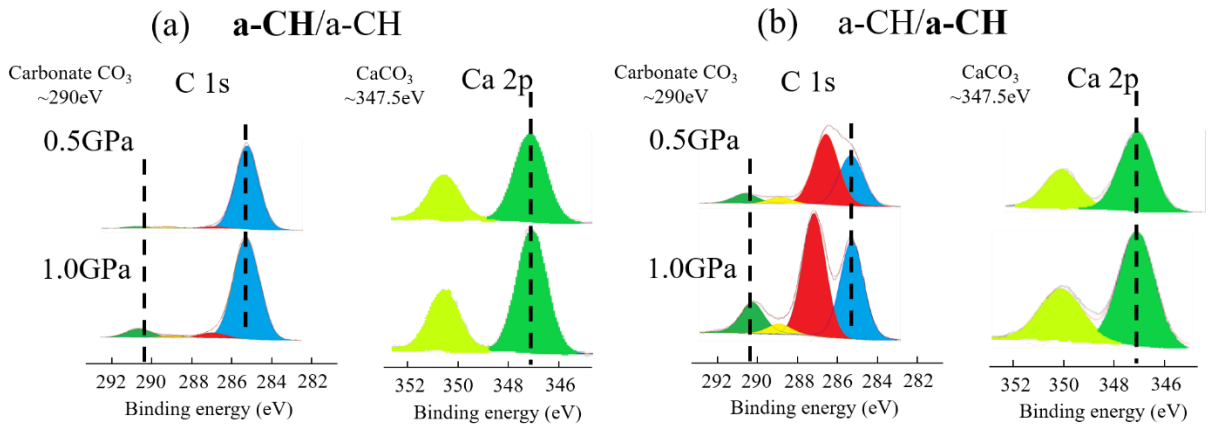

Fig. 5.15 XPS high resolution spectra of C 1s and Ca 2p on the a-C:H ball (a) and on the a-C:H disk (b) from the a-C:H self-mated contact

Therefore, the raise of the calcium quantity is observed on all the surfaces of each tribo-pair. This is consistent with the prediction of which the friction reduction at high contact load is accompanied

with the raise of the calcium carbonate concentration. On the other hand, it is also noteworthy that the iron quantity decreases on all steel surfaces as the function of pressure. This may be due to the fact that iron element from the substrate is less detected, or that less quantity of the iron element is found in the tribofilm. This suggests the formation of a compact or a better anti-wear property calcium carbonate rich tribofilm at high pressure.

5.2.3 TEM/FIB analysis

In chapter 3 and chapter 4, using the fully formulated lubricant, the crystallization of calcium carbonate and the formation of the calcite were confirmed by FIB/TEM for the tribo-contacts (steel/a-C:H chapter 3, a-C:H/a-C:H chapter 4), in which the friction decreases as the function of the pressure. The increase of the calcium carbonate amount was also observed for these tribo-contacts. For the other tribo-pairs, the calcite polymorph was not found in the tribofilm. The quantity growth of calcium carbonate on the surfaces was not significant.

In this chapter, the base oil lubricant blended with 1wt% of detergent additive is used as lubricant on the tribo-contacts used in chapter 4. The friction reduction when the pressure increases is found for all the tribo-pairs, steel/steel, a-C:H/steel and a-C:H/a-C:H. Therefore, FIB cuts were prepared on the disks of a-C:H and the steel self-mated contacts after sliding tests at 0.5GPa and 1.0GPa.

Fig. 5.16 shows the TEM images of the FIB cuts at different scales for the a-C:H disk at 0.5GPa (a1, a2, a3), 1.0GPa (b1, b2, b3) and for the steel disk at 0.5GPa (c1, c2, c3) and 1.0GPa (d1, d2, d3).

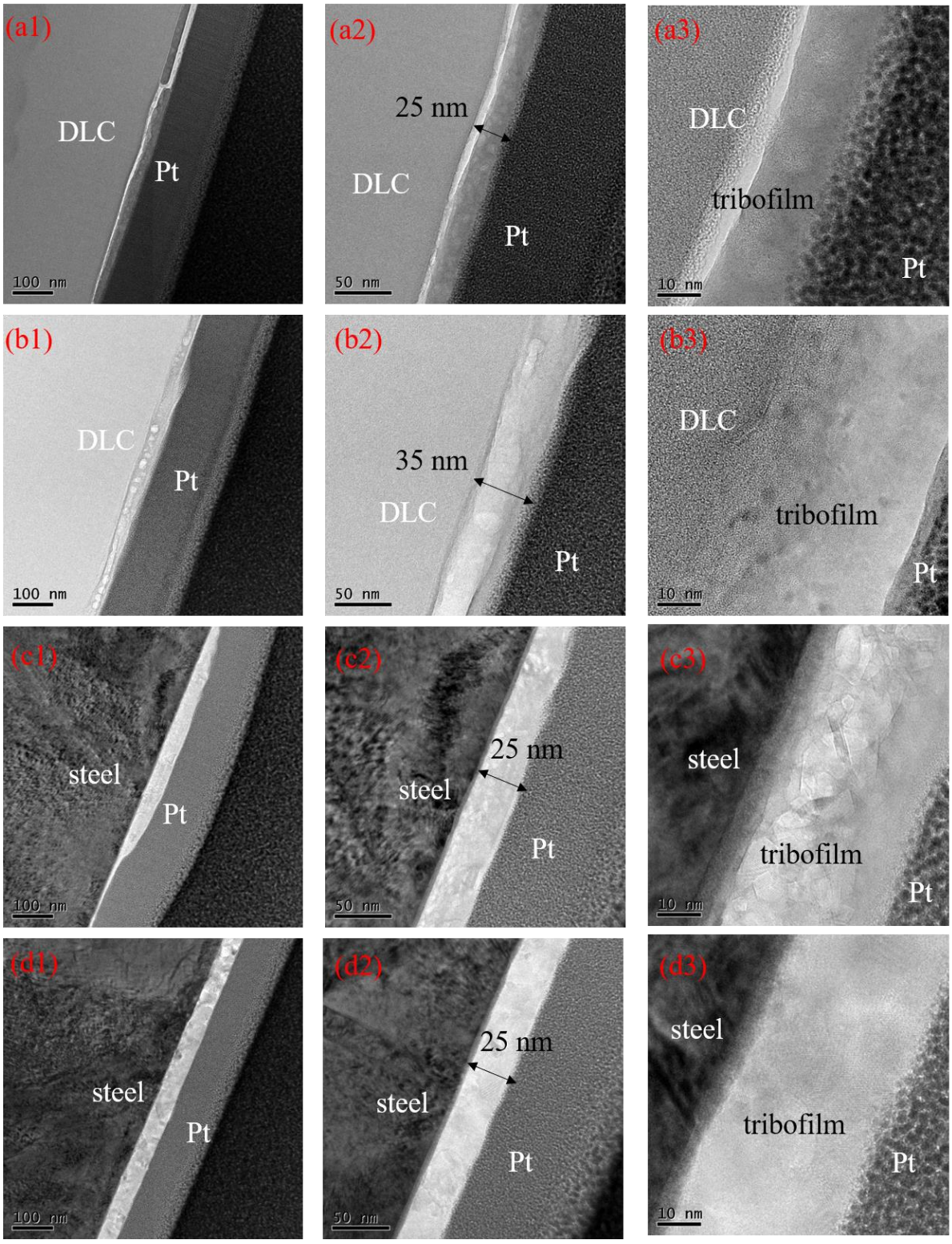

Fig. 5.16 TEM/FIB images at different scales of a-C:H self-mated contact at 0.5GPa (a1, a2, a3), at 1.0GPa (b1, b2, b3) and of steel self-mated contact at 0.5GPa (c1, c2, c3), at 1.0GPa (d1, d2, d3).

For the a-C:H self-mated contact, the holes can be seen in the tribofilm obtained at 0.5GPa (long white parts in a1, a2, a3). The formation of these holes can be due to the milling process during the FIB cut preparation. The different contact pressure does not induce a significant difference on the thickness of the tribofilm, which is always around 30nm. This is not consistent with the AFM results (Fig.5.12 a2 & b2). As explained in chapter 4, this inconsistency can probably due to the fact that AFM is not a very reliable technique to measure the tribofilm thickness. Moreover, the selected areas for AFM and FIB/TEM are not exactly the same. Even though the analyzed area was carefully chosen (always in the center of the tribofilm), it is likely that in some specific areas, the tribofilm thickness can be significantly different. The interlayer between the tribofilm and a-C:H coating is relatively regular. At 1.0GPa, it seems like that the tribofilm is less homogeneous than that of 0.5GPa. The crystal plane crystal structure can be found in the heterogenous zone. The higher magnification images will be shown in the following texts.

For steel self-mated contact, the tribofilm is more homogenous at 1.0GPa. The thickness of tribofilm remains at about 25nm for both 0.5GPa and 1.0GPa. This is consistent with the AFM results (Fig. 5.8 a2, b2). The interlayer of the tribofilm and the steel substrate is relatively regular. The crystal plane structures can be observed in Fig. 5.16 (d3), and they will be identified in the following text.

Tab. 5.5 shows the EDS quantification results of the characteristic elements present in the tribofilm (obtained from the cross-section). It should be noted that the absolute quantity obtained by EDS is not reliable. It is the ratio between the elements that should be investigated. Therefore, it would be interesting to calculate the ratio between for example, O and Ca, ratio that is supposed to be close to 3 ($CaCO_3$). The calculation with carbon is risky considering the fact that carbon can be related

to many structures in the tribofilm. The chemical bond of carbon is even more complex and less predictable than oxygen.

Tab. 5.5 EDS quantification on FIB cross-section.

Elements	Atomic Concentration			
	a-C:H disk		steel disk	
	0.5GPa	1.0GPa	0.5GPa	1.0GPa
C	86.8	46.3	22.7	25.6
O	10.0	40.6	50.6	59.3
Ca	3.2	13.2	12.6	18.4
Fe	/	/	2.0	1.1

For a-C:H disk, the ratio between O and Ca is very close to 3, which are 3.13 and 3.08 at 0.5GPa and 1.0GPa, respectively. Interestingly, the quantity of calcium carbonate also increases as the function of the contact load. This is consistent with the findings of XPS.

For steel disk, the ratio between O and Ca is 4.02 at 0.5GPa and 3.22 at 1.0GPa. The ratio is little higher than 3 and can possibly be explained by the presence of iron oxide. More importantly, at higher pressure, the ratio between O and Ca is closer to 3. The ratio between carbon and calcium is closer to 1 comparing with the a-C:H self-mated tribo-pair. Nevertheless, it is risky to have the further discussion on the calcium quantity.

The presence of Ca and O is confirmed by the EDS mapping results in Fig. 5.17. The contrast of the oxygen element is not significant for (b1) and (b2) due to the relatively high oxygen content in the steel substrate.

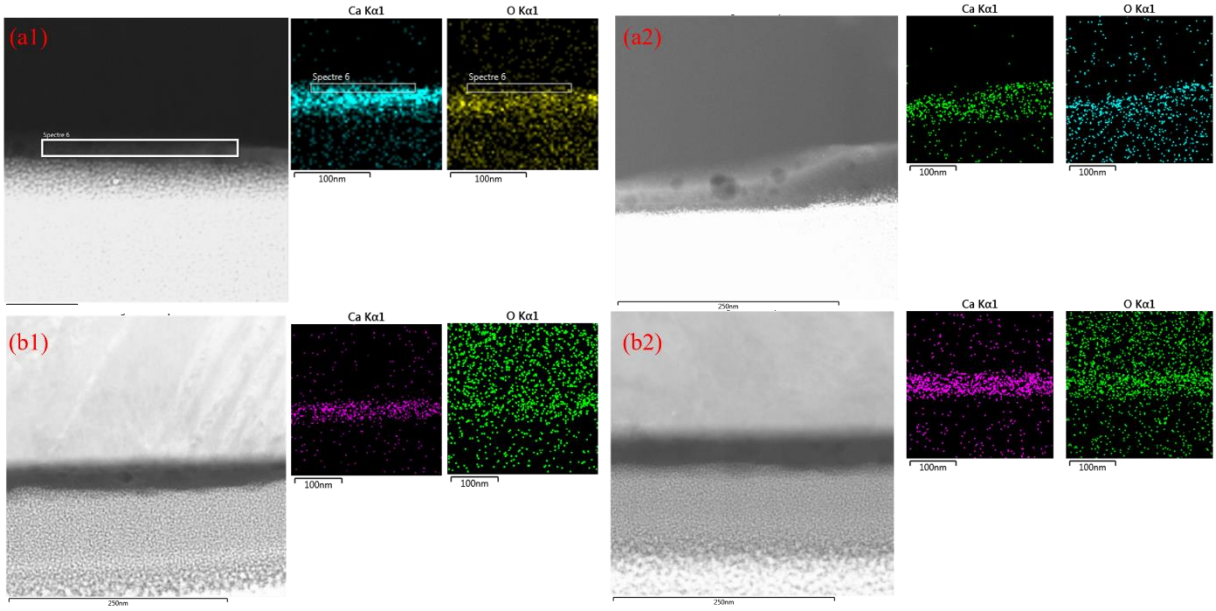

Fig. 5.17 EDS mapping results on the cross-sections of a-C:H self-mated contact at 0.5GPa (a1) and 1.0GPa (a2) and steel self-mated contact at 0.5GPa (b1) and 1.0GPa (b2).

Fig. 5.18 shows the images obtained in diffraction mode performed on the a-C:H disk (a1, a2) and the steel disk (b1, b2) at 0.5GPa and 1.0GPa, respectively. The d-distances were measured by using Gatan GMS 3.

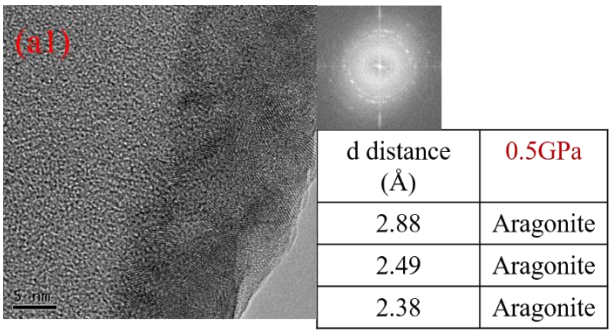

d distance (Å)	0.5GPa
2.88	Aragonite
2.49	Aragonite
2.38	Aragonite

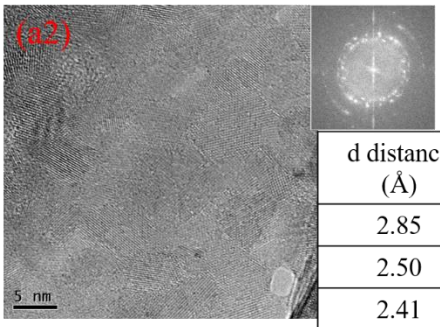

d distance (Å)	1.0GPa
2.85	Calcite
2.50	Calcite
2.41	Aragonite
2.28	Calcite
1.70	Aragonite

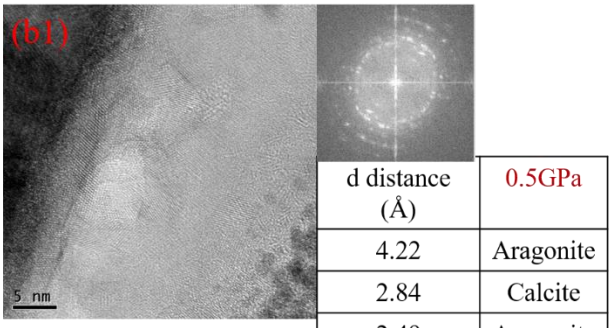

d distance (Å)	0.5GPa
4.22	Aragonite
2.84	Calcite
2.49	Aragonite
2.12	Aragonite
2.08	Fe_2O_3
1.71	Aragonite

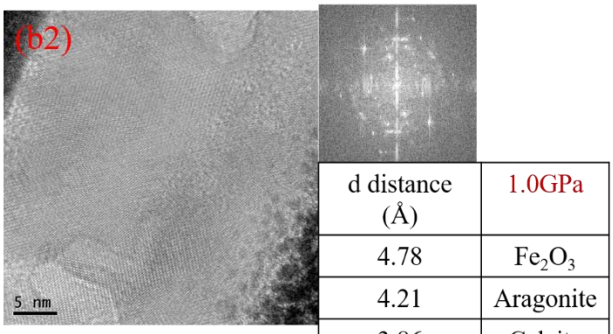

d distance (Å)	1.0GPa
4.78	Fe_2O_3
4.21	Aragonite
3.86	Calcite
2.84	Calcite
2.47	Calcite
2.09	Calcite
1.99	Fe_2O_3
1.96	Aragonite

Fig. 5.18 TEM diffraction mode on cross-sections and d-distance measurements at a-C:H disk at 0.5GPa (a1) and 1.0GPa (a2), and steel disk at 0.5GPa (b1) and 1.0GPa (b2) [7, 8].

At 0.5GPa (Fig. 5.18 a1, b1), aragonite can be found in the tribofilm of both a-C:H and steel disk. However, when fully formulated lubricant is used, the crystal structure is either hardly to be observed or mainly in the form of vaterite. At 1.0GPa (Fig. 5.18 a2, b2), both calcite and aragonite crystals can be found in the tribofilm. It is also interesting to notice that on the steel disk, the polymorph of calcium carbonate is vaterite at 1.0GPa (Fig. 4.18 b2) when fully formulated lubricant is used. However, the calcite appears in the tribofilm when BoD lubricant is used. It

should be reminded that the friction reduction as the function of pressure was observed for both a-C:H/a-C:H and steel/steel contact when BoD lubricant is used. The calcite crystal is found for both tribo-pairs at 1.0GPa.

5.3 Discussion

In this chapter, the friction reduction is obtained for each tribo-pair (steel/steel, a-C:H/steel, a-C:H/a-C:H) by blending 1wt% of detergent additive (used in the fully formulated lubricant) with the corresponding base oil. The role of the detergent additive in the friction reduction was confirmed. However, any synergistic effects in friction reduction between detergent additive and ZDDP-like additive can be excluded in this work.

Comparing with chapters 3 and 4, one of the common points of this chapter is that the friction reduction looks always related to the crystallization and the transformation of the crystal allotrope of calcium carbonate at higher contact pressure. Comparing with chapter 4, the friction at 0.5GPa is slightly lower with BoD lubricant for all the tribo-pairs. This can probably be explained by the aragonite crystal observed at 0.5GPa for steel/steel and a-C:H/a-C:H contact when BoD is used. In contrast, the tribofilm is mainly composed of crystal vaterite (steel/steel) and amorphous calcium carbonate (a-C:H/a-C:H) when the fully formulated lubricant is used. This suggests that aragonite is sable to provide the lower friction than vaterite and amorphous calcium carbonate during the friction. At 1.0GPa, the calcite appears in the tribofilm when BoD is used as the lubricant. This is consistent with the findings of the chapters 3 and 4, in which the friction reduction is induced by the formation of aragonite and calcite.

Concerning the tribo-catalytic effect, it seems like that the findings in this chapter can challenge the assumption proposed in chapter 3 as the friction reduction and calcite crystal are also found in

steel self-mated contact. A more detailed assumption on this catalytic-effect should be proposed: in chapters 3 and 4, the friction reduction as the function of pressure is observed when a-C:H coating is involved in the contact and for a-C:H self-mated contact. The presence of ZDDP-like anti-wear additive certainly influences the composition of the tribofilm. Combining the results of this chapter, we assume that the ZDDP-like anti-wear additive increases the "energy barrier" to achieve the transformation of calcium carbonate allotrope, notably for the steel/steel tribo-pair in chapters 3 and 4. Comparing with the a-C:H DLC, it is well-known that ZDDP forms on the steel surfaces a thicker tribofilm containing longer polyphosphate chain [3-6].

However, this is not to say that a-C:H DLC can be replaced by any other types of materials that are not preferable for the formation of ZDDP tribofilm. It should be further investigated by replacing a-C:H DLC by other types of DLC coatings, such as ta-C, a-C, etc. From another point of view, the FIB cuts can be performed on the tribofilm after different cycles of sliding tests for each tribo-pair. By observing the appearance of calcite after certain sliding cycles, the different tribo-catalytic potential of steel, a-C:H or other DLC coatings on calcium carbonate crystal transformation can be studied.

In this chapter, in the absence of ZDDP-like anti-wear additive in the lubricant, the "energy barrier" of the calcium carbonate crystal transformation is not increased. Therefore, the crystal transformation is much less dependent on the materials. This is why the friction reduction can be obtained for each tribo-pair. For the energies required to overcome crystallographic transition barriers in presence of different materials, further research is needed.

5.4 Conclusions

This chapter investigated the role of the detergent additive in the friction reduction as the function of pressure in boundary lubrication regime by employing ball-on-disk configuration. The lubricant was made by blending base oil with 1wt% of detergent additive used in the fully formulated lubricant. The selected tribo-pairs are the same than in chapter 4.

In this section, the friction reduction as the function of pressure is observed for each tribo-pair. By coupling multiple surface analysis techniques, the increase of calcium carbonate amount on both ball (steel, a-C:H) and disk (steel, a-C:H) is confirmed for each tribo-pair. At 0.5GPa, the calcium carbonate already crystallizes in aragonite. This is different compared to the results obtained in chapter 4 (vaterite and amorph). At 1.0GPa, the tribofilm is mainly composed of calcite for both steel and a-C:H self-mated contact. An “energy barrier” effect brought by ZDDP-like anti-wear additive in fully formulated lubricant is proposed. The tribo-catalytic effect still holds but it needs further investigation to confirm the role of a-C:H DLC coating in crystal transformation. Interestingly, the irreplaceable role of the detergent additive is confirmed again. This remains consistent throughout this PhD thesis.

References

[1] Lubricant additives - A practical guide. (2018, March 6). Machinery Lubrication. https://www.machinerylubrication.com/Read/31107/oil-lubricant-additives

[2] Burrington, J. D., Pudelski, J. K., & Roski, J. P. (n.d.). Challenges in detergents and dispersants for engine oils. Practical Advances in Petroleum Processing, 579-595. https://doi.org/10.1007/978-0-387-25789-1_18

[3] Spikes, H. (2004). The history and mechanisms of ZDDP. Tribology Letters, 17(3), 469–489. https://doi.org/10.1023/b:tril.0000044495.26882.b5

[4] Vengudusamy, B., Green, J. H., Lamb, G. D. & Spikes, H. A. (2013). Durability of ZDDP tribofilms formed in DLC/DLC contacts. Tribology Letters, 51(3), 469–478. https://doi.org/10.1007/s11249-013-0185-z

[5] Equey, S., Roos, S., Mueller, U., Hauert, R., Spencer, N. D., & Crockett, R. (2008). Reactions of zinc-free anti-wear additives in DLC/DLC and Steel/steel contacts. Tribology International, 41(11), 1090–1096. https://doi.org/10.1016/j.triboint.2008.03.004

[6] De Barros'Bouchet, M., Martin, J., Le-Mogne, T., & Vacher, B. (2005). Boundary lubrication mechanisms of carbon coatings by MoDTC and ZDDP additives. Tribology International, 38(3), 257-264. https://doi.org/10.1016/j.triboint.2004.08.009

Chapter 6 General conclusions and perspectives

In this chapter, the main findings and conclusions of this study are outlined. Recommendations for future research are provided to further explore specific outcomes that could be enhanced through additional experiments.

6.1 General conclusions

In this work, the influence of the contact pressure on the tribological behaviors of diffferent a-C:H DLC involved tribo-pairs lubricated by a fully formulated engine oil is investigated.

For ring-on-disk configuration, the CoF decreases as the function of the contact load when employing steel/a-C:H contact in boundary/mixed lubrication regime. By combining various analytical techniques, the concentration of calcium carbonate, which is derived from the detergent additive, grows as the function of the contact load. Calcium is the most dominant element in the tribofilm. Moreover, the amorphous calcium carbonate (in as-received detergent) crystallizes during the friction tests. The allotrope of calcium carbonate was found to be load-dependent. The calcium carbonate structure was found to be vaterite, aragonite and calcite at respectively low, medium and high contact load. The more and more 2D-lamella like structure as function of the pressure is believed to result in the lower CoF. However, the calcium is no longer the most dominant element in the tribofilm for steel/steel contact. The allotrope of calcium carbonate present in the tribofilm of steel/steel tribo-pair remains vaterite even at high contact load. The CoF of steel/steel increases as the function of the pressure. The calcite crystal is found for a-C:H self-mated tribo-pair at high contact load. However, XPS analysis shows that the calcium carbonate probably decomposes during the friction in this case. Therefore, the CoF of a-C:H/a-C:H exhibits a trend of initially decreasing followed by an increase.

The simpler and more standard ball-on-disk configuration was employed to have a deeper understanding of the effect of the contact pressure on the friction reduction observed for some of the tribo-pairs in the ring-on-disk configuration. The selected tribo-pairs were steel/steel, a-C:H/steel and a-C:H/a-C:H. As using the fully formulated lubricant, the friction reduction was only

obtained in a-C:H self-mated contact. Similarly, the quantity of calcium carbonate was found to increase at high pressure. More importantly, the calcite was also found in the tribofilm after friction tests carried out at high contact load. By contrast, the allotrope structure of calcium carbonate remains in vaterite for steel/steel contact even at high contact pressure.

The identical ball-on-disk tribological tests were performed by blending the base oil (used in the fully formulated lubricant) with 1wt% of detergent additive, in order to verify the role of calcium carbonate in the friction reduction. The results show that the friction reduction as the function of contact load is observed for each of the tribo-pair. An increase of the calcium carbonate amount at high pressure is also obtained. The aragonite crystals are observed in the tribofilm at 0.5GPa, and the calcite is observed at 1.0GPa for both steel and a-C:H self-mated contact.

Throughout the study, it was shown that the CoF can be controlled by applying the required contact pressure to obtain the different allotrope structure of calcium carbonate in the tribofilm. Moreover, we propose that the a-C:H DLC may have a tribo-catalytic effect, thus helping in the crystallization of the amorphous calcium carbonate into several polymorphs during the friction. The “energy barrier” to obtain the different calcium carbonate polymorphs is supposed to be different. Comparing with the model lubricant (base oil + 1wt% of detergent), when the fully formulated oil is used (ZDDP-like anti-wear additive is present), the “energy barrier” to obtain the calcite is supposed to be higher.

6.2 Perspectives

1. Performing the friction tests at the same conditions with base oil blending with detergent additive for ring-on-disk configuration. This is to verify the detergent role in friction reduction for ring-on-disk contact.

2. Perform the simulation on the impact of materials nature on calcium carbonate crystallization and transformation.

3. Perform the surface analyses (XPS, FIB/TEM) after different sliding cycles for ball-on-disk configuration when using base oil blending with detergent additive. This is to study if the formation of calcite is faster for a-C:H self-mated contact, thus to partially justify its tribo-catalytic effects.

4. Investigating the impact of different types of DLC coatings (ta-Cs, a-C, etc.) on tribological performances and calcium carbonate crystal transformation at high contact load.

5. Conducting the friction tests at room temperature to investigate if the formation of calcite is temperature-dependent.

Appendix

Not polished steel ring in steel/a-C:H

Raw

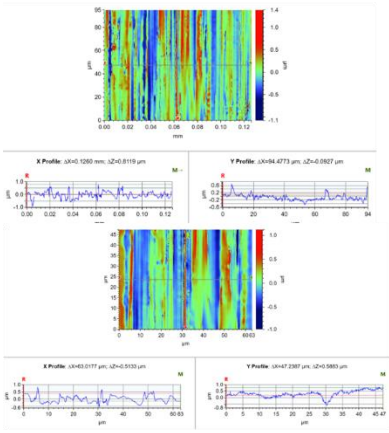

Analytical Result		
Label	Value	Units
Sa	0.201	µm
Sku	2.894	
Sp	1.115	µm
Sq	0.246	µm
Ssk	0.367	
Sv	-0.965	µm
Sz	2.08	µm

Analytical Result		
Label	Value	Units
Sa	0.202	µm
Sku	3.332	
Sp	1.386	µm
Sq	0.257	µm
Ssk	0.001	
Sv	-1.079	µm
Sz	2.466	µm

320MPa

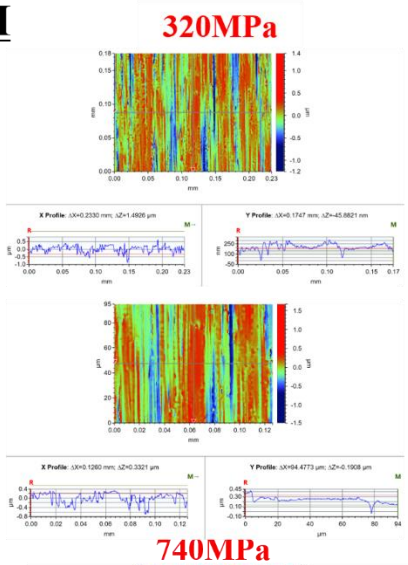

Analytical Result		
Label	Value	Units
Sa	0.178	µm
Sku	3.653	
Sp	1.383	µm
Sq	0.225	µm
Ssk	-0.853	
Sv	-1.242	µm
Sz	2.624	µm

Analytical Result		
Label	Value	Units
Sa	0.183	µm
Sku	3.228	
Sp	1.672	µm
Sq	0.225	µm
Ssk	-0.704	
Sv	-1.475	µm
Sz	3.147	µm

500MPa

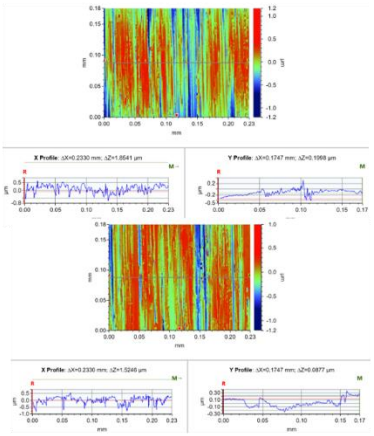

Analytical Result		
Label	Value	Units
Sa	0.196	µm
Sku	3.105	
Sp	1.167	µm
Sq	0.243	µm
Ssk	-0.586	
Sv	-1.201	µm
Sz	2.368	µm

Analytical Result		
Label	Value	Units
Sa	0.189	µm
Sku	3.659	
Sp	0.98	µm
Sq	0.24	µm
Ssk	-0.937	
Sv	-1.203	µm
Sz	2.183	µm

740MPa

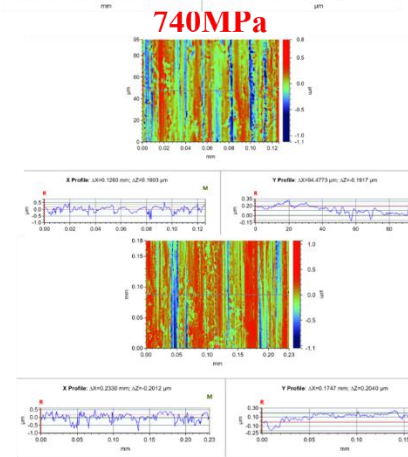

Analytical Result		
Label	Value	Units
Sa	0.158	µm
Sku	3.576	
Sp	0.85	µm
Sq	0.201	µm
Ssk	-0.782	
Sv	-1.126	µm
Sz	1.976	µm

Analytical Result		
Label	Value	Units
Sa	0.191	µm
Sku	3.555	
Sp	1.067	µm
Sq	0.243	µm
Ssk	-0.848	
Sv	-1.053	µm
Sz	2.12	µm

1GPa

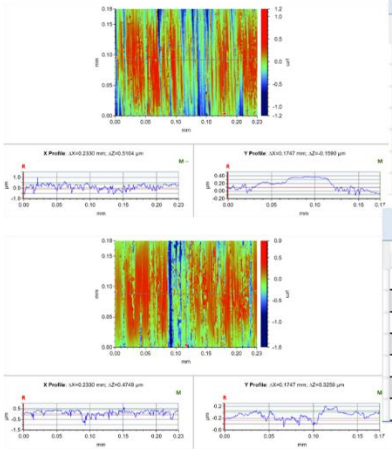

Analytical Result		
Label	Value	Units
Sa	0.196	µm
Sku	3.105	
Sp	1.167	µm
Sq	0.243	µm
Ssk	-0.586	
Sv	-1.201	µm
Sz	2.368	µm

Analytical Result		
Label	Value	Units
Sa	0.188	µm
Sku	4.85	
Sp	0.897	µm
Sq	0.247	µm
Ssk	-1.133	
Sv	-1.597	µm
Sz	2.495	µm

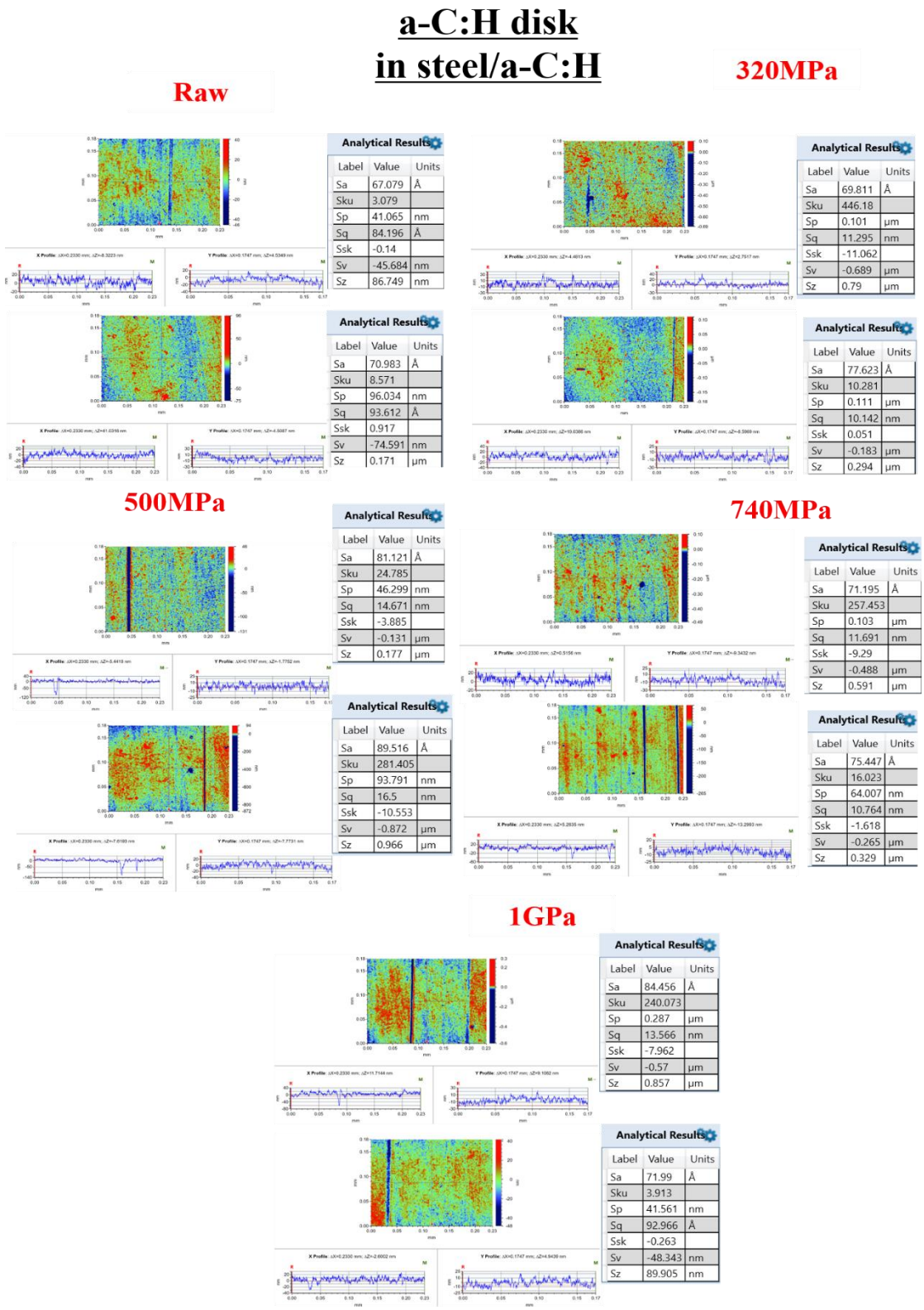

Fig. A1 The surface roughness of not polished steel ring and a-C:H disk in steel/a-C:H tribo-pair after friction tests.

Tab. A1 (X represents elements of C, P, S, Ca, Fe, Zn).

Materials	Contact pressure	Element	Assignment of species	Binding energy (eV)	Full-width-half-maximum (FWHM)
Not polished steel ring	No friction	C 1s	Carbide	282.97	0.87
			C-C/C-H	284.93	1.53
			C-O	286.43	1.53
			C=O	288.55	1.53
		O 1s	Metallic oxide	529.79	1.14
			X = O	531.07	2.13
			X-O	532.63	2.13
		Fe 2p3/2	Fe (0)	706.28	1.06
			Fe (II)	708.00	2.59
			Fe (III)	709.84	2.59
			FeOOH	711.95	2.59
			Fe (II) satellite peak	714.81	2.59
	320MPa (400N)	C 1s	C-C/C-H	284.83	1.35
			C-O	286.06	1.35
			C=O	288.60	1.35
			$-CO_3$	289.85	1.35
		O 1s	Metallic oxide	529.68	1.13
			X = O	531.33	2.02
			X-O	533.11	2.02
		Fe 2p3/2	Fe (0)	706.16	1.12
			Fe (II)	708.28	2.53
			Fe (III)	710.09	2.53
			FeOOH	712.39	2.53
			Fe (II) satellite peak	714.93	2.53
		Ca 2p3/2	Calcium carbonate	347.39	1.68
		P 2p3/2	Phosphate	133.30	1.51
		S 2p3/2	Zn-S/Fe-S	161.56	1.27
			Sulphate	168.28	1.95
		Zn 2p3/2	Zn-S/ZnO	1021.69	1.59
	500MPa (950N)	C 1s	C-C/C-H	284.75	1.50
			C-O	286.34	1.50
			C=O	288.43	1.50
			$-CO_3$	289.92	1.50
		O 1s	Metallic oxide	529.72	1.19
			X = O	531.46	1.74
			X - O	532.82	1.74
		Fe 2p3/2	Fe (II)	708.52	2.46
			Fe (III)	710.35	2.46
			FeOOH	712.45	2.46
			Fe (II) satellite peak	714.84	2.46

		Ca 2p3/2	Calcium carbonate	347.47	1.59
		P 2p3/2	Phosphate	133.20	1.46
		S 2p3/2	Zn-S/Fe-S	161.17	1.21
			Sulphate	168.21	1.92
		Zn 2p3/2	Zn-S/ZnO	1021.74	1.61
	740MPa (2100N)	C 1s	C-C/C-H	284.75	1.66
			C-O	286.36	1.66
			C=O	288.14	1.66
			-CO_3	290.04	1.66
		O 1s	Metallic oxide	529.98	1.32
			X = O	531.69	1.74
			X - O	533.08	1.74
		Fe 2p3/2	Fe (II)	708.75	2.63
			Fe (III)	710.65	2.63
			FeOOH	712.55	2.63
			Fe (II) satellite peak	714.72	2.63
		Ca 2p3/2	Calcium carbonate	347.55	1.76
		P 2p3/2	Phosphate	133.54	1.64
		S 2p3/2	Zn-S/Fe-S	161.83	1.47
			Sulphate	168.85	1.76
		Zn 2p3/2	Zn-S/ZnO	1021.85	1.70
	1GPa (3800N)	C 1s	C-C/C-H	284.85	1.69
			C-O	286.69	1.69
			C=O	287.88	1.69
			-CO_3	290.10	1.69
		O 1s	X = O	531.49	1.79
			X - O	532.86	1.79
		Fe 2p3/2	Signal is too low to be well fitted	/	
		Ca 2p3/2	Calcium carbonate	347.53	1.69
		P 2p3/2	Phosphate	133.33	1.64
		S 2p3/2	Zn-S/Fe-S	161.77	1.41
		Zn 2p3/2	Zn-S/ZnO	1022.01	1.63
a-C:H DLC coated disk	Out of the wear track	C 1s	DLC substrate	284.26	1.45
			C-C/C-H	285.06	1.45
			C-O	286.55	1.45
			C=O	288.74	1.45
		O 1s	X - O	532.61	1.98
		Ca 2p	Calcium phosphate	348.71	1.86
		P 2p	Phosphate	133.46	1.52
		S 2p	Zn-S	162.24	1.47
			S-C	163.88	1.47
			Sulphate	168.76	1.92
		Zn 2p3/2	Zn-S/ZnO	1022.47	1.73

	320MPa (400N)	C 1s	DLC substrate	284.05	1.55
			C-C/C-H	284.85	1.55
			C-O	285.91	1.55
			C=O	287.11	1.55
			$-CO_3$	289.20	1.55
		O 1s	X = O	531.77	1.92
			X - O	533.18	1.92
		Ca 2p	Calcium carbonate	347.68	1.64
		P 2p	Phosphate	133.41	1.47
		S 2p	Zn-S	161.85	1.59
			S-C	163.41	1.59
			Sulphate	168.56	1.94
		Zn 2p3/2	Zn-S/ZnO	1022.15	1.63
	500MPa (950N)	C 1s	DLC substrate	284.20	1.53
			C-C/C-H	285.10	1.53
			C-O	286.10	1.53
			C=O	287.00	1.53
			$-CO_3$	289.60	1.53
		O 1s	X = O	531.93	1.81
			X - O	533.23	1.81
		Ca 2p	Calcium carbonate	347.86	1.58
		P 2p	Phosphate	133.57	1.42
		S 2p	Zn-S	161.99	1.52
			S-C	163.56	1.52
			Sulphate	168.53	1.97
		Zn 2p3/2	Zn-S/ZnO	1022.32	1.79
	740MPa (2100N)	C 1s	DLC substrate	284.18	1.56
			C-C/C-H	285.01	1.56
			C-O	286.98	1.56
			C=O	286.97	1.56
			$-CO_3$	289.40	1.56
		O 1s	X = O	532.01	1.83
			X - O	533.63	1.83
		Ca 2p	Calcium carbonate	347.82	1.64
		P 2p	Phosphate	133.52	1.43
		S 2p	Zn-S	161.55	1.59
			S-C	163.59	1.59
			Sulphate	168.76	1.87
		Zn 2p3/2	Zn-S/ZnO	1022.45	1.86
	1.0GPa (3800N)	C 1s	C-C/C-H	284.80	1.31
			C-O	285.76	1.31
			C=O	287.45	1.31
			$-CO_3$	289.22	1.31
		O 1s	X = O	532.13	1.87
			X - O	533.75	1.87

		Ca 2p	Calcium carbonate	347.78	1.54
		P 2p	Phosphate	133.71	1.55
		S 2p	Zn-S	162.03	1.75
			S-C	163.53	1.67
			Sulphate	169.88	2.21
		Zn 2p3/2	Zn-S/ZnO	1022.61	1.57

a-C:H ring
in a-C:H/a-C:H

320MPa

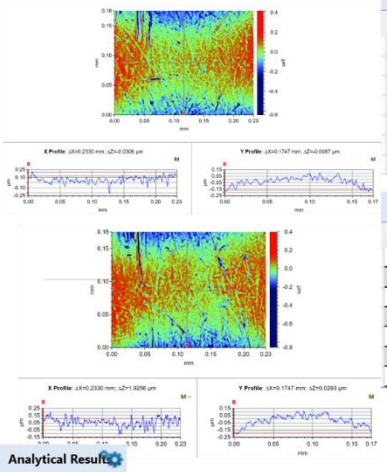

Analytical Results

Label	Value	Units
Sa	67.28	nm
Sku	4.363	
Sp	0.416	µm
Sq	85.213	nm
Ssk	-0.612	
Sv	-0.639	µm
Sz	1.054	µm

Analytical Results

Label	Value	Units
Sa	63.048	nm
Sku	5.132	
Sp	0.397	µm
Sq	80.326	nm
Ssk	-0.75	
Sv	-0.857	µm
Sz	1.253	µm

500MPa

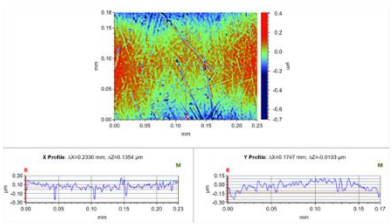

Analytical Results

Label	Value	Units
Sa	65.118	nm
Sku	3.97	
Sp	0.408	µm
Sq	81.247	nm
Ssk	-0.515	
Sv	-0.707	µm
Sz	1.115	µm

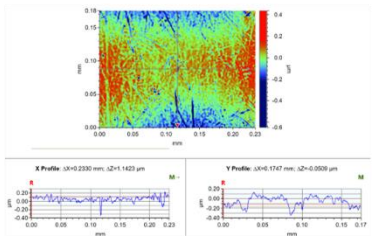

Analytical Results

Label	Value	Units
Sa	60.933	nm
Sku	4.434	
Sp	0.436	µm
Sq	78.318	nm
Ssk	-0.569	
Sv	-0.65	µm
Sz	1.086	µm

740MPa

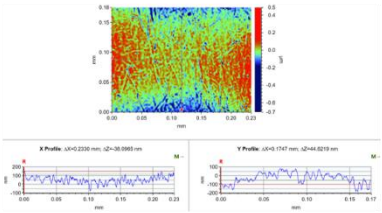

Analytical Results

Label	Value	Units
Sa	51.165	nm
Sku	4.727	
Sp	0.486	µm
Sq	65.626	nm
Ssk	-0.731	
Sv	-0.707	µm
Sz	1.193	µm

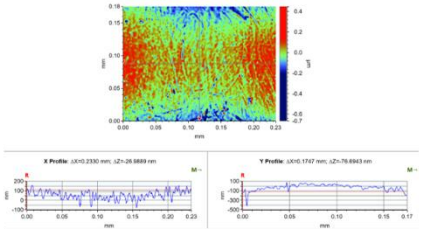

Analytical Results

Label	Value	Units
Sa	53.62	nm
Sku	4.595	
Sp	0.447	µm
Sq	68.159	nm
Ssk	-0.608	
Sv	-0.667	µm
Sz	1.114	µm

a-C:H disk
in a-C:H/a-C:H

320MPa

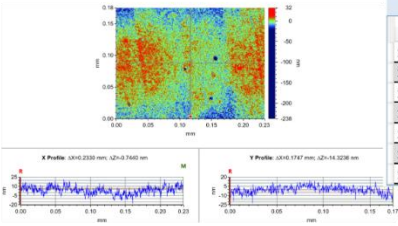

Analytical Results

Label	Value	Units
Sa	57.687	Å
Sku	29.303	
Sp	31.739	nm
Sq	74.654	Å
Ssk	-1.345	
Sv	-0.238	µm
Sz	0.27	µm

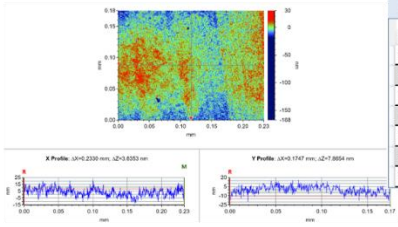

Analytical Results

Label	Value	Units
Sa	56.9	Å
Sku	12.732	
Sp	30.241	nm
Sq	72.551	Å
Ssk	-0.702	
Sv	-0.168	µm
Sz	0.198	µm

500MPa

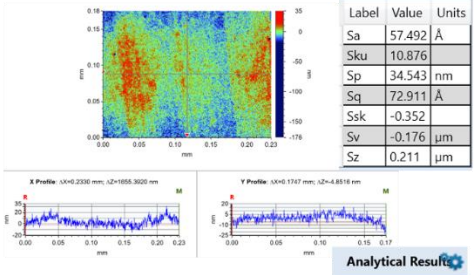

Analytical Results

Label	Value	Units
Sa	57.492	Å
Sku	10.876	
Sp	34.543	nm
Sq	72.911	Å
Ssk	-0.352	
Sv	-0.176	µm
Sz	0.211	µm

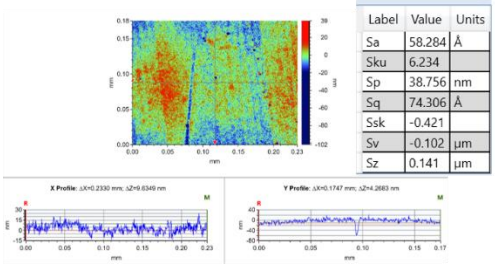

Analytical Results

Label	Value	Units
Sa	58.284	Å
Sku	6.234	
Sp	38.756	nm
Sq	74.306	Å
Ssk	-0.421	
Sv	-0.102	µm
Sz	0.141	µm

740MPa

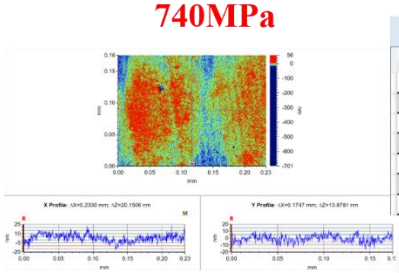

Analytical Results

Label	Value	Units
Sa	56.621	Å
Sku	644.323	
Sp	56.255	nm
Sq	77.54	Å
Ssk	-9.692	
Sv	-0.701	µm
Sz	0.757	µm

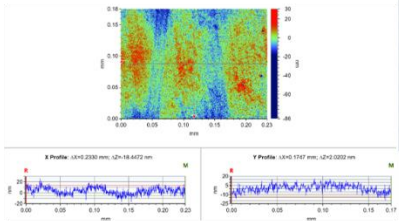

Analytical Results

Label	Value	Units
Sa	55.46	Å
Sku	3.6	
Sp	30.459	nm
Sq	69.541	Å
Ssk	-0.136	
Sv	-85.839	nm
Sz	0.116	µm

steel ring
in steel/steel

320MPa

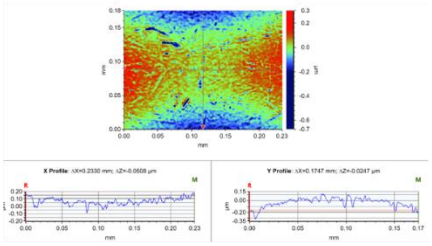

Analytical Results

Label	Value	Units
Sa	60.704	nm
Sku	4.032	
Sp	0.302	µm
Sq	75.562	nm
Ssk	-0.626	
Sv	-0.675	µm
Sz	0.977	µm

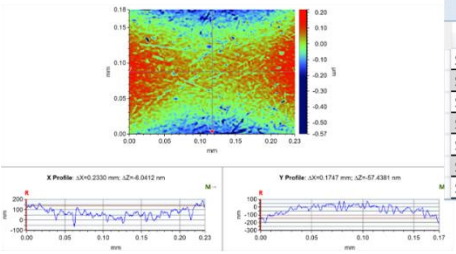

Analytical Results

Label	Value	Units
Sa	55.711	nm
Sku	3.518	
Sp	0.217	µm
Sq	69.929	nm
Ssk	-0.451	
Sv	-0.573	µm
Sz	0.79	µm

500MPa

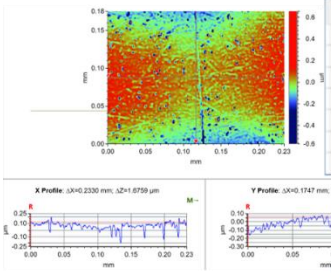

Analytical Results

Label	Value	Units
Sa	64.75	nm
Sku	5.38	
Sp	0.654	µm
Sq	83.52	nm
Ssk	-0.925	
Sv	-0.57	µm
Sz	1.224	µm

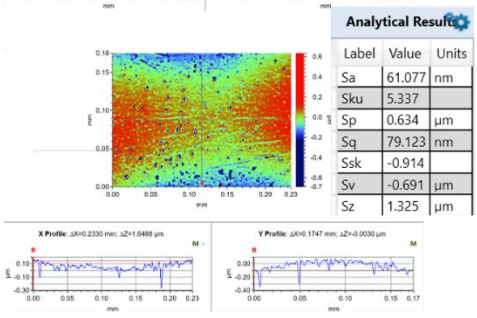

Analytical Results

Label	Value	Units
Sa	61.077	nm
Sku	5.337	
Sp	0.634	µm
Sq	79.123	nm
Ssk	-0.914	
Sv	-0.691	µm
Sz	1.325	µm

740MPa

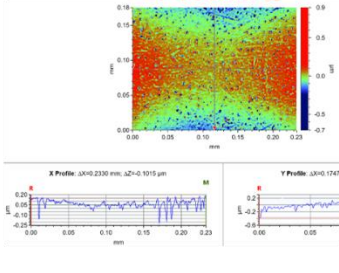

Analytical Results

Label	Value	Units
Sa	64.242	nm
Sku	6.178	
Sp	0.893	µm
Sq	84.399	nm
Ssk	-0.76	
Sv	-0.707	µm
Sz	1.6	µm

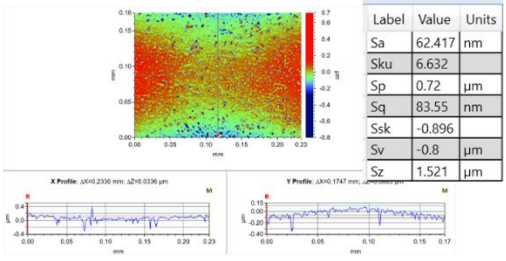

Analytical Results

Label	Value	Units
Sa	62.417	nm
Sku	6.632	
Sp	0.72	µm
Sq	83.55	nm
Ssk	-0.896	
Sv	-0.8	µm
Sz	1.521	µm

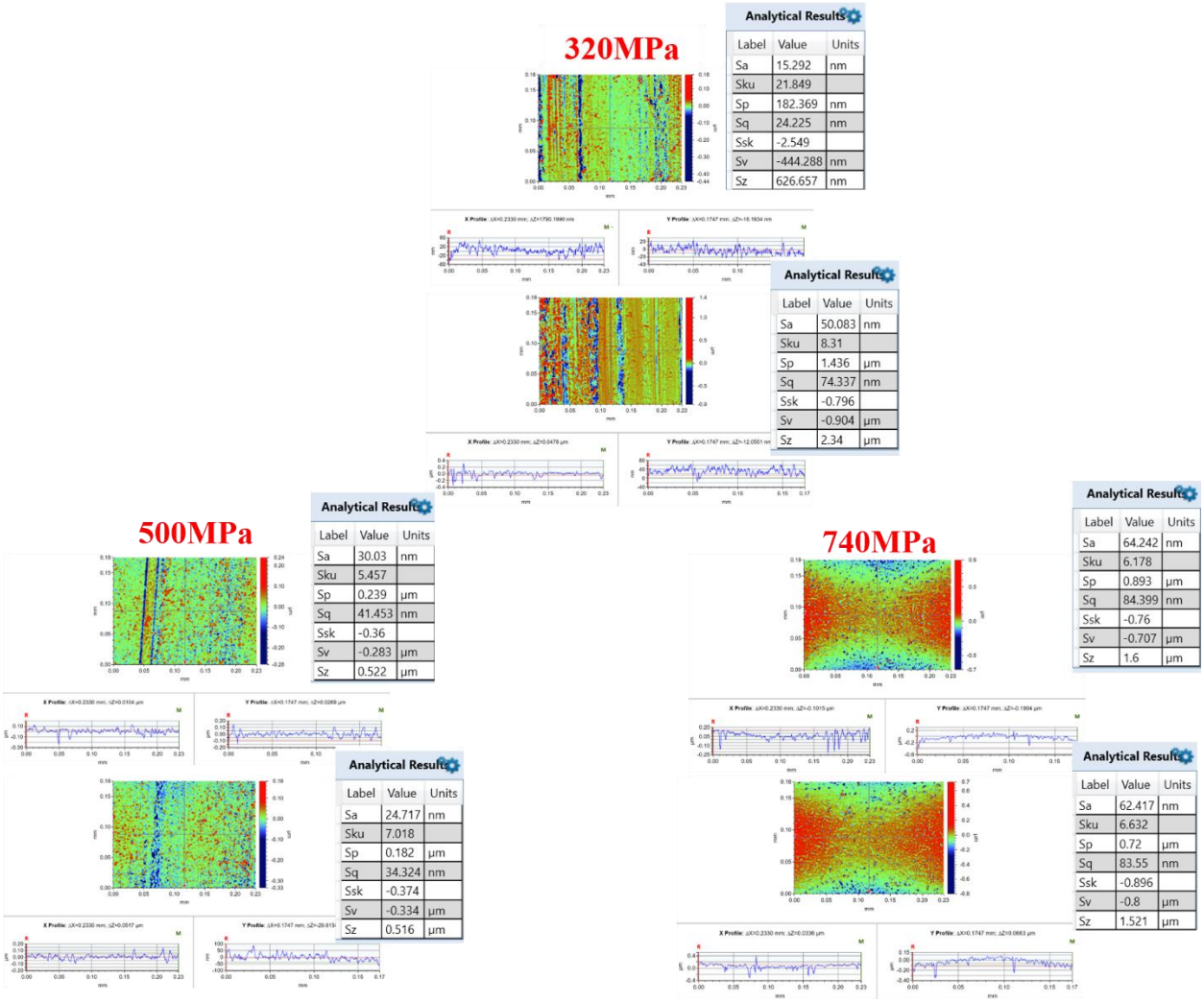

Fig. A2 The surface roughness of a-C:H ring and a-C:H disk in a-C:H/a-C:H contact and steel ring and steel disk in steel/steel contact after friction tests

Tab. A2 (X represents elements of C, P, S, Ca, Fe, Zn).

Tribo-pairs	Materials	Element	Assignment of species	Binding energy (eV)	Full-width-half-maximum (FWHM)
Steel ring/steel disk at 740MPa (2100N)	Steel ring	C 1s	C-C/C-H	284.76	1.65
			C-O	286.88	1.65
			C=O	288.98	1.65
			-CO_3	289.98	1.65
		O 1s	Metallic oxide	/	/
			X = O	531.50	1.83
			X-O	533.29	1.83
		Fe 2p3/2	Fe (0)	/	/
			Fe (II)	708.34	2.59
			Fe (III)	709.96	2.59
			FeOOH	711.98	2.59
			Fe (II) satellite peak	714.29	2.59
		Ca 2p3/2	Calcium carbonate	347.55	1.63
		P 2p3/2	Phosphate	133.48	1.77
		S 2p3/2	Zn-S/Fe-S	161.79	1.43
			S - C	163.61	1.43
			Sulphate	169.55	1.43
		Zn 2p3/2	Zn-S/ZnO	1022.10	1.60
			$ZnSO_4$	1023.80	
	Steel disk	C 1s	C-C/C-H	284.77	1.46
			C-O	286.34	1.46
			C=O	288.62	1.46
			-CO_3	/	1.46
		O 1s	Metallic oxide	/	/
			X = O	531.41	1.58
			X-O	533.09	1.58
		Fe 2p3/2	The signal is too low to fit		
		Ca 2p3/2	Calcium carbonate	348.20	1.50
		P 2p3/2	Phosphate	133.38	1.55
		S 2p3/2	Zn-S/Fe-S	161.72	1.63
			S - C	/	/
			Sulphate	/	/
		Zn 2p3/2	Zn-S/ZnO	1022.22	1.64

a-C:H ring/a-C:H disk at 740MPa (2100N)	a-C:H ring	C 1s	C-C/C-H	284.63	1.29
			C-O	286.28	1.29
			C=O	287.86	1.29
			$-CO_3$	289.45	1.29
		O 1s	Ca - O	529.98	1.94
			X = O	531.06	1.94
			X-O	532.68	1.94
		Ca 2p3/2	Calcium oxide	346.20	1.90
			Calcium carbonate	347.43	1.90
		P 2p3/2	Phosphate	132.17	2.39
		S 2p3/2	Zn-S	161.41	2.80
			S - C	163.42	2.50
			Sulphate	168.88	2.90
		Zn 2p3/2	Zn-S	1021.94	1.81
	a-C:H disk	C 1s	C-C/C-H	284.76	1.44
			C-O	286.12	1.44
			C=O	287.96	1.44
			$-CO_3$	289.94	1.44
		O 1s	Ca - O	/	/
			X = O	532.00	2.06
			X-O	532.96	2.06
		Ca 2p3/2	Calcium oxide	/	/
			Calcium carbonate	347.70	1.57
		P 2p3/2	Phosphate	133.06	2.51
		S 2p3/2	Zn-S	161.79	1.37
			S - C	163.55	1.65
			Sulphate	168.28	2.20
		Zn 2p3/2	Zn-S	1022.17	1.81

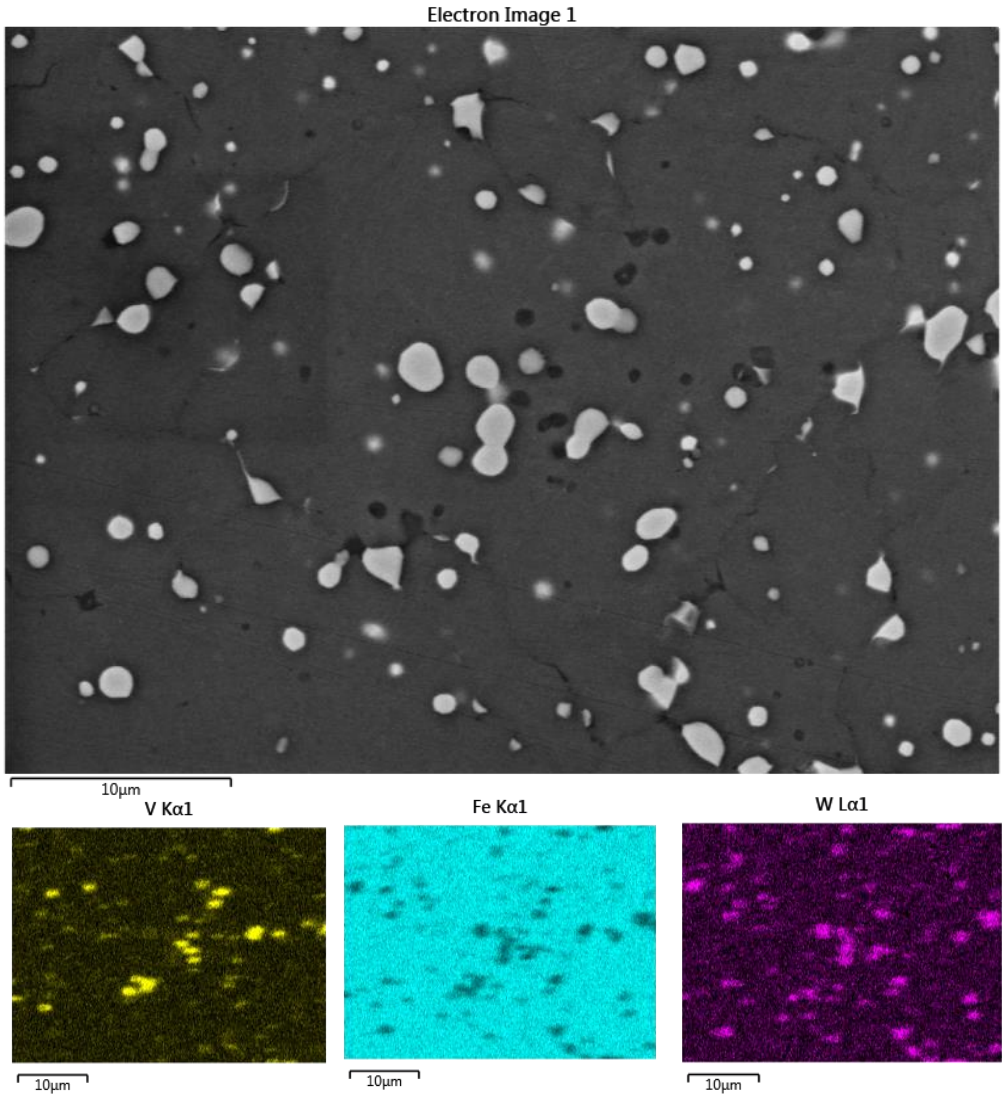

Fig. A3 The EDS mapping results of AISI M2 steel disk

Tab. A3 (X represents elements of C, P, S, Ca, Fe, Zn).

Tribo-pairs	Contact pressure	Materials	Element	Assignments of species	Binding energy (eV)	Full-width-half-maximum (FWHM)
Steel/steel	0.5 GPa	steel ball	C 1s	C-C/C-H	284.83	1.24
				C-O	285.96	1.24
				C=O	288.36	1.24
				-CO_3	290.09	1.24
			O 1s	Metallic oxide	529.60	1.10
				X = O	531.34	2.03
				X – O	532.64	2.03
			Fe 2p3/2	Fe (0)	706.18	0.92
				Fe (II)	708.43	2.25
				Fe (III)	709.83	2.25
				FeOOH	711.69	2.25
				Fe (II) satellite	714.02	2.25
			Ca 2p	$CaCO_3$	347.69	1.58
			P2p	Phosphates	133.41	1.53
			S 2p	Fe-S/Zn-S	161.43	1.43
				Sulphate	168.27	1.15
			Zn 2p3/2	Zn-S	1021.35	1.91
		steel disk	C 1s	C-C/C-H	284.70	1.43
				C-O	285.57	1.43
				C=O	288.49	1.43
				-CO_3	289.88	1.43
			O 1s	Metallic oxide	529.17	1.06
				X = O	531.46	2.05
				X – O	532.84	2.05
			Fe 2p3/2	Fe (0)	706.02	1.21
				Fe (II)	708.23	1.91
				Fe (III)	709.07	1.91
				FeOOH	712.85	1.91
				Fe (II) satellite	713.92	1.91
			Ca 2p	$CaCO_3$	347.42	1.81
			P2p	Phosphates	133.13	1.69
			S 2p	Fe-S/Zn-S	161.28	1.35
				Sulphate	167.87	2.01
			Zn 2p3/2	Zn-S	1020.91	1.49
				$ZnO/Zn(OH)_2$	2022.23	1.49
Steel/steel	1.0 GPa	Steel ball	C 1s	C-C/C-H	284.78	1.16
				C-O	285.78	1.16

				C=O	288.39	1.16
				$-CO_3$	289.82	1.16
			O 1s	Metallic oxide	529.65	1.04
				X = O	530.85	2.09
				X – O	532.02	2.09
			Fe 2p3/2	Fe (0)	706.35	0.87
				Fe (II)	708.04	2.14
				Fe (III)	709.88	2.14
				FeOOH	711.51	2.14
				Fe (II) satellite	713.33	2.14
			Ca 2p	Calcium carbonate	347.52	1.57
			P2p	Phosphates	133.15	1.71
			S 2p	Fe-S/Zn-S	161.72	1.54
				Sulphate	168.51	1.99
			Zn 2p3/2	Zn-S	1021.76	1.76
		Steel disk	C 1s	C-C/C-H	284.75	1.30
				C-O	285.87	1.30
				C=O	288.41	1.30
				$-CO_3$	289.73	1.30
			O 1s	Metallic oxide	529.37	1.02
				X = O	531.23	1.83
				X – O	532.52	1.83
			Fe 2p3/2	Fe (0)	706.07	1.19
				Fe (II)	708.19	2.29
				Fe (III)	709.82	2.29
				FeOOH	711.78	2.29
				Fe (II) satellite	714.35	2.29
			Ca 2p	$CaCO_3$	347.30	1.60
			P2p	Phosphates	132.95	1.41
			S 2p	Fe-S/Zn-S	161.22	1.52
				Sulphate	168.56	1.98
			Zn 2p3/2	Zn-S	1021.25	1.34
				$ZnO/Zn(OH)_2$	1022.33	1.34
a-C:H / steel	0.5GPa	a-C:H ball	Wear track is not available for XPS analyses			
			C 1s	C-C/C-H	284.79	1.45

		Steel disk		C-O	285.71	1.45
				C=O	288.92	1.45
				-CO_3	290.10	1.45
			O 1s	Metallic oxide	529.56	1.49
				X = O	531.80	2.04
				X – O	533.57	2.04
			Fe 2p3/2	Fe (0)	706.12	0.92
				Fe (II)	708.32	2.16
				Fe (III)	709.72	2.16
				FeOOH	711.15	2.16
				Fe (II) satellite	713.91	2.16
			Ca 2p	$CaCO_3$	347.55	1.73
			P2p	Phosphates	133.04	1.65
			S 2p	Fe-S/Zn-S	161.68	1.74
				Sulphate	168.72	2.56
			Zn 2p3/2	Zn-S	1021.56	2.02
		a-C:H ball	Wear track is not available for XPS analyses			
	1.0GPa	Steel disk	C 1s	C-C/C-H	284.79	1.40
				C-O	286.02	1.40
				C=O	288.93	1.40
				-CO_3	290.00	1.40
			O 1s	Metallic oxide	529.40	1.09
				X = O	531.30	1.67
				X – O	532.65	1.67
			Fe 2p3/2	Fe (0)	706.49	1.50
				Fe (II)	708.06	2.42
				Fe (III)	709.59	2.42
				FeOOH	711.62	2.42
				Fe (II) satellite	714.78	2.42
			Ca 2p	$CaCO_3$	347.49	1.53
			P2p	Phosphates	133.21	1.47
			S 2p	Fe-S/Zn-S	161.54	1.63
				Sulphate	168.64	2.74
			Zn 2p3/2	Zn-S	1021.23	1.75

a-C:H / a-C:H	0.5GPa	a-C:H ball	C 1s	C-C/C-H	284.75	1.54
				C-O	286.54	1.54
				C=O	288.49	1.54
				-CO_3	290.29	1.54
			O 1s	X = O	531.82	2.02
				X – O	533.10	2.02
			Ca 2p	$CaCO_3$	347.74	1.53
			P2p	Phosphates	133.40	1.65
			S 2p	Fe-S/Zn-S	161.56	1.70
				S - C	163.29	1.38
				Sulphate	168.25	2.75
			Zn 2p3/2	Zn-S	1021.75	1.81
		a-C:H disk	C 1s	C-C/C-H	284.74	1.53
				C-O	286.54	1.53
				C=O	288.52	1.53
				-CO_3	290.15	1.53
			O 1s	X = O	531.83	1.63
				X – O	533.23	1.63
			Ca 2p	$CaCO_3$	347.71	1.44
			P2p	Phosphates	133.29	1.35
			S 2p	Fe-S/Zn-S	161.72	1.40
				S - C	163.29	1.35
				Sulphate	168.45	2.82
			Zn 2p3/2	Zn-S	1021.88	1.62
	1.0GPa	a-C:H ball	C 1s	C-C/C-H	284.71	1.56
				C-O	286.54	1.56
				C=O	288.65	1.56
				-CO_3	290.23	1.56
			O 1s	X = O	532.10	1.89
				X – O	533.40	1.89
			Ca 2p	$CaCO_3$	347.80	1.61
			P2p	Phosphates	133.29	1.57
			S 2p	Fe-S/Zn-S	161.82	1.77
				S - C	163.33	1.86
				Sulphate	168.26	2.87
			Zn 2p3/2	Zn-S	1021.82	1.67
	1.0GPa	a-C:H disk	C 1s	C-C/C-H	284.73	1.55
				C-O	286.45	1.55
				C=O	288.42	1.55
				-CO_3	290.16	1.55
			O 1s	X = O	531.82	1.98
				X – O	533.43	1.98
			Ca 2p	$CaCO_3$	347.70	1.46
			P2p	Phosphates	133.33	1.29

			S 2p	Fe-S/Zn-S	161.78	1.40
				S - C	163.21	2.82
				Sulphate	168.67	1.39
			Zn 2p3/2	Zn-S	1022.07	1.60

Tab. A4 (X represents elements of C, Fe, Ca).

Tribo-pairs	Contact pressure	Materials	Element	Assignments of species	Binding energy (eV)	Full-width-half-maximum (FWHM)
Steel/steel	0.5 GPa	steel ball	C 1s	C-C/C-H	284.75	1.41
				C-O	286.05	1.41
				C=O	288.50	1.41
				-CO_3	290.18	1.41
			O 1s	Metallic oxide	529.61	1.40
				X = O	531.53	1.40
				X – O	532.45	1.40
			Fe 2p3/2	Fe (0)	706.22	0.78
				Fe (II)	708.26	2.10
				Fe (III)	709.89	2.10
				FeOOH	711.64	2.10
				Fe (II) satellite	713.61	2.10
			Ca 2p	$CaCO_3$	347.63	1.70
		steel disk	C 1s	C-C/C-H	284.86	1.44
				C-O	286.77	1.44
				C=O	288.57	1.44
				-CO_3	290.26	1.44
			O 1s	Metallic oxide	/	/
				X = O	532.06	1.79
				X – O	533.79	1.79
			Fe 2p3/2	Fe (0)	706.21	0.58
				Fe (II)	707.71	1.72
				Fe (III)	710.96	1.72
				FeOOH	712.77	1.72
				Fe (II) satellite	714.76	1.72
			Ca 2p	$CaCO_3$	347.73	1.82
	1.0GPa	Steel ball	C 1s	C-C/C-H	284.81	1.36
				C-O	286.02	1.36
				C=O	288.70	1.36
				-CO_3	290.09	1.36
			O 1s	Metallic oxide	529.83	1.53
				X = O	531.74	1.53
				X – O	532.40	1.53
			Fe 2p3/2	Fe (0)	706.24	0.54
				Fe (II)	708.46	2.14
				Fe (III)	709.82	2.14

				FeOOH	711.36	2.14
				Fe (II) satellite	713.61	2.14
			Ca 2p	$CaCO_3$	347.56	1.53
		Steel disk	C 1s	C-C/C-H	284.77	1.56
				C-O	286.64	1.56
				C=O	288.71	1.56
				$-CO_3$	290.23	1.56
			O 1s	Metallic oxide	/	
				X = O	531.94	1.86
				X – O	533.56	1.86
			Fe 2p3/2	Fe (0)	705.98	1.01
				Fe (II)	708.71	1.40
				Fe (III)	711.23	1.40
				FeOOH	712.83	1.40
				Fe (II) satellite	714.54	1.40
			Ca 2p	$CaCO_3$	347.56	1.95
a-C:H /steel	0.5GPa	a-C:H ball	C 1s	C-C/C-H	284.81	1.44
				C-O	286.22	1.44
				C=O	288.58	1.44
				$-CO_3$	290.10	1.44
			O 1s	Metallic oxide	/	
				X = O	532.10	1.85
				X – O	533.32	1.85
			Ca 2p	$CaCO_3$	347.54	1.53
		Steel disk	C 1s	C-C/C-H	284.80	1.59
				C-O	286.84	1.59
				C=O	289.42	1.59
				$-CO_3$	290.91	1.59
			O 1s	Metallic oxide	/	
				X = O	532.10	1.80
				X – O	533.81	1.80
			Fe 2p3/2	Fe (0)	705.97	0.70

				Fe (II)	708.53	2.53
				Fe (III)	710.25	2.53
				FeOOH	712.54	2.53
				Fe (II) satellite	714.80	2.53
			Ca 2p	$CaCO_3$	347.42	1.80
	1.0GPa	a-C:H ball	C 1s	C-C/C-H	284.81	1.29
				C-O	286.74	1.29
				C=O	288.57	1.29
				$-CO_3$	290.29	1.29
			O 1s	Metallic oxide	/	
				X = O	532.08	1.65
				X – O	533.53	1.65
			Ca 2p	Calcium carbonate	347.75	1.48
		Steel disk	C 1s	C-C/C-H	284.80	1.48
				C-O	285.88	1.48
				C=O	288.73	1.48
				$-CO_3$	290.28	1.48
			O 1s	Metallic oxide	/	
				X = O	531.98	1.82
				X – O	533.72	1.82
			Fe 2p3/2	The signal is too low to be fitted		
			Ca 2p	$CaCO_3$	347.54	1.88
	0.5GPa	a-C:H ball	C 1s	C-C/C-H	284.78	1.40
				C-O	286.42	1.40
				C=O	288.85	1.40
				$-CO_3$	290.24	1.40
			O 1s	X = O	532.22	1.74
				X – O	533.71	1.74
			Ca 2p	$CaCO_3$	347.73	1.52
		a-C:H disk	C 1s	C-C/C-H	284.78	1.57
				C-O	286.66	1.57
				C=O	288.98	1.57

				-CO_3	291.31	1.57
			O 1s	X = O	532.20	2.02
				X – O	533.57	2.02
			Ca 2p	$CaCO_3$	347.70	1.72
		a-C:H ball	C 1s	C-C/C-H	284.80	1.12
				C-O	285.92	1.12
				C=O	288.99	1.12
				-CO_3	290.22	1.12
			O 1s	X = O	532.10	1.60
				X – O	533.61	1.60
			Ca 2p	$CaCO_3$	347.74	1.43
	0.5GPa	a-C:H disk	C 1s	C-C/C-H	284.73	1.56
				C-O	286.86	1.56
				C=O	288.82	1.56
				-CO_3	290.32	1.56
			O 1s	X = O	532.01	2.04
				X – O	533.43	2.04
			Ca 2p	$CaCO_3$	347.51	1.87